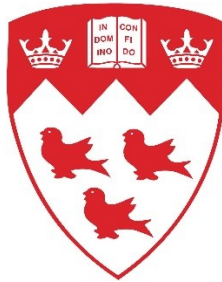


# **Rotor Design Optimization of Permanent Magnet–Assisted Synchronous Reluctance Machines for Traction Applications**

Mohammad Hossain Mohammadi, B.S.E.E



Department of Electrical and Computer Engineering

Faculty of Engineering, McGill University

Montreal, Quebec, Canada

November 2015

A thesis submitted to McGill University in partial fulfillment of the requirements of the degree of Master of Engineering (Thesis)

© Mohammad Hossain Mohammadi, 2015

## ABSTRACT

In the past decades, the electrification of the transportation industry has pushed to improve the performance of the electric drivetrain, especially the electric motor, in traction applications. Recent fluctuations in the price and supply of rare-earth *permanent magnets* (PMs), which are primarily used in most traction electric motors, has driven researchers to explore alternative motor topologies such as the *Synchronous Reluctance Machine* (SynRM). Although pure SynRMs benefit from simple rotor manufacturing and low material cost, they fail to directly compete with the high torque-to-rotor-volume density, efficiency, power factor and Constant Power Speed Range of Interior Permanent Magnet machines. It is possible to address the pure SynRM's performance limitations by inserting low-cost PMs inside its rotor structure to give rise to a Permanent Magnet-assisted SynRM. There are, however, computational bottlenecks in arriving at an optimal PM-assisted SynRM design solution. If correct methodologies are not employed, an optimal solution may or may not be found with less confidence in its optimality properties.

This thesis addresses the computational and design challenges involved in the rotor design optimization of PM-assisted Synchronous Reluctance Machines for traction applications. Upon presenting a brief theory of electric drives, a case study for a direct-drive application is used to illustrate the global and local rotor optimizations by using artificial intelligence and genetic algorithm methods. Novel methodologies for modelling and optimizing SynRM rotors are presented. These can be used to find the set of global optimal solutions using less computational effort, compare general rotor models using a Response Surface map, generalize the space mapping from a single-barrier to a multiple-barrier rotor design, and indicate whether a suggested solution is globally optimal using a proposed analytical function. Both single and multiple-barrier SynRM rotor topologies are explored, and model improvements are validated using accurate numerical simulations. The final rotor design is then compared with a direct-drive motor used in automotive applications, while considering the current and voltage limitations of the inverter drive system. In addition, a brief robustness analysis is performed for the final PM-assisted SynRM solution to account for imperfections and uncertainties in the rotor manufacturing process, magnetic material properties and motor controller setpoints.

### RÉSUMÉ

Au cours des dernières décennies, l'électrification de l'industrie du transport a poussé pour améliorer la performance de la transmission électrique et, en particulier, les applications de traction. Les récentes fluctuations du prix et de l'offre des aimants permanents de terres rares (AP), qui sont principalement utilisés dans la plupart des moteurs de traction électriques, ont encouragé les chercheurs à explorer plusieurs topologies de moteurs, tels que le moteur synchrone à réluctance (MSynR). Même si les MSynR bénéficient de la fabrication de rotors simples et un coût de matériaux faible, ils ne parviennent pas à rivaliser le fort rapport couple/densité volumique, rendement, facteur de puissance, et fonctionnement à puissance constante des moteurs à aimant permanent. Il est possible de régler les limites de performance des MSynR standards en faisant insérer des aimants permanents à faibles coûts à l'intérieur du rotor pour créer un MSynR assisté d'aimants permanents. Cependant, il y a plusieurs goulots d'étranglement qui préviennent une solution de conception de MSynR assisté AP optimale. Si les méthodes correctes ne sont pas utilisés, une solution optimale peut ou ne peut pas être trouvée avec confiance.

Par conséquent, cette thèse aborde les défis de calculs et de conception impliqués dans l'optimisation de la conception du rotor de MSynR assisté AP pour les applications de traction. Sur présentation d'une théorie de commande électrique, une étude de cas de prise directe est utilisée pour illustrer les optimisations globales et locales de rotor en utilisant des méthodes d'intelligence artificielle et d'algorithmes génétiques. Plusieurs méthodologies nouvelles pour la modélisation et l'optimisation des rotors de MSynR sont présentées. Ceux-ci peuvent trouver l'ensemble des solutions optimales globales en utilisant moins de calculs, peuvent comparer les modèles de rotor généraux en utilisant une surface de réponses, peuvent généraliser la cartographie de l'espace à partir d'une conception de rotor à barrière simple ou à barrières multiples, et peuvent indiquer si une solution est globalement optimale à l'aide d'une fonction analytique proposée. Les topologies de rotor à barrière simple et à barrières multiples du MSynR sont explorées, et des améliorations du modèle sont validées à l'aide de simulations numériques précises. La conception du rotor final est ensuite comparée avec un moteur à prise directe utilisée dans les applications automobiles, tout en tenant compte des limites actuelles de tension et de courant de l'onduleur. En outre, une brève analyse de la robustesse du MSynR assisté AP final est effectuée pour tenir compte des imperfections et des incertitudes dans le processus de fabrication du rotor, les propriétés des matériaux magnétiques, et les points de réglage du moteur.

## ACKNOWLEDGEMENTS

I would like to dedicate my sincere gratitude to my research advisor, Prof. David A. Lowther, for his timely supervision, constructive criticism and financial support over the past two years. I am honored to have had this research opportunity to learn from his patience and persistence. Not to forget, this work would not have been possible without the close guidance of Dr. Tanvir Rahman.

Moreover I am greatly indebted to the *Natural Sciences and Engineering Research Council of Canada* (NSERC) for financially supporting this work. I am thankful to the Infolytica Corporation for providing me with academic licenses to their *MotorSolve* and *MagNet* software. Also, I highly appreciate the additional feedback and suggestions received from Dr. Majid Poshtan.

To my fellow colleagues at the *Computational Electromagnetics* and the *Electric Energy Systems Laboratories* – Mr. Rodrigo César Pedrosa Silva, Dr. Min Li, Dr. Rajeev Das, Mr. Adrian Ngoly, Mr. Vahid Ghorbanian, Mr. Sajid Hussain, Mr. Moein Nazari, Mr. Ryan Galagusz, Mr. Subhadeep Bhattacharya and Mr. Syed Qaseem Ali – I wish to thank you for your technical support and helpful words of encouragement. I am grateful to have worked with former and current members of the *McGill IEEE Student Branch*, especially Ms. Malika Meghjani, Dr. Ali Jahanbani Ardakani, Mr. Ahmad Muannaki and Prof. Roni Khazaka, and shared lasting moments of laughter and sorrow.

Last but not the least, my highest appreciation goes to my loving family and friends. I will never forget their unwavering support and kindness through good and stressful times.

*“Human beings are members of a whole, In creation of one essence and soul.  
If one member is afflicted with pain, Other members uneasy will remain.  
If you have no sympathy for human pain, The name of human you cannot retain!”*

*“Les hommes sont membres les uns des autres, et tous créés de même matière.  
Si un membre est affligé, les autres s'en ressentent.  
Qui n'est pas touché du mal d'autrui, ne mérite pas d'être appelé homme!”*

**Sheikh Moslehedin Sa'adi**, *Golestan*, 1258 CE

**TABLE OF CONTENTS**

ABSTRACT.....	ii
RÉSUMÉ.....	iii
ACKNOWLEDGEMENTS.....	iv
TABLE OF CONTENTS.....	v
LIST OF FIGURES.....	vii
LIST OF TABLES.....	ix
GLOSSARY OF ABBREVIATIONS.....	x
GLOSSARY OF SYMBOLS.....	xi
FREQUENTLY-USED SUBSCRIPTS AND SUPERSSCRIPTS.....	xiii
Chapter 1 INTRODUCTION.....	1
1.1. Introduction.....	1
1.1.1. Electrification of the Transportation Industry.....	1
1.1.2. Automotive Initiatives and Future Targets.....	3
1.2. Traction Electric Machine: Synchronous Topologies.....	4
1.2.1. Permanent Magnet Machines.....	5
1.2.2. Variable Reluctance Machines.....	5
1.3. Thesis Objectives.....	9
Chapter 2 THEORY OF ELECTRIC DRIVES.....	10
2.1. Introduction.....	10
2.1.1. Inverter-Driven Systems.....	10
2.1.2. Synchronous Machine Theory.....	12
2.1.3. Salient Rotor Structures.....	15
2.2. Motor Control Strategies.....	16
2.2.1. Maximum-Power-Factor Control.....	17
2.2.2. Maximum-Torque-Per-Ampere Control.....	18
2.2.3. Flux-Weakening and Maximum-Torque-per-Volt Control.....	20
2.3. Analysis and Simulation Methods.....	23
2.3.1. IPM Parameter Plane.....	23
2.3.2. Insulation Ratio.....	24
2.3.3. Finite Element Analysis.....	24
2.4. Case Study Definition.....	27
2.5. Conclusion.....	29

# TABLE OF CONTENTS

---

Chapter 3 GLOBAL ROTOR DESIGN OPTIMIZATION .....	30
3.1. Introduction.....	30
3.1.1. Sampling Plans.....	30
3.1.2. Pareto Fronts .....	31
3.1.3. Initial Sizing.....	32
3.1.4. Design Challenges .....	33
3.2. Single-Barrier Rotor Design .....	34
3.2.1. Geometric Modelling.....	34
3.2.2. Data Acquisition .....	36
3.2.3. Supplementary Analysis .....	41
3.2.4. Surrogate Modelling .....	43
3.2.5. Multi-Objective Optimization.....	48
3.3. Result Verification and Discussion.....	52
3.3.1. Pareto Front Validation.....	53
3.3.2. Double-Barrier Validation .....	54
3.4. Conclusion .....	55
Chapter 4 LOCAL ROTOR DESIGN OPTIMIZATION.....	56
4.1. Introduction.....	56
4.2. Multiple-Barrier Rotor Design.....	56
4.2.1. Selection of a Global Optimal Design .....	56
4.2.2. Generalization to a Multiple-Barrier Design .....	57
4.2.3. Effect on Inverter Drives .....	61
4.3. Permanent Magnet-Assisted Rotor Design.....	62
4.3.1. Barrier Refinements .....	62
4.3.2. Power-Speed Characteristic .....	66
4.3.3. Design Comparison.....	67
4.4. Robustness Analysis .....	71
4.5. Conclusion .....	73
Chapter 5 CONCLUSION .....	74
BIBLIOGRAPHY .....	75

---

**LIST OF FIGURES**

Figure 1. Schematic of a Typical Series Hybrid Electric Drivetrain [2] .....	2
Figure 2. Cross-Sections of Selected Synchronous Electric Machines [9]: white represents Fe, dark grey on rotors represent PMs, dark grey on the stator of (b) represents Cu windings.....	4
Figure 3. Variable Reluctance Rotor Laminations [11]: (a) Switched Reluctance Motor, (b) ALA Synchronous Reluctance Motor, (c) TLA Synchronous Reluctance Motor .....	5
Figure 4. Kostko’s Rotor for the <i>Reaction Synchronous Motor</i> [12] .....	8
Figure 5. Evolution of the SynRM Rotor [14], [20] .....	8
Figure 6. Typical Schematic of a Synchronous Motor Drive System [27].....	10
Figure 7. <i>3-Phase 2-Level</i> Inverter (a) Schematic, (b) PWM Waveform with Fundamental [29]	11
Figure 8. <i>3-Phase</i> Inverter Voltage-Control Ranges through Modulation [29].....	11
Figure 9. Vector Diagram of a PM-Assisted SynRM without Rotor Core Losses: partial rotor cross-section demonstrates its <i>dq</i> -axes .....	13
Figure 10. Ideal Drive Characteristics for Different Motor Speeds [36] .....	16
Figure 11. MPF versus Saliency Ratio [13].....	18
Figure 12. General ALA Rotor Construction [13].....	18
Figure 13. Relationships between $L_d$ (lower) and $L_q$ (upper) Inductances with $I_s$ [38] .....	19
Figure 14. MTPA Variation with Current Angle $\gamma$ for Different Currents $I_s$ [38] .....	19
Figure 15. Mode Diagram including the Maximum Torque Trajectory (bold) for Zero to Infinite Speeds. Mode I: MTPA, Mode II: FW, Mode III: MTPV [36] .....	21
Figure 16. Maximum Torque Trajectories for Five Drive Classes [36] .....	22
Figure 17. (a) Power-Speed Curves and (b) SM Drive Classes in the $(\xi, \lambda_{mn})$ Plane [36] .....	23
Figure 18. <i>TM4 Sumo MD</i> Motor [44].....	27
Figure 19. Cross-Section View of the <i>Initial IPM</i> Motor .....	28
Figure 20. Sampling Plans for 2 Variables: (a) Full Factorial across 3 Levels, (b) Latin Hypercube for 8 Points [45] .....	31
Figure 21. Pareto Front Example of Two Objectives $f_1$ and $f_2$ [48] .....	32
Figure 22. Continuous Rotor Design Variables across a Rotor Pole and its <i>dq</i> -axes.....	35
Figure 23. Solution Mesh of an <i>8-Pole</i> Single-Barrier SynRM Rotor ( $1.0I_{rated}$ , $56^\circ$ ) .....	37
Figure 24. FEA Field Plot of an <i>8-Pole</i> Single-Barrier SynRM Rotor ( $1.0I_{rated}$ , $56^\circ$ ) .....	37
Figure 25. Sensitivity of Torque Ripple to the <i>Speed/Accuracy</i> Tradeoff Setting .....	38

---

LIST OF FIGURES

---

Figure 26. Pseudocode for the MTPA Peak Finding Algorithm .....	39
Figure 27. Example of the MTPA Peak Finding Algorithm (4 Iterations).....	40
Figure 28. FEA Field Plot of an 8-Pole Single-Barrier SynRM ( $1.0I_{rated}$ , $0^\circ$ , $I_d=0$ ) .....	41
Figure 29. FEA Field Plot of an 8-Pole Single-Barrier SynRM ( $1.0I_{rated}$ , $90^\circ$ , $I_q=0$ ) .....	41
Figure 30. Instantaneous Torque Plots for 3 Advance Angles (8 poles, $1.0I_{rated}$ ) .....	42
Figure 31. Sensitivity of Average Torque to the Radial Rib Width for Different Currents .....	42
Figure 32. Sensitivity of Average Torque to the Tangential Rib Width for Different Currents...	43
Figure 33. A Multiple-Input Neuron [56].....	43
Figure 34. 3-Input 1-Output Artificial Neural Network with a Single Hidden Layer .....	43
Figure 35. BRNN Training Algorithm Pseudocode .....	45
Figure 36. Single-Barrier: Average Torque RS Map for (8 poles, $2.0I_{rated}$ ).....	46
Figure 37. Single-Barrier: Torque Ripple RS Map for (8 poles, $2.0I_{rated}$ ).....	46
Figure 38. Boxplot of $R^2_{test}$ and Number of Neurons for 30 Repetitions ( $T_{rip}$ , 8 poles, $2.0I_{rated}$ ) .	47
Figure 39. Pareto Fronts for Three Currents Levels in the Objective Plane.....	50
Figure 40. Pareto Front Solutions for Three Currents Levels in the Design Plane .....	51
Figure 41. Objective Boxplots for Methods A and B in the Double-Barrier Space.....	54
Figure 42. Rotor Half-Pole Variables: (a) Single-Barrier (left), (b) Double-Barrier (right) .....	57
Figure 43. Double-Barrier: Average Torque RS Map for (8 poles, $2.0I_{rated}$ ) .....	58
Figure 44. Double-Barrier: Torque Ripple RS Map for (8 poles, $2.0I_{rated}$ ) .....	58
Figure 45. High $T_{avg}$ Regions: (a) Single-Barrier (left), (b) Double-Barrier (right).....	59
Figure 46. FEA Field Plot of the Improved Double-Barrier SynRM Rotor ( $1.0I_{rated}$ , $59^\circ$ ).....	60
Figure 47. Current-Limit Circles (blue, green, red) and Voltage-Limit Ellipses (black) for Different Currents and Rotor Speeds of the Double-Barrier Improved Design .....	61
Figure 48. Rotor Geometric Variables for Angled Flux Barriers (radial PM magnetization).....	63
Figure 49. Demagnetization BH Curves for Different Magnets at $20^\circ\text{C}$ Temperature .....	63
Figure 50. Contour Plots of (a) Average Torque (b) Torque Ripple .....	65
Figure 51. 2B-PMa SynRM: Power-Speed Characteristics.....	67
Figure 52. Average Torque Comparison between Different Motors .....	69
Figure 53. Inverter Utilization Ratio for 2B-PMa-SynRM (dashed) and Initial IPM (dotted) .....	70
Figure 54. Normalized $N_{max}$ for 2B-PMa-SynRM (dashed) and Initial IPM (dotted).....	70
Figure 55. Remanent Flux Density Parameters of 6 PMs across 1 Rotor Pole .....	71

---

---

**LIST OF TABLES**

Table 1. Technical Targets for Electric Traction System [6].....	3
Table 2. Performance Specifications of a High-Torque, Low-Speed Direct-Drive Motor [44]...	27
Table 3. <i>Initial IPM</i> Motor Parameters and Ratings.....	28
Table 4. <i>Initial IPM</i> Motor Material Costs using Material Pricing in [23].....	28
Table 5. Training, Validation and Testing $R^2$ Coefficients for Three Currents of the Trained BRNN Functions for the Average Torque and Torque Ripple Objectives.....	47
Table 6. Statistics ( $\mu_{rip}$ , $\sigma_{rip}$ ) of All Single-Barrier Designs for the $T_{rip}$ Objective .....	51
Table 7. Relative Error Percentage Statistics for Validated FEA Solutions.....	53
Table 8. Comparison between Optimal and Non-Optimal Solutions for $2.0I_{rated}$ .....	53
Table 9. Single-Barrier $T_{avg}$ [ $Nm$ ], $T_{rip}$ [%] and $k_{air,r}$ for $max(T_{avg})$ Results.....	56
Table 10. Result Summary of Double-Barrier Design.....	59
Table 11. Result Summary of the <i>2B-PMa SynRM</i> (Ceramic 10) .....	65
Table 12. Performance Comparison between Different Motors.....	68
Table 13. Extreme Variations of Geometric Parameters across $l$ Rotor Pole.....	71
Table 14. Extreme Variations of Remanent Flux Density Parameters across $l$ Rotor Pole.....	71
Table 15. Sensitivity Results of the 2 Objectives to Extreme Parameter Variations.....	73

---

**GLOSSARY OF ABBREVIATIONS**

<b><i>Symbol</i></b>	<b><i>Description</i></b>
AC	Alternating Current
ALA	Axially-Laminated Anisotropic
ANN	Artificial Neural Network
BRNN	Bayesian Regularization Backpropagation Neural Network
CPSR	Constant Power Speed Range
Cu	Copper
DC	Direct Current
Fe	Iron
FEA	Finite Element Analysis
FOC	Field-Oriented Control
FW	Flux-Weakening
GA	Genetic Algorithm
HEV	Hybrid and Electric Vehicle
IC	Internal Combustion
IGBT	Insulated-Gate Bipolar Transistor
IM	Induction Motor/Machine
IPM	Interior Permanent Magnet
IUR	Inverter Utilization Ratio
MMF	Magnetomotive Force
MOGA	Multi-Objective Genetic Algorithm
MOSFET	Metal-Oxide-Semiconductor Field-Effect Transistor
MPF	Maximum-Power-Factor
MTPA	Maximum-Torque-Per-Ampere
MTPV	Maximum-Torque-Per-Volt
NdFeB	Neodymium Iron Boron
PDE	Partial Differential Equation
PM	Permanent Magnet
PU	Per-Unit
PWM	Pulse-Width-Modulated/Modulation
RMS	Root Mean Square
RS	Response Surface
SMPM	Surface-Mounted Permanent Magnet
SRM	Switched Reluctance Motor/Machine
SynRM	Synchronous Reluctance Motor/Machine
TLA	Transversally-Laminated Anisotropic

## GLOSSARY OF SYMBOLS

<b><i>Symbol</i></b>	<b><i>Description</i></b>	<b><i>Unit</i></b>	<b><i>Unit Name</i></b>
$\vec{A}$	magnetic vector potential	<i>Tm</i>	<i>tesla-meter</i>
$A_{lim}$	PM area limit per rotor pole	$mm^2$	<i>millimeter-squared</i>
$\vec{B}$	magnetic flux density vector	<i>T</i>	<i>tesla</i>
$B_r$	remnant magnetic flux density	<i>T</i>	<i>tesla</i>
$D_{ri/o}$	rotor inner/outer diameter	<i>mm</i>	<i>millimeter</i>
$D_{so}$	stator outer diameter	<i>mm</i>	<i>millimeter</i>
$e_r$	relative error percentage	%	
$f$	function or objective values		
$\mathcal{F}_{HT}$	set of high-torque solution points		
$\mathcal{F}_{OPT}$	set of optimal design space points		
$\mathcal{F}_{\Delta}$	set of feasible design space points		
$\vec{H}$	magnetic field intensity vector	<i>A/m</i>	<i>ampere-per-meter</i>
$H_c$	coercive magnetic field intensity	<i>A/m</i>	<i>ampere-per-meter</i>
$i_s$	instantaneous stator winding current	<i>A</i>	<i>ampere</i>
$I_s$	stator winding current magnitude	<i>A</i>	<i>ampere</i>
$I_{d/q}$	direct/quadrature-axis stator current	<i>A</i>	<i>ampere</i>
$j$	imaginary unit number ( $\sqrt{-1}$ )		
$J$	stator winding current density	<i>A/mm<sup>2</sup></i>	<i>ampere-per-mm-squared</i>
$k_{air,r}$	rotor insulation ratio		
$k_{air,s}$	stator insulation ratio		
$l_{stk}$	motor stack length	<i>mm</i>	<i>millimeter</i>
$L_{d/q}$	direct/quadrature-axis stator self-inductance	<i>H</i>	<i>henry</i>
$n_b$	number of rotor barriers		<i>barriers</i>
$n_p$	number of rotor poles		<i>poles</i>
$n_s$	number of stator slots		<i>slots</i>
$N$	mechanical angular speed	<i>RPM</i>	<i>revolutions-per-minute</i>
$N_{base}$	rated/base angular speed	<i>RPM</i>	<i>revolutions-per-minute</i>
$N_{max}$	maximum angular speed	<i>RPM</i>	<i>revolutions-per-minute</i>
$P$	active power	<i>W</i>	<i>watt</i>
$\mathcal{R}$	magnetic reluctance	<i>A/Wb</i>	<i>ampere-per-weber</i>
$R_s$	stator winding resistance	$\Omega$	<i>ohm</i>
$SF_n$	net slot-fill factor	%	
$t$	time instant	<i>s</i>	<i>second</i>
$T$	instantaneous rotor torque	<i>Nm</i>	<i>newton-meter</i>
$T_{avg}$	average rotor torque	<i>Nm</i>	<i>newton-meter</i>

GLOSSARY OF SYMBOLS

---

$T_{avg}^{CONT}$	continuous average rotor torque	$Nm$	<i>newton-meter</i>
$T_{avg}^{MAX}$	maximum average rotor torque	$Nm$	<i>newton-meter</i>
$T_{em}$	electromagnetic rotor torque	$Nm$	<i>newton-meter</i>
$T_{rel}$	reluctance rotor torque component	$Nm$	<i>newton-meter</i>
$T_{rip}$	rotor torque ripple (peak-to-peak)	%	
$T_{pm}$	PM rotor torque component	$Nm$	<i>newton-meter</i>
$\vec{v}$	instantaneous velocity vector	$m/s$	<i>meter-per-second</i>
$V_{d/q}$	direct/quadrature-axis stator voltage	$V$	<i>volt</i>
$V_{dc}$	DC bus/link voltage	$V$	<i>volt</i>
$V_s$	stator winding voltage magnitude	$V$	<i>volt</i>
$\overline{W}$	vector of design space variables		
$W_{ag}$	air gap thickness	$mm$	<i>millimeter</i>
$W_b$	width of rotor flux barrier	$mm$	<i>millimeter</i>
$W_c$	width of rotor flux carrier	$mm$	<i>millimeter</i>
$W_i$	width of rotor inner magnet	$mm$	<i>millimeter</i>
$W_o$	width of rotor outer magnet	$mm$	<i>millimeter</i>
$W_{lim}$	total width limit	$mm$	<i>millimeter</i>
$W_r$	width of rotor radial rib	$mm$	<i>millimeter</i>
$W_t$	width of rotor tangential rib	$mm$	<i>millimeter</i>
$\vec{\nabla}$	gradient operator		
$\gamma$	advance angle of stator current	$^\circ, rad$	<i>degree, radian</i>
$\delta$	stator winding flux-linkage load angle	$^\circ, rad$	<i>degree, radian</i>
$\Delta f_r$	relative objective sensitivity	%	
$\Delta T_{1/2}$	previous/current average torque differences	$Nm$	<i>newton-meter</i>
$\eta$	power efficiency	%	
$\theta$	outer magnet orientation of angled rotor	$^\circ, rad$	<i>degree, radian</i>
$\lambda_s$	stator winding flux linkage magnitude	$Vs$	<i>volt-second</i>
$\lambda_{d/q}$	direct/quadrature-axis stator flux linkage	$Vs$	<i>volt-second</i>
$\vec{\mu}$	magnetic permeability vector	$Tm/A$	<i>tesla-meter/per-ampere</i>
$\mu_0$	magnetic permeability constant	$Tm/A$	<i>tesla-meter/per-ampere</i>
$\mu_{rip}$	mean of torque ripple's dataset	%	
$\xi$	magnetic saliency ratio		
$\vec{\sigma}$	electrical conductivity vector	$S/m$	<i>siemen-per-meter</i>
$\vec{\sigma}_{MST}$	Maxwell's stress tensor	$N/m^2$	<i>newton-per-m-squared</i>
$\sigma_{rip}$	standard deviation of torque ripple's dataset	%	
$\varphi$	angular position of rotor	$^\circ, rad$	<i>degree, radian</i>
$\phi$	power factor angle	$^\circ, rad$	<i>degree, radian</i>
$\omega_e$	electrical angular frequency	$rad/s$	<i>radian-per-second</i>

---

## FREQUENTLY-USED SUBSCRIPTS AND SUPERSCRIPTS

<i>Symbol</i>	<i>Description</i>	<i>Examples</i>
<i>avg</i>	average	$T_{avg}$
<i>b</i>	flux barrier	$n_b, W_b$
<i>c</i>	flux carrier	$W_c$
<i>cont</i>	continuous	$T_{avg}^{CONT}$
<i>d</i>	direct-axis	$L_d, I_d, V_d, \lambda_d$
<i>dc</i>	direct-current	$V_{dc}$
<i>e</i>	electrical	$\omega_e$
<i>em</i>	electromagnetic	$T_{em}$
<i>i</i>	inner	$W_i, D_{si}$
<i>lim</i>	limit	$W_{lim}, A_{lim}$
<i>max</i>	maximum	$N_{max}, T_{avg}^{MAX}$
<i>mtpa</i>	maximum-torque-per-ampere	$\gamma^{MTPA}, T_{avg}^{MTPA}, T_{rip}^{MTPA}$
<i>o</i>	outer	$D_{ro}, D_{so}, W_o$
<i>p</i>	rotor poles	$n_p$
<i>pm</i>	permanent magnet component	$T_{pm}$
<i>pu</i>	per-unit	$T_{rel,pu}$
<i>q</i>	quadrature-axis	$L_q, I_q, V_q, \lambda_q$
<i>r</i>	rotor / relative	$D_{ri}, D_{ro}, k_{air,r} / e_r, \Delta f_r$
<i>rated</i>	rated	$I_{rated}, J_{rated}$
<i>rel</i>	reluctance component	$T_{rel}$
<i>rip</i>	ripple	$T_{rip}, \mu_{rip}, \sigma_{rip}$
<i>rms</i>	root mean square	$A_{rms}$
<i>s</i>	stator	$i_s, I_s, k_{air,s}, V_s, \lambda_s, R_s$

## Chapter 1 INTRODUCTION

### 1.1. Introduction

This chapter starts by briefly reviewing recent energy issues in the transportation industry. It highlights the main reasons behind the design optimization of traction electric motors before explaining the different topologies of synchronous electric motors. At the end of the chapter, the design challenges of Synchronous Reluctance Machines are discussed, and the thesis objectives and outline are presented in §1.3.

#### 1.1.1. Electrification of the Transportation Industry

In the 2012 U.S. Annual Energy Review, about 28% of the primary energy consumption occurred in the transportation sector [1]. Given that this energy use is equivalent to around 7825 TWh, developments towards higher energy-efficiency levels in vehicle propulsion systems could result in reducing energy needs. *Internal Combustion* (IC) engines in traditional vehicles, which run from burning hydrocarbon fuels, can optimistically operate at an energy-efficiency of 40%. However, the remaining 60% of the total energy input is either released as unwanted heat energy or as harmful air pollutants into the atmosphere, such as nitrogen oxides that result in acid rains, poisonous carbon monoxides which reduce oxygen levels in living organisms, and unburnt hydrocarbons that create widespread city smog. Also, the accumulation of carbon dioxide gas emissions is largely believed to be responsible for the Earth's climate change, with increasing average global temperatures affecting a multitude of living organisms.

To tackle these environmental concerns, the transportation sector has been targeted for a major technological transformation. One possible long-term solution is the replacement of the IC engine with the energy-efficient electric motor that converts clean electrical energy to mechanical energy. Although its maximum efficiency level reaches to more than 90%, there is a significant limitation in migrating toward a complete electric vehicle solution. It is currently challenging to match the high mileage levels of hydrocarbon-run IC engines with portable battery supplies. Bottlenecks in the specific energy density ( $Wh/kg$ ) of battery supply technologies suggest that pure electric vehicles cannot yet compete with IC engine vehicles. Putting this in perspective, a lithium-ion battery supply can store less than 1 kWh of chemical energy in a single kilogram while gasoline can easily hold up to 12 kWh for the same mass [2].

In the past decades, both traditional and new automotive manufacturers have noticed the underdevelopment of battery supply technologies and have targeted the best of both sides by introducing *Hybrid and Electric Vehicles* (HEVs). These vehicles use electric motors to sustain high energy-efficiency levels alongside hydrocarbon-run IC engines to extend the overall vehicle mileage. According to the U.S. Department of Energy's *100-mile* trip comparative analysis, HEVs have been reported to produce 48% less greenhouse gases than conventional vehicles by considering well-to-wheel emissions [3]. By reducing the over-reliance on a hydrocarbon economy within the transportation industry by using HEVs, it is possible to ensure a smooth transition into a cleaner use of energy resources.

The typical operation of a series HEV drivetrain is briefly explained through Figure 1. A traction electric motor propels the vehicle's tires through a connected transmission system. This motor is either powered through a battery supply (peaking power source) or an engine-generator set. If the battery supply has sufficient energy reserves, the engine-generator set turns off and the battery supply provides the required electrical energy. This enables the electric motor to run at energy-efficient levels. If the battery supply is depleted instead, the engine-generator set switches on and the required electrical energy is converted from burning hydrocarbon fuels at an optimum engine operation. This provides the motor with sufficient energy input for a high vehicle mileage. Throughout the different blocks in the series drivetrain, automatic controllers are used to enable different modes of operation depending on the driver's demands and energy availability.

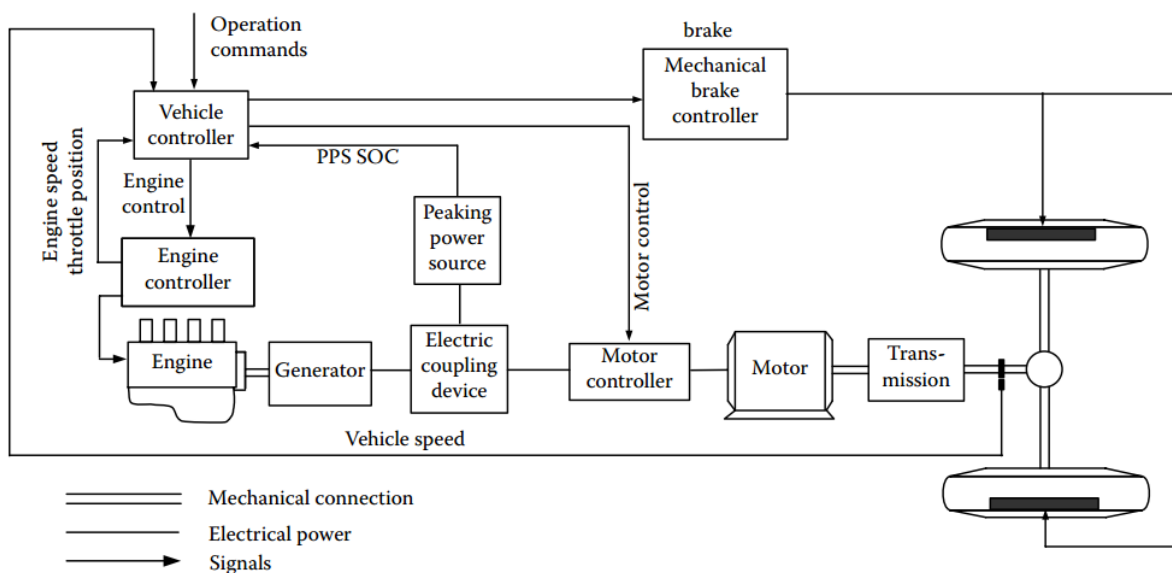


Figure 1. Schematic of a Typical Series Hybrid Electric Drivetrain [2]

### 1.1.2. Automotive Initiatives and Future Targets

Collaborative initiatives such as the *Automotive Partnership Canada* [4] and the *FreedomCAR and Fuel Partnership* in the United States of America [5] have set down long-term visions for gradually phasing out conventional hydrocarbon fuel-driven vehicles. Advanced research on improving the electric drivetrain, which consists of the electric motor, portable fuel or battery supply, power converter, controller and transmission system, is the main focus of such initiatives. Systematically advancing HEVs for their performance, reliability, cost and energy-efficiency requires the electrification of drivetrain components while considering their mutual interactions as well.

An electric motor is typically designed to maximize its torque production for a specific volumetric size and thermal constraints. By boosting its power factor, which is the ratio of the active power used for an invested apparent power, has direct implications on downsizing the vehicle's power converter and cost. This system-level optimization approach requires the identification of vital system objectives for a given set of physical and non-technical constraints to achieve the long-term goals of these automotive initiatives. For example, the U.S. Department of Energy has set down technical targets for the electric traction system to be met by the year 2020 as presented in Table 1. Over the current decade, the specific power, power density and efficiency targets are gradually increased. A stringent requirement is the considerable reduction of the high cost per power which poses an important challenge for automotive manufacturers.

**Table 1. Technical Targets for Electric Traction System [6]**

Technical Target	Unit	2010 <sup>a</sup>	2015 <sup>b</sup>	2020 <sup>b</sup>
<b>Cost per Power</b>	$\$/kW$	$< 19$	$< 12$	$< 8$
<b>Specific Power</b>	$kW/kg$	$> 1.06$	$> 1.20$	$> 1.40$
<b>Power Density</b>	$kW/L$	$> 2.6$	$> 3.5$	$> 4.0$
<b>Efficiency Level (10%-100% rated speed, 20% rated torque)</b>		$> 90\%$	$> 93\%$	$> 94\%$

Based on air or liquid coolant with a maximum temperature of <sup>a</sup> 90°C or <sup>b</sup> 105°C.

Although the popular Toyota Prius, Nissan Leaf and Chevrolet Volt have taken major steps toward mass producing HEVs with significant fuel savings over a multiple-year plan, high initial HEV costs may still not provide an economic incentive to prospective buyers [7]. Cheaper alternatives to individual drivetrain components, such as the electric motor, are necessary while maintaining high performance requirements.

## 1.2. Traction Electric Machine: Synchronous Topologies

As the vehicle's main power plant, an electric machine or motor converts electrical power into mechanical power through a magnetically-coupled medium. The produced mechanical power then propagates along the transmission system to drive the vehicle wheels. An electric motor consists of two main parts: a stationary *stator* comprised of excitation windings and a *rotor* free to rotate about its shaft or axis of rotation. A rotating magnetic field is produced by exciting the multiphase stator windings in a continuous or stepwise approach. Through the principle of electromechanical energy conversion [8], the rotor is forced to rotate and align itself with the stator magnetic axis thereby producing torque. For synchronous motors, the frequencies of the stator and rotor magnetic fields are locked into synchronism as explained under §2.1.2.

To simplify the general classification of synchronous electric motors, the total motor torque produced at a specific rotational speed can be subdivided into two torque components: *permanent magnet* (PM) torque and *reluctance* torque. As the name implies, the PM torque is produced by the interaction of the stator field with a fixed-magnitude rotor PM field (through a permanent magnet buried within the rotor segment). On the other hand, reluctance torque is generated by naturally aligning the rotor's magnetic axis with the stator's in order to minimize the overall magnetic reluctance path. By relying on different combinations of these two torque components, different classes of electric motors are identified in Figure 2: (a) *Surface-Mounted Permanent Magnet* (SMPM) motors only produce PM torque, (b) and (c) *Variable Reluctance* motors only produce reluctance torque, and (d) *Interior Permanent Magnet* (IPM) motors produce both torque components. For each class, a brief summary is provided in §1.2.1 and §1.2.2 respectively.

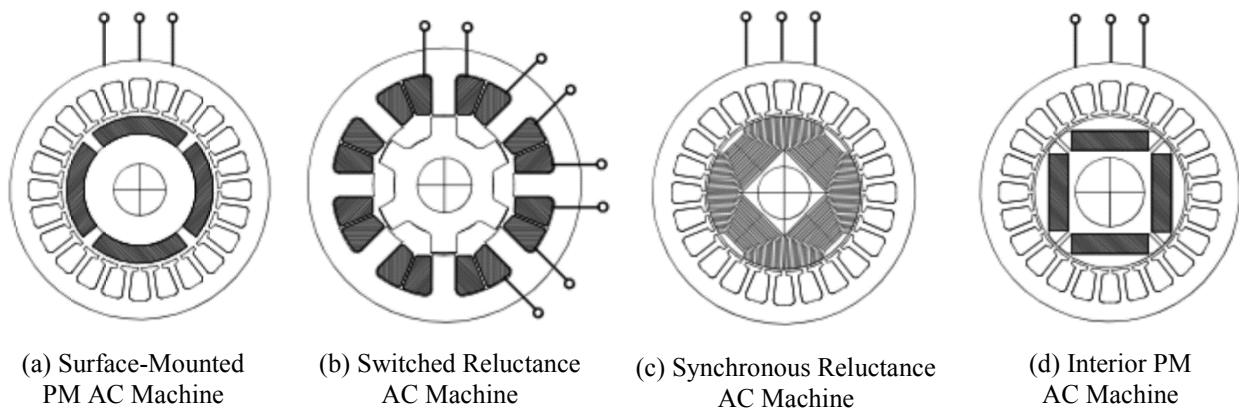


**Figure 2. Cross-Sections of Selected Synchronous Electric Machines [9]: white represents Fe, dark grey on rotors represent PMs, dark grey on the stator of (b) represents Cu windings**

### 1.2.1. Permanent Magnet Machines

Most of the current HEV manufacturers employ rare-earth permanent magnet motors, such as SMPM or IPM motors, in automotive applications. The high-grade PMs buried inside the rotor segment provide a constant rotor magnetic field which interacts with the stator field to produce PM torque at a given angular speed. Benefits of these machines are high torque-to-rotor volume density (smaller frame sizing for the same load torque), efficiency levels and Constant Power Speed Range (CPSR). They can also operate at high power factors that helps decrease the inverter's  $kVA$  sizing and reduce overall system costs [10]. However relying only on producing more PM torque comes at an initial financial expense.

Recent fluctuations in the price and supply of rare-earth magnet materials, such as high-grade *Neodymium-Iron-Boron* (NdFeB), has led to further research activity in alternative motor topologies with significantly less or no rare-earth magnet material, while sustaining the targeted efficiency and performance requirements [10]. One possible alternative is a Variable Reluctance Machine: it produces reluctance torque at synchronous speed through a magnetically-salient rotor structure explained below.

### 1.2.2. Variable Reluctance Machines

Under the Variable Reluctance Machine topology, there are two main types of rotor structures as illustrated in Figure 3: the *Switched Reluctance Machine* (SRM) in (a) and the *Synchronous Reluctance Machine* (SynRM) in (b) and (c). The last two rotor structures in Figure 3 (b) and (c) differ only by their axis of stacking laminations – *Axially-Laminated Anisotropic* (ALA) or *Transversally-Laminated Anisotropic* (TLA) respectively – which is discussed under §2.1.3.

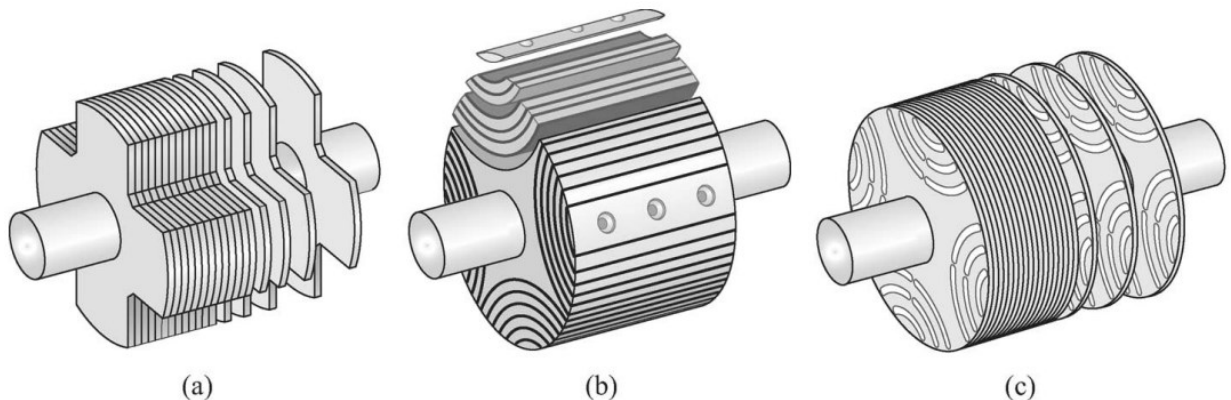


**Figure 3. Variable Reluctance Rotor Laminations [11]: (a) Switched Reluctance Motor, (b) ALA Synchronous Reluctance Motor, (c) TLA Synchronous Reluctance Motor**

SRMs employ a salient rotor with a salient stator (doubly salient), whereas the SynRMs use a salient rotor with a cylindrical stator (singly salient). Salient stators consist of phase windings wound across individual stator poles, while cylindrical stators employ sinusoidally-distributed windings similar to that of an *Induction Machine* (IM).

For a given stator, previous works [12], [13], [14] have demonstrated that geometrically designing a reluctance machine rotor can considerably improve its overall performance. While the two main subclasses of reluctance machines have significant similarities, there are differences in their modes of operation as discussed below.

### 1.2.2.1. Switched Reluctance Motors

Prior to Tesla's invention of the AC *Induction Motor* (IM), doubly-salient Variable Reluctance Motors known as *Switched Reluctance Motors* had already been developed [15], [16]. In 1838, Davidson built the first SRM for driving an electric locomotive on the Glasgow-Edinburgh railway [17]. In this machine topology, each set of stator winding coils is wound on individual stator poles as shown in Figure 2 (b). The coils are excited through a sequence of current pulses on separate phases which magnetizes the salient stator poles. Then, the salient rotor poles attempt to exactly align with the magnetized stator poles in what is called an aligned position [17]. This transient movement produces reluctance torque by lining up the SRM's rotor poles along the path of minimum reluctance, or correspondingly the maximum inductance. When the rotor is perfectly aligned, no more torque can be produced.

The SRM rotor illustrated in Figure 3 (a) rotates at a mechanical speed synchronized to the stator excitation frequency. An important consideration is that its rotor takes discrete steps in aligning its rotor magnetic axis to the energized stator teeth. For a continuously-rotating operation, this stepwise rotation may produce an undesirable torque-dip between phase commutations resulting in a non-smooth operation [17]. Despite its advantages of utilizing a simple and robust rotor structure, the SRM suffers from high torque ripple, loud acoustic noise and a position sensor requirement which are all dependent on the employed motor control strategy [18]. Also the SRM's doubly salient structure would require a new manufacturing technology and a special inverter topology [9]. However, design improvements have been made by increasing the number of stator phases to reduce the unwanted torque dip at the cost of higher control complexity [17].

### 1.2.2.2. Synchronous Reluctance Motors

Another type of a variable reluctance machine is one with a salient rotor structure and a cylindrical stator. First introduced by Kostko as the *reaction synchronous motor*, its stator produces a rotating field as opposed to its doubly-salient SRM counterpart [12]. Kostko's rotor in Figure 4 includes multiple iron laminations separated by insulated air layers to create a high magnetic saliency. Through an ideal set of sinusoidally-distributed coils excited by balanced sinewave currents, a smoothly-rotating stator field is produced in order to force the salient rotor to rotate and align its primary magnetic axis with the stator field. This helps to minimize the overall reluctance path between the stator and rotor structures thereby producing reluctance torque. Over the years, there have been multiple names associated with this singly-salient machine topology: *Synchronous Reluctance Machine* (SynRM, Synchrel), *Reluctance Synchronous Machine* (RSM), and *Reluctance Machine* (RM). For simplicity and consistency, the *Synchronous Reluctance Machine* (SynRM) name is maintained throughout this thesis.

Since this synchronous machine does not simply start at synchronous speed, an asynchronous operation is required to rise the motor speed from zero before locking it to synchronism. One approach is to incorporate a squirrel-cage within the SynRM rotor to enable line-start operation through the electromagnetic induction principle. The asynchronous rotor is always slower than the stator rotating field measured by the slip. Different SynRM rotors with squirrel-cage structures are illustrated in Figure 5 (a), (b) and (c). Before variable-speed drive technologies, this method was widely used to help to produce considerable starting torque and bring its speed close to synchronism speed before switching to synchronous reluctance operation [15].

Due to the advancement of modern power electronics in the past decades, newly developed motor control methods, such as *Field-Oriented Control* (FOC), enabled variable frequency and motor speed operation. By using the rotor's orientation or angular position at any synchronous speed as an additional reference signal, it is possible to accelerate the motor from zero speed by varying the angular speed of the rotating stator field speed through the excitation's electrical frequency. A SynRM may then operate at different torque levels over a wide speed range. This FOC strategy eliminates the need for a line-start cage in exchange for a rotor position sensor or sensorless position techniques [19]. For example, the SynRM rotor structures without line-start cages in Figure 5 (d), (e) and (f) employ a high number of iron lamination and air insulation layers in an alternating manner to increase the rotor saliency and ability for sensorless position control.

---

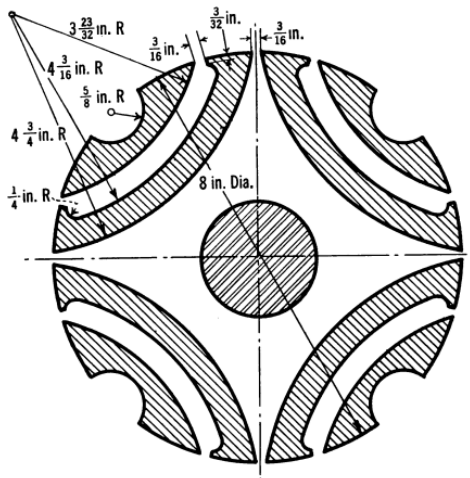


**Figure 4. Kostko's Rotor for the Reaction Synchronous Motor [12]**

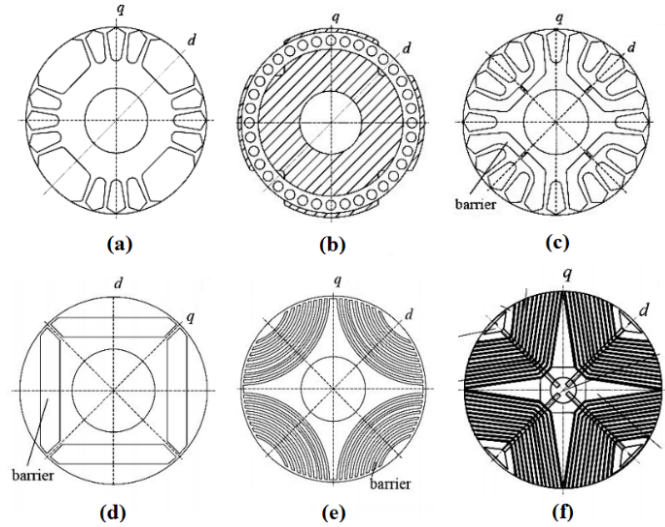


**Figure 5. Evolution of the SynRM Rotor [14], [20]**

The Induction Machine has also emerged as a suitable candidate for variable speed applications with high control accuracy. Previous works have attempted to compare IMs with SynRMs [18], [21]. For the same motor volume in low-power applications, SynRMs produce higher torque and efficiency levels at rated operation due to the elimination of the line-start cage. The SynRM can operate at a higher rated current for the same winding temperature with smaller rotor losses. This comparison has also been experimentally validated through ABB's recent SynRM production line ranging from 17 to 350 kW in output power. ABB have demonstrated that their SynRMs have a smaller frame size and higher efficiency levels than their IMs for supplying the same torque [22]. A smaller SynRM rotor size also correlates with a faster dynamic performance. Other advantages include: synchronous speed behavior, simple rotor manufacturing using existing IM infrastructure, and low material cost due to absence of expensive rare-earth magnets [9].

While the superiority of SynRMs over IMs has been validated in practice, SynRMs suffer from lower power factor, limited CPSR and high torque ripple as reported in [10], [23], [24]. These limiting conditions require inverter  $kVA$  oversizing and increasing the initial system costs which suggests a negative perspective in meeting the technical targets set down in Table 1. A simple, but effective approach to alleviate the low power factor and CPSR problems is to insert low-cost magnets within the SynRM rotor. This procedure follows after optimizing the SynRM's reluctance torque with respect to the geometry of the rotor flux barriers using simulation procedures. As discussed below, there are computational and other challenges that need to be addressed during the design optimization of Synchronous Reluctance Machines.

### 1.3. Thesis Objectives

In this thesis, a low-cost hybrid design of a Synchronous Reluctance Machine is considered to meet a given set of drivetrain requirements. Since a pure SynRM cannot directly compete with an IPM motor's torque-to-rotor volume density, efficiency and CPSR, these limitations are alleviated by using low-cost PMs within the SynRM rotor to produce a *PM-assisted SynRM*. Compared to an IPM motor, there is a fundamental difference in the torque production: a PM-assisted SynRM relies more on reluctance torque than its PM component.

Although [16], [24], [25], [26] have similarly modelled PM-assisted SynRMs using both analytical and numerical approaches, mutual considerations of multiple geometrical parameters have not been explored in detail. This thesis focuses on studying the mutual effects of SynRM rotor geometries and provides an alternative SynRM design methodology to illustrate the motor's performance variation over its rotor geometric space. Using this methodology allows potential motor engineers to validate whether a suggested rotor model is globally optimal using an analytical function, and to visualize the performance tradeoffs and the associated parameter sensitivities in the design plane. During the proposed procedure, the computational bottlenecks in the design optimization of a PM-assisted SynRM rotor are also addressed.

Hence, the thesis's structure is as follows. Chapter 2 reviews the fundamental theory of electric drives including inverter-driven systems and synchronous machines. Different motor control strategies and analysis methods are described before defining the case study for a direct-drive application. A systematic methodology for global optimization of a single-barrier SynRM rotor geometry using artificial intelligence and genetic algorithm methods is presented in Chapter 3. The optimized solutions are validated using accurate numerical simulations. In Chapter 4, the local optimization of the global optimal model is performed. The space mapping from a single-barrier to a multiple-barrier rotor generalization is discussed to further improve the SynRM reluctance torque performance. Next, one of the optimal SynRM rotor solutions is chosen in §4.3 to assist its torque production by inserting low-cost permanent magnets. The final PM-assisted SynRM model is then compared with the initial case-study motor before presenting a robustness analysis. This step-by-step design methodology helps to achieve performance levels close to IPM motors by optimizing the reluctance torque, while introducing useful PM torque for high-speed operation in traction applications. Finally, Chapter 5 discusses the work's conclusion and future considerations.

## Chapter 2 THEORY OF ELECTRIC DRIVES

### 2.1. Introduction

The previous chapter introduced the challenges and opportunities in the automotive industry with an emphasis on the design of the electric traction motor. The market's need for a cheaper electric drive system with a high performance criteria is motivated by mutually optimizing the electric motor and inverter systems. In this chapter, the theory of inverter-driven systems in §2.1.1 and synchronous machines in §2.1.2 are presented. Next, different motor control strategies are discussed under §2.2 before briefly reviewing simulation and analysis methods in §2.3 used for characterizing motor performances. A case study presented in §2.4 is used to demonstrate the optimization procedure for a direct-drive application.

#### 2.1.1. Inverter-Driven Systems

In electric drives, voltage-driven sources are required to operate electric motors. Figure 6 below shows the block diagram of a typical drive system for a synchronous motor.

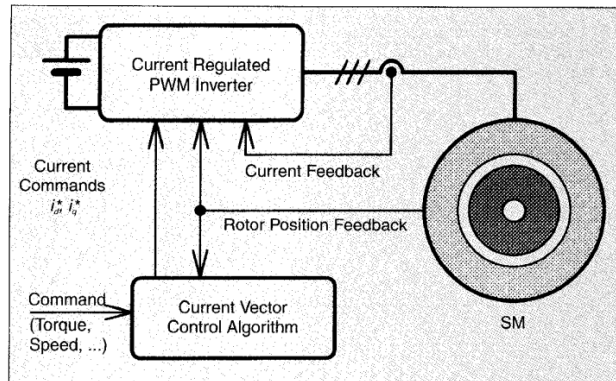
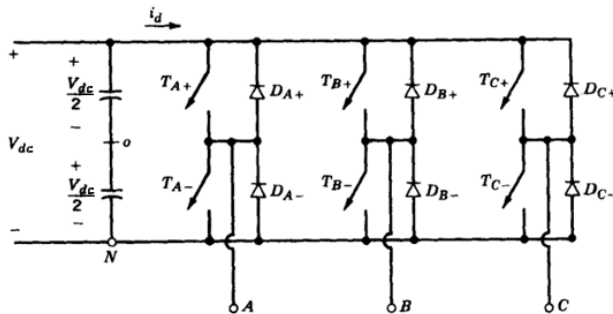


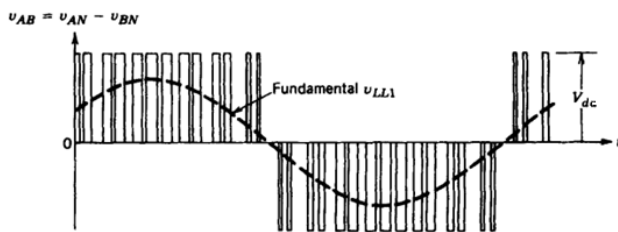
Figure 6. Typical Schematic of a Synchronous Motor Drive System [27]

A constant DC link or bus voltage, usually a battery supply, is connected directly to a closed-loop current regulated *Pulse-Width-Modulated* (PWM) inverter. By connecting each output phase of the PWM inverter between the DC link voltage and ground for different pulse widths, the output signal attempts to emulate a sinusoidal waveform in its fundamental component in order to excite the motor windings. The feedback signals include the phase currents and the rotor position, usually through hall-effect sensors, encoders, resolvers, or sensorless position techniques [19]. A separate current vector control algorithm accepts the command input torque and speed signals to produce the appropriate PWM inverter control signals.

The inverter operation is demonstrated through a *Sine-PWM* method of a simple *3-phase 2-level* inverter shown in Figure 7 (a). By converting a constant DC link voltage  $V_{dc}$  into a balanced *3-phase* PWM voltage signal, the inverter can drive the motor phase windings at a particular switching frequency. A balanced PWM switching allows for voltage amplitude and frequency control. The output voltage amplitude is modulated by comparing a triangular carrier waveform with a control sinusoidal voltage, while the output frequency is varied by changing the carrier signal's frequency and transistor switching frequency. Every inverter leg of the *3-phase* output consists of power transistors such as IGBTs and MOSFETs. In the case of *phase A*, the upper transistor (e.g.  $T_{A+}$ ) connects the phase output to  $V_{dc}$ , and the lower transistor (e.g.  $T_{A-}$ ) connects the phase output to ground. At any given time of the *2-level* inverter operation, each phase output is either connected to the  $V_{dc}$  supply or ground. For this *3-phase* inverter operation, each output phase voltage is  $120^\circ$  out of phase with other phases and a PWM line-to-line waveform  $V_{AB}$  similar to Figure 7 (b) is obtained. The fundamental component buried within the PWM voltage replicates a sinusoidal waveform, while the visible PWM switching introduces unwanted harmonics into the terminal voltage supply. Figure 8 shows the amplitude of the fundamental voltage  $V_{LL1}$  with respect to  $V_{dc}$  as a function of the amplitude modulation index  $m_a$ . Using higher order inverter topologies (e.g. *3-level*) can improve the inverter efficiency by increasing the switching frequency [28].



(a)



(b)

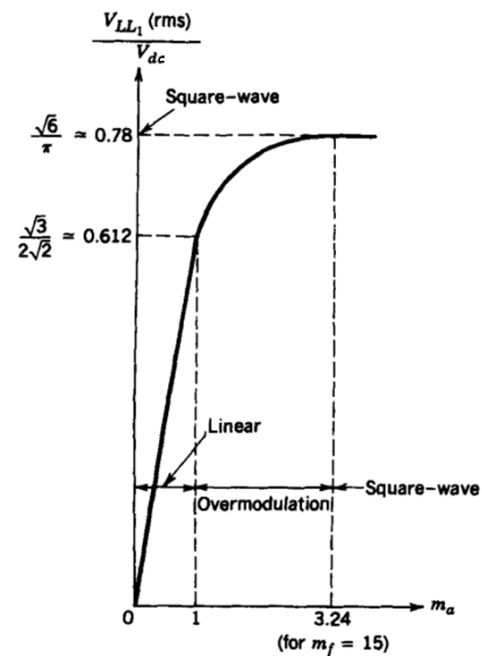


Figure 7. *3-Phase 2-Level* Inverter (a) Schematic, (b) PWM Waveform with Fundamental [29]

Figure 8. *3-Phase* Inverter Voltage-Control Ranges through Modulation [29]

For a given carrier frequency, there are three distinct voltage-control regions in Figure 8 which signify how much the fundamental component of the line-to-line PWM waveform can be amplified with respect to  $V_{dc}$ . The maximum possible voltage increase between the line-to-line RMS and  $V_{dc}$  is  $\sqrt{6}/\pi$  at the square-wave operation boundary. By converting the line-to-line RMS into its per-phase instantaneous voltage, this ratio becomes  $2/\pi$  which is the maximum available per-phase fundamental component of the drive voltage  $V_s^{MAX}$  with respect to  $V_{dc}$ . This value is later used in (15) of §2.2.3 as a drive voltage limitation.

Moreover, an inverter's size is dictated by its topology and individual transistor ratings: the maximum voltage and current ratings set down the inverter's  $kVA$  capability which contributes to the inverter cost [10]. From the perspective of a motor designer, the lagging power factor of the electric motor is used to oversize the inverter's  $kVA$  rating for the worst-case supply scenario.

### 2.1.2. Synchronous Machine Theory

A Synchronous Reluctance Machine consists of a traditional Induction Machine stator with sinusoidally-distributed windings and a singly-salient anisotropic rotor. Through the reluctance torque principle, the unaligned anisotropic rotor is forced to rotate and align itself with the stator magnetic field, also known as stator *magnetomotive force* (MMF). Once the rotor's magnetic axis is aligned directly with the stator MMF, the overall magnetic reluctance path is minimized and the rotor no longer needs to rotate. If it is desired to rotate continuously, the stator MMF must rotate continuously to ensure that the rotor's magnetic axis is never aligned. During the steady-state time, the mechanical rotor speed  $N$  is synchronized to the stator's rotating MMF through the excitation's angular frequency  $\omega_e$  and the rotor number of poles  $n_p$ .

To understand the electromechanical operation of a PM-assisted SynRM, a traditional IM stator with sinusoidally-distributed windings is assumed for generating a sinusoidally-rotating MMF in the air-gap. As discussed in previous papers [30], [31], [32], Park's synchronous machine equations [33] without field and damper windings, core losses, and cross-coupling effects are used to derive the PM-assisted SynRM  $dq$  equations of the stator current in (1), the stator flux linkage in (2) and the stator voltage in (3) in the rotor's reference frame.

$$\bar{I}_s = \begin{bmatrix} I_d \\ I_q \end{bmatrix} = I_s \begin{bmatrix} -\sin \gamma \\ +\cos \gamma \end{bmatrix} \quad (1)$$

$$\bar{\lambda}_s = \begin{bmatrix} \lambda_d \\ \lambda_q \end{bmatrix} = \begin{bmatrix} L_d & 0 \\ 0 & L_q \end{bmatrix} \bar{I}_s + \begin{bmatrix} \lambda_m \\ 0 \end{bmatrix} \quad (2)$$

$$\bar{V}_s = R_s \bar{I}_s + \frac{d\bar{\lambda}_s}{dt} + j\omega_e \bar{\lambda}_s = \begin{bmatrix} V_d \\ V_q \end{bmatrix} = \begin{bmatrix} R_s + pL_d & -\omega_e L_q \\ \omega_e L_d & R_s + pL_q \end{bmatrix} \begin{bmatrix} I_d \\ I_q \end{bmatrix} + \begin{bmatrix} 0 \\ \omega_e \lambda_m \end{bmatrix} \quad (3)$$

Here, the stator current vector  $\bar{I}_s$  consists of the  $d$ - and  $q$ -axis components  $I_d$  and  $I_q$ ,  $\gamma$  is the current advance angle measured counterclockwise from the  $q$ -axis, the stator flux linkage vector  $\bar{\lambda}_s$  consists of the  $d$ - and  $q$ -axis components  $\lambda_d$  and  $\lambda_q$ ,  $\lambda_m$  is the PM flux linkage,  $L_d$  and  $L_q$  are the  $d$ - and  $q$ -axis stator inductances, the stator voltage vector  $\bar{V}_s$  consists of the  $d$ - and  $q$ -axis components  $V_d$  and  $V_q$ ,  $R_s$  is the stator winding resistance, and  $\omega_e$  is the electrical angular speed. The steady-state vector diagram of current, flux linkage and voltage using (1), (2) and (3) is represented in Figure 9 for a general PM-assisted SynRM or even an IPM motor.

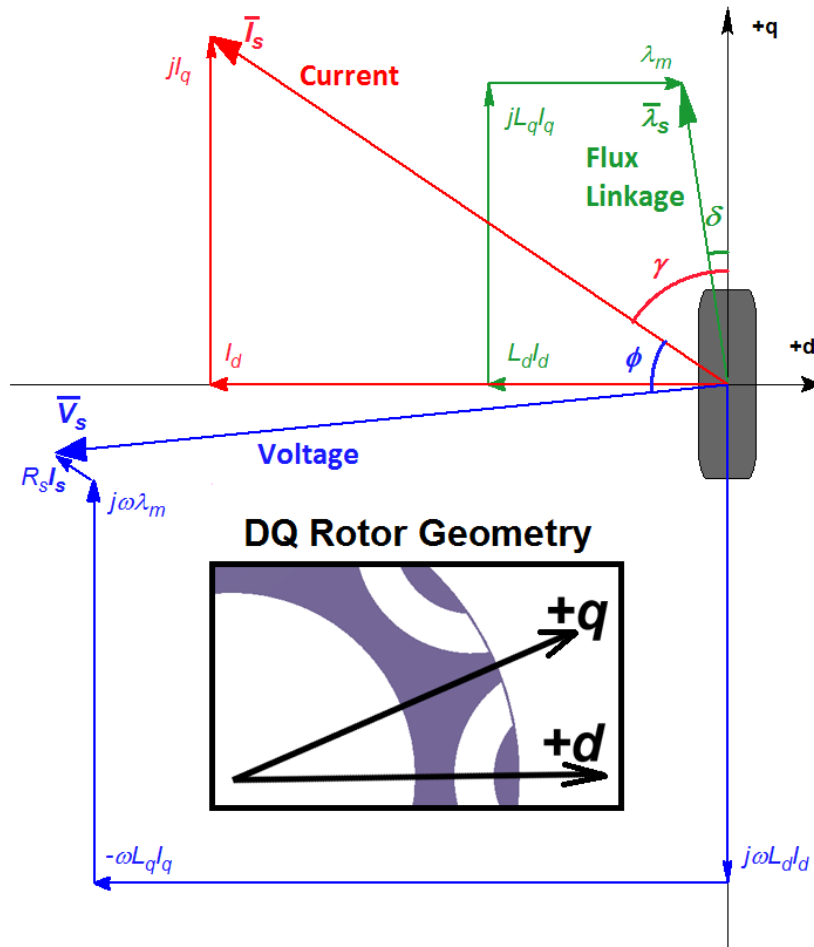


Figure 9. Vector Diagram of a PM-Assisted SynRM without Rotor Core Losses: partial rotor cross-section demonstrates its  $dq$ -axes

During a balanced motor operation, this rotor  $dq$ -frame representation converts the varying motor quantities into constant values. This change of variable representation greatly simplifies the motor control and analysis. The employed  $dq$ -axis convention has been followed from [25], [30] and [34], where the highest inductance (or minimum reluctance) path is aligned along the  $q$ -axis. For a motoring operation, the stator current vector  $\bar{I}_s$  lies in the second-quadrant of the  $I_d$ - $I_q$  plane where  $-I_d$  demagnetizes the rotor field.

From Figure 9, it can be seen that the back-emf vector ( $\bar{V}_s$  vector without the  $R_s\bar{I}_s$  winding loss), which is comprised of the inductive and PM flux linkage components, is perpendicular to the  $\bar{\lambda}_s$  vector. This steady-state vector diagram also provides a useful visual tool to analyze the relationships between the different electromagnetic vectors: the power factor angle  $\phi$  is measured between the current and voltage vectors, and the load angle  $\delta$  is measured from the  $q$ -axis to  $\lambda_s$ .

If the  $\bar{I}_s$  vector is closer to  $\bar{V}_s$  (higher power factor), the inverter is then oversized by a smaller amount implying lower system costs. Also, the  $j\omega L_d I_d$  component dictates how far the  $\bar{V}_s$  vector is vertically from the  $\bar{I}_s$  vector which is mostly responsible for a lower power factor. Ideally, the  $d$ -axis inductance  $L_d$  is desired to be minimized to restrain this undesired effect. Since  $I_d$  is fixed for a given  $\omega_e$  operation, the  $d$ -axis inductance may be minimized to increase the power factor. However due to rotor geometric limitations, it may not be possible to further decrease the  $L_d$  value as explained in §2.2.2. A power factor correction approach is to incorporate a vertical PM flux linkage component  $j\omega\lambda_m$  to bring the  $\bar{V}_s$  vector closer to the  $\bar{I}_s$  vector. This serves as the basis for PM-assisted SynRMs with higher power factor and torque production capabilities.

For a 3-phase motor and a given number of rotor poles  $n_p$ , the electromagnetic torque  $\bar{T}_{em}$  along the  $\hat{z}$ -axis of the rotor shaft in (4) can be calculated through the cross product of the stator flux linkage vector  $\bar{\lambda}_s$  in (2) with the stator current vector  $\bar{I}_s$  in (1). This  $\bar{T}_{em}$  equation in (4) is expanded using (1) to isolate the PM torque  $\bar{T}_{pm}$  and reluctance torque  $\bar{T}_{rel}$  components in (5) as functions of the  $dq$ -axis inductances,  $\lambda_m$ ,  $I_s$  and  $\gamma$ .

$$\bar{T}_{em} = \frac{3}{2} n_p (\bar{\lambda}_s \times \bar{I}_s) = \frac{3}{2} n_p (\lambda_d I_q - \lambda_q I_d) \hat{z} \quad (4)$$

$$\bar{T}_{em} = \bar{T}_{pm} + \bar{T}_{rel} = \frac{3}{2} n_p \left\{ \lambda_m I_s \cos \gamma + \frac{1}{2} (L_q - L_d) I_s^2 \sin 2\gamma \right\} \hat{z} \quad (5)$$

Different classes of synchronous machines can be analyzed through (5). By setting  $L_d=L_q$  along with a non-zero PM flux linkage  $\lambda_m \neq 0$ , a pure PM machine is obtained with no rotor saliency. This means that no reluctance torque can be produced using this pure PM machine. In the other extreme, setting a zero PM flux linkage  $\lambda_m = 0$  and  $L_d \neq L_q$  provides only a reluctance torque proportional to the rotor magnetic *saliency ratio*  $\xi$  as represented in (6). This saliency ratio  $\xi$  is normally greater than 1 for pure reluctance machines, but strictly equal to 1 for pure PM machines. Under §2.2 and §2.3, it is later shown that the rotor saliency ratio  $\xi$  has a significant effect on the reluctance motor performance, especially on the motor power factor.

$$\xi = L_q/L_d \quad (6)$$

### 2.1.3. Salient Rotor Structures

Before explaining the different motor control strategies, the two types of SynRM's rotor structure are identified: *Axially-Laminated Anisotropic* (ALA) and *Transversally-Laminated Anisotropic* (TLA) rotors as previously shown in Figure 3 (b) and (c) respectively.

The rotor  $d$ -axis is oriented towards the maximum reluctance path, while the rotor  $q$ -axis is pointed to the minimum reluctance path. ALA rotors are constructed by stacking multiple axially-laminated steel sheets in the radial direction, while TLA rotors employ regular rotor laminations in the transverse direction. The ferromagnetic layers usually consisting of iron segments are known as *flux carriers*, while the insulated layers usually consisting of air (or magnets in the case of PM-assisted rotors) are called *flux barriers*. The ALA rotor structure has a higher  $\xi$  value than the TLA type as reported in [20], since the ALA  $d$ -axis inductance is smaller. Nowadays the TLA structure is preferred, because it employs standard iron lamination cutting similar to an Induction Machine stator manufacturing process [9].

To provide structural integrity at high speed operation, the multiple flux barriers need to be connected through the radial and tangential iron ribs. However these structural ribs introduce cross-saturation, or cross-coupling, of the  $dq$ -axes of the magnetic flux thereby affecting the motor's mathematical model accuracy during the implementation of a control strategy [35]. This cross-coupling effect is especially prominent in high electric loadings of heavy-duty applications. If the structural ribs are kept small enough relative to the rotor geometry, this cross-coupling effect is minimized to simplify the SynRM design and analysis.

## 2.2. Motor Control Strategies

For a given electric drive with limited inverter  $kVA$  capability, the ideal motor characteristics against speed are visually represented in Figure 10. Below the motor's rated speed, the output torque is kept constant under the constant torque region.

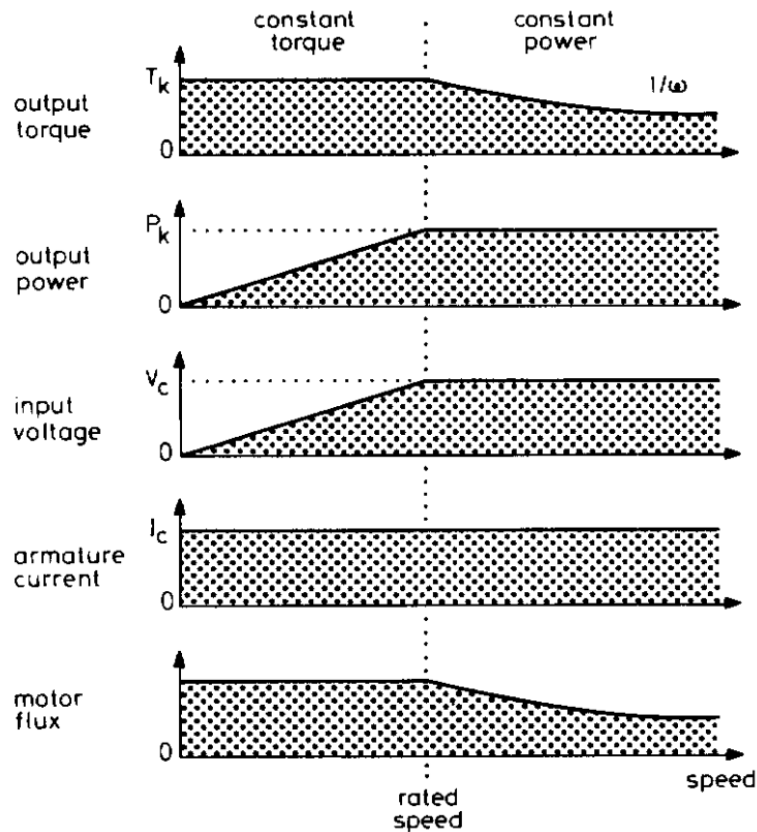


Figure 10. Ideal Drive Characteristics for Different Motor Speeds [36]

During this mode of operation, both the armature or excitation current and the motor flux are maintained. As the motor speed is increased up to the rated condition, the output power and input voltage increase linearly until the motor's back-emf is equal to the terminal voltage. Above the rated speed, the input voltage can no longer grow beyond the motor's back-emf, so it is kept constant by decreasing the motor flux. If the excitation current is maintained at the same time, the output power is kept constant as well. This ensures that the output torque follows a speed-reciprocal ( $1/\omega$ ) relationship in the constant power or *Field-Weakening* (FW) region [36].

In §2.2.1, §2.2.2 and §2.2.3, the different control strategies are discussed with respect to the ideal drive characteristics in Figure 10. Comparison of the final drive's performance with the presented ideal characteristic is later discussed under §4.3.2.

### 2.2.1. Maximum-Power-Factor Control

Previous works reported in [13] and [20] have shown that the rotor saliency ratio  $\xi$  directly contributes to increasing the motor's power factor. By ignoring the effect of the number of rotor poles and winding phases, the per-unit steady-state torque components can be rewritten for a pure reluctance machine in (7) and for a pure PM machine in (8).

$$T_{rel,pu} = (L_d - L_q)I_d I_q = \frac{1}{2}L_d(\xi - 1)I_s^2 \sin 2\gamma \quad (7)$$

$$T_{pm,pu} = \lambda_{mn}I_s \cos \gamma \quad (8)$$

For a given stator current magnitude and advance angle, the per-unit reluctance torque  $T_{rel,pu}$  is a function of  $\xi$  by safely assuming that the  $d$ -axis inductance is approximately constant for different currents (refer to Figure 13) [37]. In the case of per-unit PM torque  $T_{pm,pu}$ , it is only a function of the normalized PM flux linkage  $\lambda_{mn} = \lambda_m/\lambda_s$  with respect to the total stator flux linkage  $\lambda_s$ . Both independent parameters  $\xi$  and  $\lambda_{mn}$  assume that the two torque components are decoupled. They are later used in the IPM parameter plane analysis of §2.3.2 to compare different drives in §4.3.3.

For a pure reluctance machine, its power factor  $\cos \phi$  in (9) is defined as the ratio between active and apparent power using (1), (2), (3) and (7). To simplify (9), the power factor is represented with respect to the variable  $k_\gamma = I_d/I_q$  which is closely related to the advance angle  $\gamma$ .

$$\cos \phi = \frac{T_{rel,pu}\omega_e}{V_s I_s} = \frac{(\xi - 1)k_\gamma}{\sqrt{(\xi^2 + k_\gamma^2)(1 + k_\gamma^2)}} \quad (9)$$

In order to maximize the power factor for an advance angle  $\gamma$ , (9) is differentiated with respect to the  $k_\gamma$  current ratio to find the optimal operating point shown in (10) and (11).

$$\frac{d \cos \phi}{dk_\gamma} = 0 \rightarrow k_\gamma = \sqrt{\frac{L_q}{L_d}} = \sqrt{\xi} \rightarrow \cos \phi^{MPF} = \frac{\xi - 1}{\xi + 1} \quad (10)$$

$$\gamma^{MPF} = \tan^{-1} \sqrt{\xi} \quad (11)$$

This SynRM relationship dictates the *Maximum-Power-Factor* (MPF) control which depends on the rotor saliency ratio  $\xi$ . Figure 11 illustrates the relationship between the *Maximum Power*

---

Factor and the rotor saliency ratio  $\xi$  using (10) and (11). For example,  $\cos \phi^{MPF} = 0.8$  for  $\xi = 7$  and  $\gamma^{MPF} \approx 69^\circ$ . If another advance angle  $\gamma$  is selected different from the optimal  $\gamma^{MPF}$ , a saturation curve similar to Figure 11 is observed but with a smaller steady-state value.

While maximizing the saliency ratio has major implications on inverter sizing, [20] reported unsaturated saliency ratios lower than 10 for practical ALA rotors. These ALA rotors can operate at high torque and power factor levels at the expense of mass manufacturing complexity and cost [16]. Figure 12 demonstrates a general construction of an ALA rotor where multiple iron laminations are stacked radially from the inner shaft and held together at each end. In the case of TLA rotors, high saliency ratios of 7 and greater are not feasible during high current excitations. Nevertheless, TLA types are still preferred for their suitability in simpler industrial manufacturing using regular transverse iron laminations as its stator.

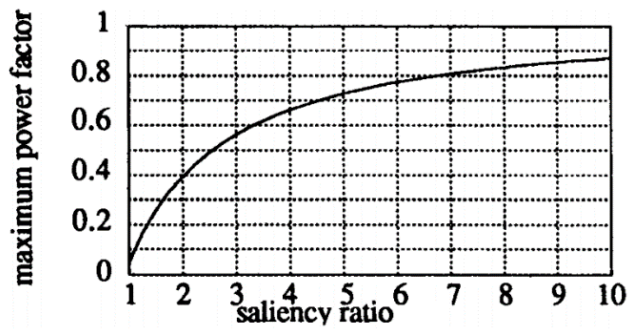


Figure 11. MPF versus Saliency Ratio [13]

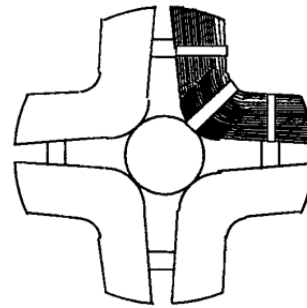


Figure 12. General ALA Rotor Construction [13]

### 2.2.2. Maximum-Torque-Per-Ampere Control

Ignoring the effect of rotor PMs and cross-coupling, the  $dq$ -axis inductances are noted to be dependent on the stator winding current level  $I_s$ . An example of this relationship is illustrated in Figure 13 for a 7.5 kW ALA rotor with an unsaturated saliency ratio  $\xi$  of 11.5. The  $L_d$  inductance may be assumed to be approximately constant, with slight variations existing due to the level of cross-coupling between the  $dq$ -axes. This constant  $L_d$  assumption is valid for high saliency ratios such that the rotor  $d$ -axis does not allow more leakage flux to pass through. At higher current or load levels, the main rotor iron paths along the rotor  $q$ -axis saturate, thereby decreasing the  $L_q$  inductance and the saliency ratio  $\xi$ . Hence the  $q$ -axis inductance  $L_q$  and the  $(L_q - L_d)$  inductance difference are both functions of the stator current magnitude  $I_s$  and advance angle  $\gamma$ . For TLA

rotors, the  $L_d$  inductance value is higher due to more leakage flux passing through the flux barriers and the radial structural ribs.

In addition, the per-unit reluctance torque  $T_{rel,pu}$  relationship in (7) may be analyzed for different winding excitations. The per-unit reluctance torque is a function of three parameters: the saliency ratio  $\xi$ , the stator current magnitude  $I_s$  and the current advance angle  $\gamma$ . By fixing the  $I_s$  value for a given SynRM, single values from a  $dq$ -inductance graph similar to Figure 13 are chosen to calculate  $\xi$ . This reduces the number of independent parameters to only  $I_s$  and  $\gamma$  for a fixed rotor structure. Figure 14 shows that for a constant current  $I_s$ , the torque-per-ampere curves always follow a concave relationship with a local maximum with respect to the advance angle,  $\gamma$ .

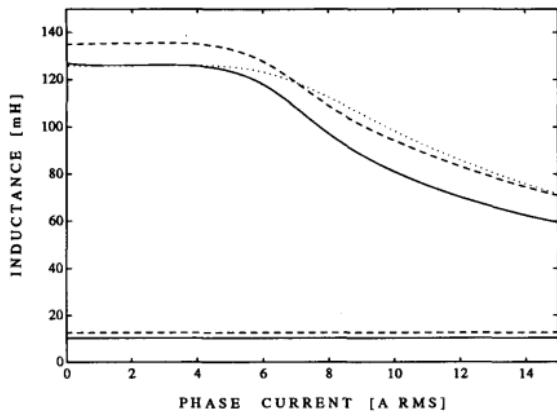


Figure 13. Relationships between  $L_d$  (lower) and  $L_q$  (upper) Inductances with  $I_s$  [38]

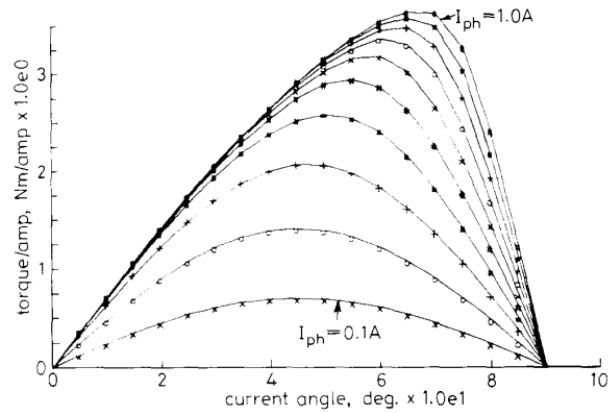


Figure 14. MTPA Variation with Current Angle  $\gamma$  for Different Currents  $I_s$  [38]

This implies that an optimal  $\gamma$  operation point exists such that it maximizes the output reluctance torque for a given current level  $I_s$ , known as the *Maximum-Torque-Per-Ampere* (MTPA) control strategy. At high currents, the torque-per-ampere curves shear toward  $90^\circ$  due to the saturating  $q$ -axis inductance. The maxima MTPA points require higher current angles in order to demagnetize the saturated rotor iron paths and allow the motor to run at higher torque. Considering the maxima points for a range of stator currents, the MTPA-current trajectory follows a nonlinear relationship which requires knowledge of the  $dq$  inductance for any  $I_d$  and  $I_q$ . Increasing  $\gamma$  demagnetizes the rotor which introduces additional rotor losses and decreases the motor's efficiency.

By using the per-unit PM torque in (8) with the per-unit reluctance torque (7), the current angle  $\gamma$  is decreased to maximize the total per-unit torque. This requires the mutual maximization of  $\cos \gamma$

and  $\sin 2\gamma$  in order to produce more torque at a higher efficiency level. This PM-assisted SynRM case becomes particularly important during high speed operation of Flux-Weakening control.

### 2.2.3. Flux-Weakening and Maximum-Torque-per-Volt Control

The MPF and MTPA control strategies provide a useful means to operate Synchronous Reluctance Motors with specified saliency ratios at different current levels. Nevertheless, the effect of the rotor angular speed on the control strategies has not yet been considered.

The available per-phase fundamental component of the motor voltage  $V_s$ , also known as the voltage-limit, can be represented in (12) using its  $dq$ -axis components [30]. During the steady-state, the maximum current-limit is similarly defined in (13).

$$V_s^2 = V_d^2 + V_q^2 \quad (12)$$

$$I_s^2 = I_d^2 + I_q^2 \quad (13)$$

Expanding (12) using the stator voltage in (3) during steady-state and ignoring the winding losses, the voltage-limit equation can be written in (14) in terms of the electrical angular speed  $\omega_e$ , the  $dq$ -axis currents, the rotor saliency ratio  $\xi$  and the PM flux linkage  $\lambda_m$ . Referring back to Figure 8, the maximum  $V_s$  is related to the DC link inverter input voltage  $V_{dc}$  through (15). This occurs at the boundary of the inverter's square-wave operation during voltage-amplitude modulation.

$$\left(\frac{V_s}{\omega_e L_d}\right)^2 = I_q^2 + \xi^2 \left(I_d + \frac{\lambda_m}{L_d}\right)^2 \quad (14)$$

$$V_s^{MAX} = \frac{2}{\pi} V_{dc} \quad (15)$$

Referring to the  $(I_d, I_q)$  plane of the Figure 15 mode diagram, a current-limit circle centered at the origin is plotted using (13) for a given  $I_s$  magnitude. The constant-torque hyperbolas are plotted using (5) to illustrate the feasible operational points for any rotor speed. Multiple voltage-limit ellipses are displayed using (14) for different rotor speeds. The voltage-limit ellipses are observed to be centered at  $-\lambda_m/L_d$  with its eccentricity governed by  $\xi$ . A higher saliency ratio value further stretches the voltage-limit ellipse along the  $d$ -axis. Note that the rotor speed  $N$  grows by increasing the value of  $\omega_e$  through the inverter drive frequency ( $\omega_e = (\pi/60)n_p N$ ).

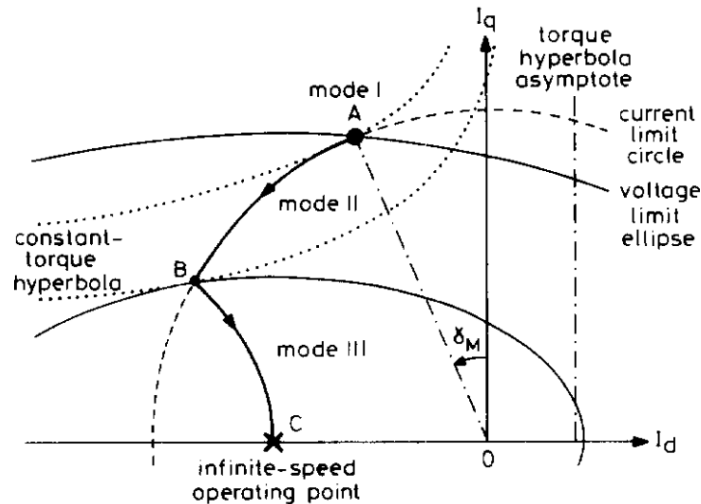


**Figure 15. Mode Diagram including the Maximum Torque Trajectory (bold) for Zero to Infinite Speeds. Mode I: MTPA, Mode II: FW, Mode III: MTPV [36]**

Given that the size of the voltage-limit ellipse shrinks for increasing rotor speeds through (14), this smaller ellipse imposes fewer feasible  $dq$  current points. For producing the same torque at a higher speed, the operating  $dq$  current point should move along the constant-torque hyperbola outside the current-circle. However, the current-limit circle does not allow this current magnitude increase. The output torque is then forced to decrease, while the  $dq$  current point shifts along the current-limit circle. This inherent tradeoff between the current-limit circle and voltage-limit ellipse becomes more apparent at higher speeds.

By relying on the different presented motor-drive control strategies, there are mutually-exclusive modes depending on the rotor speed [36]. For simplification, a comparison between the drive characteristic curves in Figure 10 and the mode diagram in Figure 15 is used.

Ranging from zero to rated motor speed, Mode I dictates a current-limited constant-torque region where the maximum torque is obtained for a given operating current magnitude and MTPA advance angle  $\gamma_M$ . The voltage-limit is still not violated, and point A in Figure 15 corresponds to the boundary intersection of the constant-torque hyperbola with the current-limit circle.

After the rated motor speed, Mode II is both current and voltage-limited. Since the voltage-limit ellipse has become smaller at a higher rotor speed, it is no longer possible to sustain the same constant torque at point A. For higher speeds, the torque produced is forced to decrease by moving along the feasible current-limit circle and maintaining constant power. The intersection between the current-limit circle and voltage-limit ellipse is illustrated by the bold trajectory line between

points A and B: the current advance angle  $\gamma$  increases, while the current magnitude  $I_s$  is kept constant. Increasing the current angle  $\gamma$  demagnetizes the motor flux to maintain the same back-emf, thereby naming this strategy as *Flux-Weakening* (FW) control.

Between points B and C, Mode III represents a voltage-limited region to provide the highest torque possible for a limited voltage supply. By intersecting the constant-torque hyperbolas with the voltage-limit ellipse along a tangent, it is theoretically possible to reach an infinite motor speed at point C. This voltage-limited strategy is known as *Maximum-Torque-per-Voltage* (MTPV) control.

For the three control modes presented above, [36] defined five classes of synchronous motors illustrated in Figure 16 for the pure SMPM, pure SynRM and hybrid IPM motors. The SMPM motor only produces PM torque using (8), so its Mode I (MTPA) trajectory moves along the  $I_q$ -axis ( $\gamma = 0^\circ$ ) and its Mode II follows along the current-limit circle. When the voltage-limit ellipse is centered inside the current-limit circle, it is possible to achieve MTPV control using Mode III by moving vertically downwards toward the  $I_q = 0$  line at the ellipse's center point  $-\lambda_m/L_d$  (infinite speed point). For the SynRM or Synchronrel case, the Mode I trajectory linearly follows along an MTPA angle using (7) until the current-limit circle is reached. This trajectory may not necessarily be linear as discussed in §2.2.2. The FW capabilities of Modes II and III are more inhibited for torque production, because the displayed trajectories move toward the origin at theoretically-infinite maximum speeds. In the hybrid case of the SMPM motor and SynRM, the IPM motor or PM-assisted SynRM mode diagram is observed. Its different modes follow similar trajectories while employing both PM and reluctance torque components.

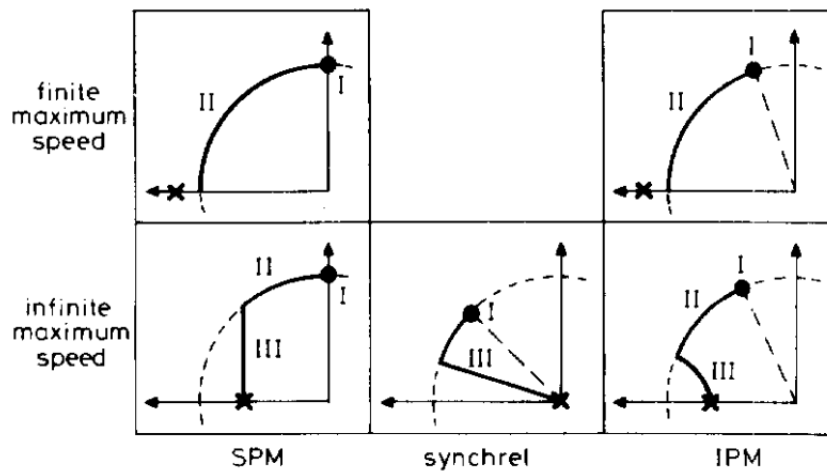


Figure 16. Maximum Torque Trajectories for Five Drive Classes [36]

### 2.3. Analysis and Simulation Methods

The analysis and simulation methods used to compare performances of different SynRM rotors is described below. Presented topics are visited again in subsequent chapters.

#### 2.3.1. IPM Parameter Plane

The IPM parameter plane provides a useful tool to analyze motor performances as functions of two independent parameters. This provides a holistic perspective on choosing a suitable motor to meet specific drive requirements during the design process. For the FW analysis, [36] identified two independent parameters for producing the reluctance and PM torque components: the magnetic saliency ratio  $\xi$  and the normalized PM flux linkage  $\lambda_{mn}$ . By varying  $\xi$  and  $\lambda_{mn}$  across the IPM parameter plane, different normalized power-speed characteristics are calculated as illustrated in Figure 17 (a). The dashed lines represent the ideal power characteristics similar to Figure 10, while the solid curves represent the realistic versions. This IPM parameter plane can also be subdivided into the five SM drive classes of Figure 16 as shown in Figure 17 (b).

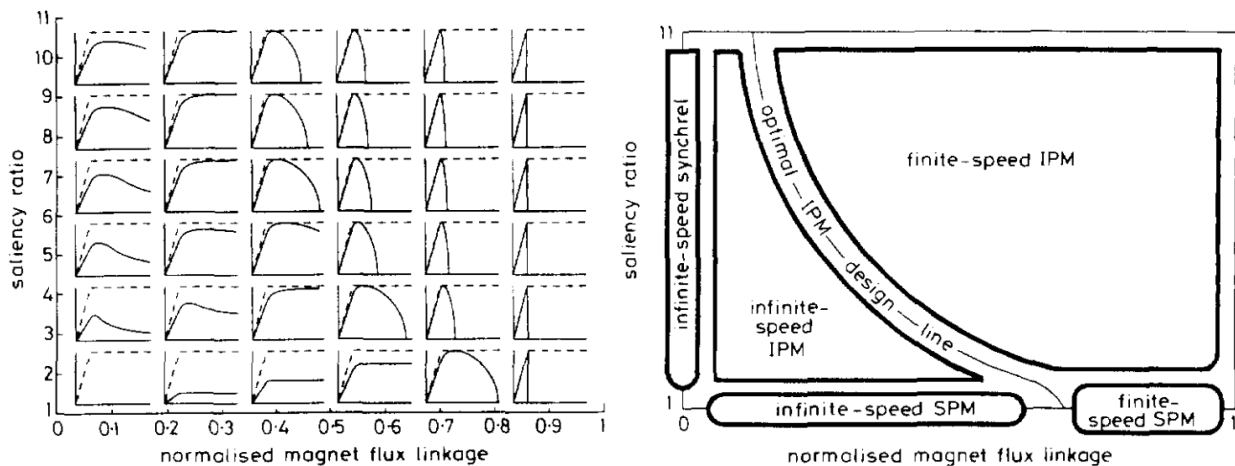


Figure 17. (a) Power-Speed Curves and (b) SM Drive Classes in the  $(\xi, \lambda_{mn})$  Plane [36]

For a wide CPSR capability, it is desired to have an  $(\xi, \lambda_{mn})$  operational point along the *optimal IPM design line* in Figure 17 (b). Assuming a mutually-exclusive design process, it is possible to model a pure SynRM with a high  $\xi$ , before  $\lambda_{mn}$  is increased by inserting PMs within the rotor structure. This helps to optimize the PM-assisted SynRM for a traction application with a desired power-speed characteristic. In addition, the IPM parameter plane is used to analyze various drive performances. One notable result is the *Inverter Utilization Ratio* (IUR) or the normalized rated output power which is the product of the motor power factor  $\cos \phi$  and power efficiency  $\eta$ . Along

the *optimal IPM design line*, it is observed that the IUR contour value tends to about 0.7 and approaches unity for strictly  $\lambda_{mn} = 1$ . Although it is desirable to maximize the IUR, tradeoffs must be made with respect to the CPSR value. The IPM parameter plane is later used in §4.3.3.

### 2.3.2. Insulation Ratio

Similar to using the saliency ratio to estimate the motor power factor, the difference between the  $dq$ -axis inductances ( $L_q - L_d$ ) correlates with the reluctance torque production. An approximate measure to estimate the rotor saturation level is through the rotor insulation ratio  $k_{air,r}$  in (16). This is a ratio between the total insulation width  $W_b$  consisting of non-ferromagnetic material, and the total rotor iron width measured from the inner rotor radius  $D_{ri}/2$  to its outer radius  $D_{ro}/2$ .

$$k_{air,r} = \frac{W_b}{(D_{ro} - D_{ri})/2} \quad (16)$$

A simulated relationship between ( $L_q - L_d$ ) and the  $k_{air,r}$  ratio for two different stator slot numbers presented in [13] seems to suggest that a range between 0.3 and 0.5 for  $k_{air,r}$  produces the highest torque. In fact, [32] has extended the SynRM saturation analysis and introduced the stator insulation ratio  $k_{air,s}$ , which calculates the ratio between the stator slot width and the stator slot pitch. Both insulation ratios should be as close as possible to ensure that the stator and rotor are equally saturated under high currents. When  $k_{air,r} < k_{air,s}$  in [32], the effect of rotor saturation is reported to be more prominent: the average torque, torque ripple, output power, stator tooth loss and back-iron loss were all higher while the power factor was lower. Under Chapter 3, the  $k_{air,r} \approx k_{air,s}$  relationship is later used to ensure equal saturation levels in the stator and rotor.

### 2.3.3. Finite Element Analysis

While magnetic circuit modeling provides analytical approximations to design electric machines with simplified geometries, accurate prediction of motor performances is not always possible. Nonlinear characteristics of magnetic materials, for example fringing, saturation and leakage flux, play a prominent role in the operation of synchronous motors. Through past experiences, these nonlinearities are taken into account through correction coefficients [16].

To ensure a more accurate and reliable calculation of motor performances, a numerical method such as *Finite Element Analysis* (FEA) can account for complex geometries and material

---

nonlinearities. FEA is used to solve a *Partial Differential Equation* (PDE) on a given surface or domain for a set of boundary conditions. In electromagnetic problems such as electric motor design, Maxwell's Equations of Electromagnetism are used to form the underlying PDE. Another benefit of using an FEA tool is its domain discretization: it allows users to easily change the geometric shape, excitation currents, winding configurations, material properties and other motor parameters without altering the problem definition. A brief description of the 2D FEA formulation is described below using [39], [40], [41], [42].

Upon discretizing or meshing the domain into smaller subdomains known as *finite elements*, the values of an unknown field quantity  $\bar{x}$  are solved throughout all nodes using a system of linear equations  $\bar{M}\bar{x} = \bar{b}$ . Finite elements could consist of a combination of triangular and quadrilateral shapes or facets. Triangles are used more often to mesh 2D domains in commercial FEA software packages, because they guarantee full discretization of any arbitrary geometry. If the  $\bar{x}$  values are known to vary more in particular regions of the domain, the geometric mesh is refined (e.g. through *h-refinement*) by generating more smaller-sized triangle elements to ensure that  $\bar{x}$  is solved more accurately. Inside a local element,  $\bar{x}$  is smoothly approximated using a support or basis function of its nodal values through a set of linear, quadratic or higher order polynomials. If the polynomial order of the interpolation function and the number of elements are both increased, the size of  $\bar{x}$  increases as well implying a tradeoff between solution accuracy and computational time.

Once the basis function is defined, the system of finite element equations  $\bar{M}\bar{x} = \bar{b}$  is formed by using either the *variational* (also known as *Ritz method* or *Galerkin's method*). The *variational method* generally formulates the boundary value problem in terms of a functional (a function with a domain of functions) whose minimum corresponds to the PDE with given boundary conditions. On the other hand, *Galerkin's method* obtains an identical set of finite element equations by minimizing the sum of weighted residuals. At first, the residual of a local element is constructed by equating all terms of the PDE to zero. This residual is multiplied by a weight function and integrated over a single element. Next, the residual sum is obtained by summing all the local element residuals. By minimizing the residual sum and assembling all the element matrices into one, the global matrix system is formed with an order corresponding to the total number of unknown field values  $\bar{x}$  at the meshed nodes. For a nonlinear model, matrix  $\bar{M}$  is linearized before

solving for  $\bar{x}$  as an inverse problem. The solution convergence is accelerated if matrix  $\bar{M}$  is sparse. The values of  $\bar{x}$  are then post-processed to explicitly calculate the desired field quantities.

Although many FEA formulations exist, it is worth discussing its transient 2D version including motion effects in (17). Here,  $\bar{\nabla}$  is the gradient operator,  $\bar{\mu}$  is the magnetic permeability vector,  $\vec{A}$  is the magnetic vector potential,  $\vec{\sigma}$  is the electrical conductivity vector,  $\partial/\partial t$  is the partial derivative with respect to time  $t$ ,  $\vec{v}$  is the instantaneous velocity vector and  $V$  is the electric scalar potential.

$$\bar{\nabla} \times (\bar{\mu}^{-1} \cdot \bar{\nabla} \times \vec{A}) + \vec{\sigma} \cdot \left( \frac{\partial \vec{A}}{\partial t} - \vec{v} \times \bar{\nabla} \times \vec{A} \right) = -\vec{\sigma} \cdot \bar{\nabla} V \quad (17)$$

Using the procedure described above, the magnetic vector potential  $\vec{A}$  is treated as the unknown field quantity  $\bar{x}$  before solving it using computationally-fast matrix solvers. In the post-processing stage, the magnetic field density  $\vec{B}$  and magnetic field intensity  $\vec{H}$  vectors are calculated using the vector potential relation in (18) and the constitutive tensor relation of electromagnetism in (19).

$$\vec{B} = \bar{\nabla} \times \vec{A} \quad (18)$$

$$\vec{H} = \bar{\mu}^{-1} \cdot \vec{B} \quad (19)$$

Once the required field quantities are found, the instantaneous electromagnetic torque  $T_i$  on a rotor body is calculated using (20) based on Maxwell's Stress Tensor  $\vec{\sigma}_{MST}$  [40]. This approach, derived from the Lorentz force equation, sums all the local stresses on a bounding air gap surface  $S$  using a surface integral formulation. Here,  $r$  is the radius of the circular path of integration,  $\mu_0$  is the magnetic permeability constant in free space,  $l_{stk}$  is the motor's effective stack length, and  $B_r$  and  $B_t$  are the radial and tangential components of  $\vec{B}$ . Note that only the  $z$ -component of  $T_i$  is non-zero for a balanced motor operation.

$$T_i = \oint_S \left( (\vec{r} \times \vec{\sigma}_{MST}) \cdot d\vec{S} \right) \cdot \hat{z} = \frac{l_{stk}}{\mu_0} \int_0^{2\pi} r^2 B_r B_t d\varphi \quad (20)$$

At another time instant  $i$ , the rotor body moves to a new angular position  $\varphi_i$  and the entire FEA procedure is repeated. In short, the  $(\vec{B}, \vec{H})$  values are calculated using the solved  $\vec{A}$  quantities at all meshed nodes before finding the instantaneous rotor torque  $T_i$  value at a rotor position. This

procedure continues across one electrical period in order to compute the average torque and torque ripple values from the  $T$  waveform. For this thesis, the available *MotorSolve* and *MagNet* software through [43] is used to accurately calculate the instantaneous torque of different SynRM models.

## 2.4. Case Study Definition

To illustrate the design methodologies employed and handle the challenges faced, a case study motor is used as a template to search for an optimal SynRM rotor model. Table 2 below lists the performance specifications of a high-torque, low-speed direct-drive motor typically used for driving heavy duty vehicles such as city buses and delivery trucks. This *TM4 Sumo MD* motor in Figure 18 has a SMPM topology (refer to §1.2.1) with an inner stator and outer rotor configuration for increased torque and efficiency, and better PM retention at higher speeds [44]. It also requires less maintenance by eliminating the need for a vehicle transmission system.

**Table 2. Performance Specifications of a High-Torque, Low-Speed Direct-Drive Motor [44]**

Specification	<i>TM4 Sumo MD</i>
$T_{avg}^{MAX}, T_{avg}^{CONT}$ (Nm)	2100, 1000
$P_{FW}^{MAX}, P_{FW}^{CONT}$ (kW)	200, 180
$\eta^{MAX}$ (%)	95.0
$N_{max}$ (RPM)	3100



**Figure 18. *TM4 Sumo MD* Motor [44]**

Here, the maximum and continuous average torques are defined as  $T_{avg}^{MAX}$  and  $T_{avg}^{CONT}$  respectively, the maximum and continuous output powers in the FW region are correspondingly  $P_{FW}^{MAX}$  and  $P_{FW}^{CONT}$ , the maximum efficiency at minimal operation is  $\eta^{MAX}$ , and the maximum operational speed is  $N_{max}$ . By using *TM4 Sumo MD*'s specifications as objective guidelines and estimating its overall dimensions, an *initial IPM* motor with an inner rotor configuration is modelled. This helps to fix the motor's volume and stator structure for exclusively carrying out the global optimization of the SynRM rotor in Chapter 3. Note that a similar procedure follows for designing other traction motor applications with higher maximum speeds or different sizes.

Figure 19 displays this *initial IPM* motor with V-shaped PMs and listed ratings close to the *TM4 Sumo MD*. Its performances are calculated using FEA simulations and presented along with its

parameters in Table 3. Since its rotor does not use flux barriers, this motor relies more on producing PM torque than reluctance torque which restricts its overloaded current operation. By allowing the rotor geometry to vary using flux barriers and low-grade magnets, its rotor is replaced with a *PM-assisted SynRM* version to address the *initial IPM*'s limitations. The *33-slot* stator configuration and rotor outer diameter are assumed to be fixed in order to emphasize the global rotor design optimization with respect to the reluctance torque component.

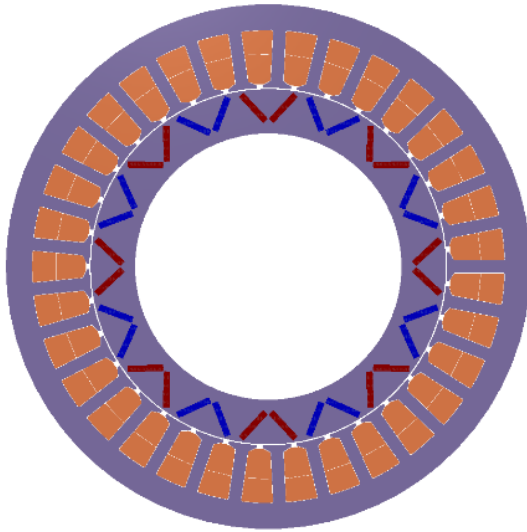


**Figure 19. Cross-Section View of the Initial IPM Motor**

**Table 3. Initial IPM Motor Parameters and Ratings**

Description	Symbol	Value
Number of Stator Slots	$n_s$	33 slots
Stator Outer Diameter	$D_{so}$	325 mm
Stack Length	$l_{stk}$	275 mm
Air Gap Thickness	$W_{ag}$	0.75 mm
Rotor Outer Diameter	$D_{ro}$	220 mm
Rated Line Current	$I_{rated}$	470 $A_{rms}$
Rated Current Density	$J_{rated}$	9.6 $A_{rms}/mm^2$
Net Slot-Fill Factor	$SF_n$	40 %
Supply DC Voltage	$V_{dc}$	450 $V_{dc}$
Cooling Method	Liquid-Cooled	
Rated Rotor Speed	$N_{base}$	700 RPM
Rated Torque	$T_{avg}^{CONT}$	967 Nm
FW Output Power (est.)	$P_{FW}$	160 kW

For the motor model displayed in Figure 19, Table 4 lists its estimated incurred material costs including the rare-earth PMs. It is worth noticing that the NdFeB magnets account for about 60% of the total material cost by using the pricing estimate from [23]. Due to the market volatility and the high expense of rare-earth PMs, it is desired to eliminate their use from the SynRM rotor. In the next chapter, a global rotor design optimization as a function of a pure SynRM's rotor geometric parameters is performed with novel methodologies presented. An overview of the data acquisition and rotor modelling techniques used are also covered.

**Table 4. Initial IPM Motor Material Costs using Material Pricing in [23]**

Material	Unit US\$/kg	Material kg	Cost US\$	Total US\$
NdFeB PM	70.00	5.85	409.50	704.60
Copper	8.50	23.2	197.20	
Stator & Rotor Iron	1.10	35.0 + 54.0	97.90	

## 2.5. Conclusion

In this chapter, a brief theory of inverter-driven systems and general synchronous machines is discussed under §2.1.1 and §2.1.2 respectively. Starting from the fundamental lumped parameter equations in the rotating reference frame, the vector diagram of electrical quantities in the  $dq$ -plane and the  $dq$  electromagnetic torque equation are developed. The motor model is assumed to produce both PM and reluctance torque components leading to five drive classes as illustrated under §2.3.1. A short discussion on the saliency of SynRM rotor structures is also provided before analyzing the relative drive performances of IPM machines. Among the different motor control strategies derived above in §2.2, the Maximum-Torque-per-Ampere and Flux Weakening are primarily used in subsequent analyses as the common basis for fairly comparing various motor designs (especially in §3.2.2, §4.2.3 and §4.3.2). Similarly, the post-processed calculation of the instantaneous torque, based on the computed results of the Finite Element Analysis with its electromagnetic fundamentals explained in §2.3.3, is later described in §3.2.2. Finally, a direct-drive case study presented in §2.4 sets the focus of this thesis study to design the rotor structure of a PM-assisted SynRM in its global and local optimizations of Chapter 3 and Chapter 4 respectively for a set of given requirements.

## Chapter 3 GLOBAL ROTOR DESIGN OPTIMIZATION

### 3.1. Introduction

In the global optimization of a SynRM rotor for reluctance torque, multiple objectives require mutual minimization or maximization to ensure that both a feasible and optimal model is selected. Before discussing a single-barrier design optimization of the SynRM rotor for the presented case study in §3.2, the subsections below briefly review the required concepts in sampling plans, Pareto fronts, initial motor sizing and design challenges.

#### 3.1.1. Sampling Plans

Electric motor optimization problems often require information about the design or search space. As explained under §1.3, it is not computationally efficient to invest in an accurate function evaluator at every iteration of the optimization procedure. A common approach uses sampling techniques to choose specific points in the search space. Using these sampled points, the desired objective values are evaluated using accurate methods and interpolated between the non-sampled points using regression analysis.

Also known as a design of experiment, a *sampling plan* systematically selects points in the specified space in order to maximize the total information acquired [45]. It particularly discretizes the design space to reduce the invested computational effort in exploring less interesting regions. In the literature there are several sampling techniques explored, but this thesis only considers the *full factorial* and *Latin hypercube* techniques for the geometric search spaces.

Let  $m$  be the number of design space variables and  $l$  be the number of sampled levels in each variable. A *full factorial* method uniformly discretizes the  $m$  variables across  $l$  levels for all possible combinations. The total number of acquired samples  $n$  is calculated using (21). Although full factorial sampling is easy to perform and is regularly used for screening experiments (to identify significant design factors), this approach is computationally expensive for higher numbers of variables [45]. An illustrative example of a full factorial sampling for 2 variables across 3 levels is shown in Figure 20 (a) which results in 9 sampled points ( $l^m = 3^2$ ).

$$n = \prod_{i=1}^m l_i \quad (21)$$

An alternative sampling technique is the *Latin hypercube*. In the most basic form, this technique splits the design space into equally-sized hypercubes and inserts samples in them [46]. An important feature of the Latin hypercube is that the sampled points are uniformly spread using “space-filling” measures, such as the maximin metric, as introduced in [47]. If a variable is unneeded and removed, the sampled space is still well-distributed across the other variables. Figure 20 (b) displays an example of a Latin hypercube sampling for 2 variables and 8 points using the maximin distance design [45]. For higher dimension numbers, the Latin hypercube sampling is preferred to distribute the sampled points across the search space.

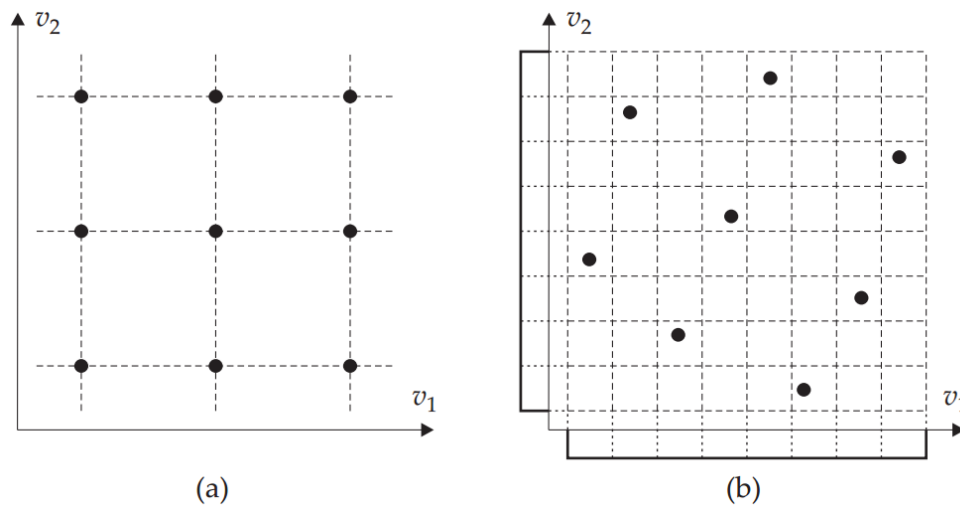


Figure 20. Sampling Plans for 2 Variables: (a) Full Factorial across 3 Levels, (b) Latin Hypercube for 8 Points [45]

### 3.1.2. Pareto Fronts

During a multi-objective optimization, several objectives need to be minimized or maximized while satisfying a set of constraints, resulting in a set of optimal solutions known as the *Pareto front*. At the end of the optimization process, a set of Pareto front solutions are available so that a final design can be chosen. Figure 21 illustrates, by example, the definition of a Pareto front for two objectives. In the 2-dimensional objective space of  $\mathbf{f}_1$  and  $\mathbf{f}_2$ , the squares correspond to the set of all solutions. It is desired to minimize both objectives  $\mathbf{f}_1$  and  $\mathbf{f}_2$  simultaneously. The Pareto front consists of the red dotted line connecting only the dark blue squares, which correspond to the set of global optimal solutions. Note that points A and B are on the Pareto front, while Point C is not. Point C has higher objective values (and is correspondingly worse) to Points A and B. Also the Pareto front demonstrates a tradeoff relationship between the two objectives. A decrease (or improvement) in one objective value results in an increase (or diminishment) of another objective.

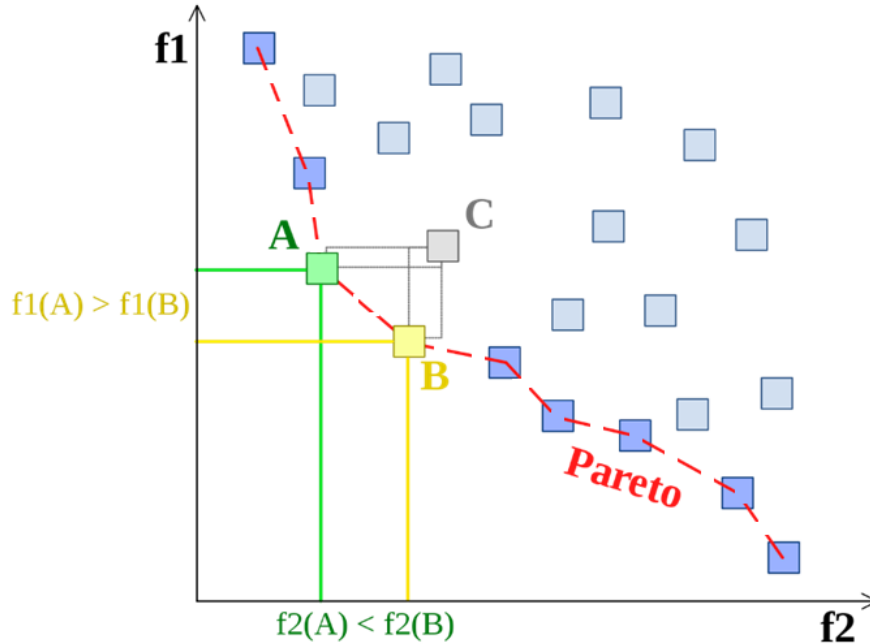


Figure 21. Pareto Front Example of Two Objectives  $f_1$  and  $f_2$  [48]

### 3.1.3. Initial Sizing

Similar to AC motors, Synchronous Reluctance Machines follow the same design principles demonstrated in [34] and [49]. Starting with the presented theory of electric drives and the case study requirements, the sizing of the SynRM is performed according to its torque-per-rotor-volume, or its electric and magnetic loadings. This provides a rough estimate for the relative performance level of the electric machine. Next the stator and rotor core along with the magnet materials are chosen to satisfy expected saturation and magnetic loading levels before the selection of initial parameters. In certain applications, decreasing the machine losses requires a careful choice of material properties.

The number of rotor poles, number of stator slots and winding configurations are a few of the discrete parameters that need to be set before designing for the continuous geometric variables. Once all the parameters are selected, the motor simulation model is created within a numerical software package to predict its performance in a manner similar to solving an inverse problem. If the simulated results are undesirable, the parameters are changed using a set of known rules and equations to improve its output. This procedure is continued until a satisfactory solution is found. While this iterative process has been extensively used to optimize electric machines, there are design challenges that still need to be addressed.

### 3.1.4. Design Challenges

Systematic design of SynRM rotors is not a recent issue: it was first argued in [12] that the SynRM's low efficiency and performance was a direct consequence of its poor geometric rotor construction and an attempt was made to improve it. Throughout the past decades, research papers such as [38] and [50] have proposed analytical and numerical models to design SynRMs through magnetic circuit modelling, FEA and past experiences. By properly designing the stator and rotor lamination structures, the SynRM torque performance can be optimized by forcing the machine flux through the desired iron flux paths.

Previous works [13], [14] and [16] have simplified and reduced the design process by considering the optimal design problem separately. To address the torque ripple issue of SynRMs [51], [52], previous studies of SynRM design methodology [53] kept the stator configuration fixed and a triple-barrier rotor was designed to mutually increase the average torque and decrease the torque ripple. In this work, a similar approach is followed for the multi-objective design optimization which consists of searching for the set of Pareto front solutions.

In addition, the computational times and related problems need to be addressed in finding a set of optimal motor models. For example, a naïve design approach cannot be used to explore the entire stator and rotor search space, as the computational time required to find an optimal solution rises exponentially for higher number of variables. Also, designing electric machines is an NP-hard mixed-integer problem [54]: variables could be either discrete (e.g. winding configurations, number of rotor poles or stator slots, etc.) or continuous (e.g. current excitation, geometric width, and other dimensions). Deciding on the best combination of discrete variables before optimizing the continuous ones is not always possible and may not even converge (also known as an *undecidable solution*) [54]. Another bottleneck in the optimization procedure is using an accurate, yet time-consuming function evaluator such as Finite Element Analysis (FEA). For instance, the six rotor geometric variables in [4] could pose computational issues during the design space sampling before the search for a set of Pareto front solutions.

To address these challenges, §3.2 presents a computationally efficient algorithm for the global design optimization of a SynRM rotor by considering two conflicting objectives: maximizing the average torque and minimizing the torque ripple. A two-step process is described here: 1) find an

optimal region in the search space for a single-barrier rotor, and 2) using this region, restrict the sampling space for an improved multiple-barrier rotor with reduced torque ripple.

Through a single-barrier configuration and a fixed set of stator dimensions, rotors with different slots-per-pole combinations are compared and the procedure's computational complexity is simplified by limiting the design variables to those having the most impact. A simple assumption relies on combining multiple flux paths into one by using magnetic circuit analysis to ensure that a single-barrier solution can represent various multiple-barrier models. Also, the algorithm can reach highly accurate optimal solutions while saving considerable computational time by reducing the number of FEA simulations for the employed control strategy and restricting the feasible search space through an analytical ellipse function. This becomes useful while searching for an optimal multiple-barrier design within this region.

### 3.2. Single-Barrier Rotor Design

To find the set of Pareto optimal designs of a single-barrier SynRM rotor, the algorithm assumes that the stator geometry and windings are fixed. Also the effect of low, medium and high current excitations are explored. The subsections below present the required steps to find an optimal region in the design space.

#### 3.2.1. Geometric Modelling

An overall study of all SynRM rotor parameters may not necessarily lead to a significantly improved design. Only the highest contributing parameters need to be considered in order to reduce the number of combinations.

In a SynRM rotor, there are two main electromagnetic components per rotor pole: the *flux barrier* and the *flux carrier*. A *flux barrier* consists of a non-ferromagnetic material leading to a high magnetic reluctance path, while it is the opposite case for a *flux carrier*. Multiple flux barriers and carriers may be stacked from the rotor's outer diameter to its inner diameter for improving saliency ratios as in Figure 5 [13], [20], but only single barrier designs are considered here. This simplification is justified by assuming that parallel fluxes flowing through multiple smaller flux carriers can be represented by a single flux carrier.

Table 3 from the previous chapter lists the fixed SynRM stator parameters employed for a direct-drive application requiring high average torque. The design parameters are chosen to be the *flux*

carrier  $W_c$  and the flux barrier  $W_b$  widths. Since these two continuous rotor parameters control the magnetic flux passing from the stator teeth to the rotor flux carriers for each rotor pole, it is also worth varying the number of rotor poles  $n_p$ . This discrete parameter later plays an important role in selecting a global optimal rotor model in §4.2.

The two rotor flux widths are modelled by intersecting different circular radii from a fixed center and are chosen to be symmetric about the center of each rotor pole. For the fixed number of stator slots, only three possible rotor pole combinations  $n_p \in \{4,8,10\}$  are chosen to satisfy feasible winding layouts. Higher numbers of rotor poles are ignored. Figure 22 illustrates the SynRM continuous rotor design variables for the 8-pole case. A similar rotor geometric modelling is performed for the other rotor pole combinations using the *MotorSolve* software [43].

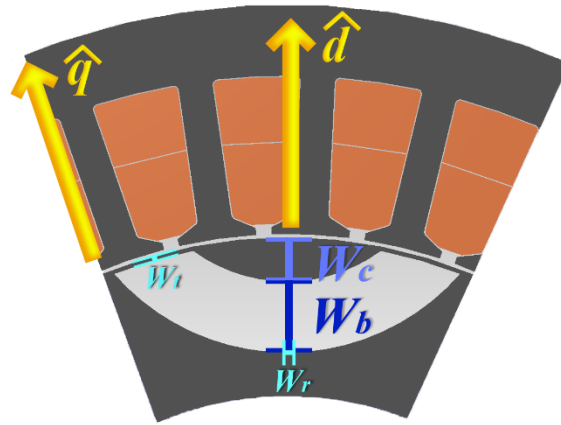


Figure 22. Continuous Rotor Design Variables across a Rotor Pole and its  $dq$ -axes

For each number of rotor poles  $n_p$ , the flux carrier  $W_c$  and barrier  $W_b$  widths range from a lower bound  $W_l$  to an upper bound  $W_u$  using the rotor outer diameter as a reference point. If both widths continuously increase, two adjacent rotor poles will touch and possibly intersect each other. To avoid this problem, a linear sum constraint is imposed for both  $W_c$  and  $W_b$  through the total width limit  $W_{lim}$ . This  $W_{lim}$  value is calculated using the geometric values in Table 3 and the number of rotor poles  $n_p$ . Hence the 3-dimensional design space consists of the convex feasibility triangle  $\mathcal{F}_\Delta$  constrained by (22) and (23) in the continuous  $(W_c, W_b)$  plane for each  $n_p$  combination.

$$W_l \leq (W_c, W_b) \quad (22)$$

$$W_c + W_b \leq W_{lim} \quad (23)$$

Here, the  $W_u$  value is a function of the independent bounds  $W_l$  and  $W_{lim}$  in the single-barrier design space. Each continuous  $(W_c, W_b)$  plane is sampled for 90 different points using a full factorial approach due to the low dimension number (2 for a single-barrier model) [45]. For a full factorial sampling of 2 design variables across 13 levels, there is a total of  $13^2 = 169$  points using (21). However, not all the sampled points are constrained within the convex feasibility triangle  $\mathcal{F}_\Delta$ , so the infeasible samples are removed by using (22) and (23). This leaves 90 design points per rotor pole combination to generate a total of 270 SynRM rotor models for the three rotor pole combinations  $n_p \in \{4, 8, 10\}$ . For each motor model, the flux barrier is filled with air, and the stator and rotor core material is *M-19 29 Ga* steel. Each SynRM model in *MotorSolve* is later exported to the *MagNet* software to take advantage of the Parallel toolbox in the *MATLAB* software for faster objective calculations [55].

### 3.2.2. Data Acquisition

An electromagnetic simulation of a SynRM model can be performed using a sequence of static FEA solutions for rotor optimization problems due to its nonlinear material characteristics. However at high rotor speeds when the eddy current rotor losses become prominent, time-stepping or transient 2D FEA solutions would be needed to include additional objectives: maximization of efficiency and power factor. If the global optimization process simulates SynRMs using a sequence of static FEA solutions for each sampled design space point, it is both computationally expensive and impractical for even modest design space dimensions. For example, [53] used 7 continuous variables in a similar multi-objective optimization for a triple-barrier rotor. They attempted to reduce the computational time by reducing the number of static FEA evaluations and focusing the SynRM operation for a single current magnitude and advance angle operation. As explained in the previous subsection, the number of continuous rotor variables should be limited to those having the most impact in order to find a global optimum design of a single-barrier rotor. Significant computational time is also saved during the data acquisition by reducing the number of FEA simulations during the objective calculations.

Evaluation of the two conflicting objectives, *average torque* and *torque ripple*, for each rotor design requires solving for the steady-state instantaneous torque  $T$  through 2D FEA simulations. Since the stack length is relatively long with respect to the stator outer diameter, the motor's end effects can be ignored and 2D FEA simulations can accurately simulate the performance objectives

[43]. In this current-source simulation, the balanced 3-phase windings are excited using a 3-phase sinusoidal excitation with phase advance using  $\gamma$ . For the employed FOC approach, it is assumed that the SynRM's rotor orientation is known at each time instant of the 2D FEA simulation for generating a stator MMF orthogonal to the rotor's magnetic axis. This follows the *Maximum-Torque-per-Ampere* control strategy in §2.2.2. For a given current magnitude  $I_s$  and advance angle  $\gamma$ , the solution mesh of a single-barrier SynRM rotor is generated using the model's geometric information as illustrated in Figure 23. Next the FEA field solution in the *MagNet* software [43] is computed (refer to §2.3.3), post-processed and filtered to display the smoothed flux density magnitudes in Figure 24.

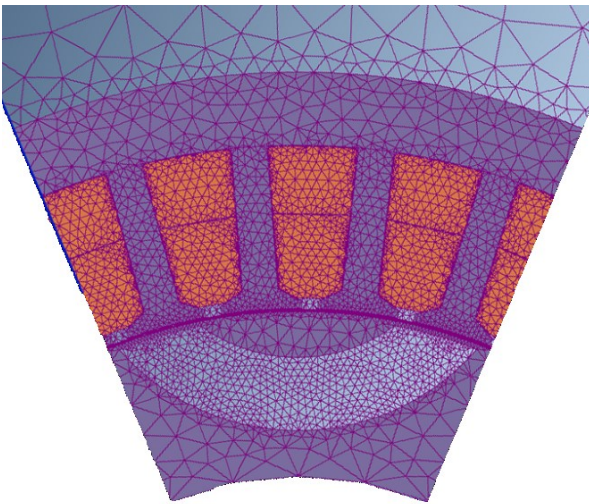


Figure 23. Solution Mesh of an 8-Pole Single-Barrier SynRM Rotor ( $1.0I_{rated}$ ,  $56^\circ$ )

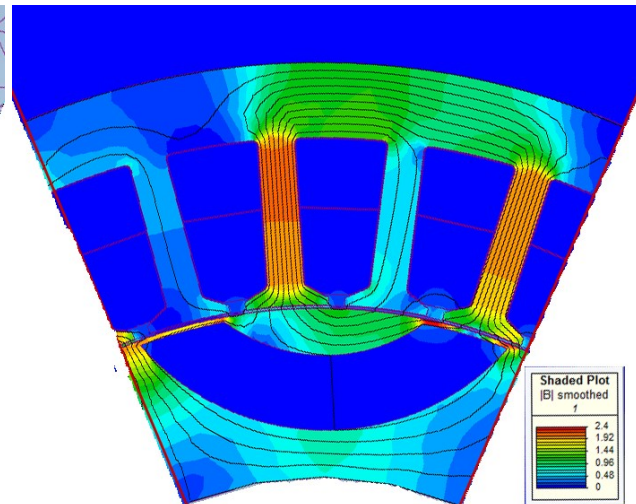


Figure 24. FEA Field Plot of an 8-Pole Single-Barrier SynRM Rotor ( $1.0I_{rated}$ ,  $56^\circ$ )

Both Figure 23 and Figure 24 are generated at one time instant of the 2D time-stepping FEA. In subsequent time steps, the rotor is rotated to a new position to calculate the new field solutions. The current advance angle of  $56^\circ$  was chosen to satisfy the MTPA control strategy at  $1.0I_{rated}$ . In Figure 23, the geometric mesh is observed to be denser around component edges (around the stator teeth and the flux barrier) and surrounding regions where magnetic saturation is expected (inside the air gap and the tangential ribs). Conversely, the virtual air box outside the motor has fewer meshed points because there is less magnetic field variation. The FEA field solution in Figure 24 shows that the stator back-iron, stator teeth and rotor back-iron are under the flux density limits suggested by [49] to ensure that magnetic losses are reduced.

Through the motor's periodicity of 3-phase windings and even number of rotor poles, only  $1/6^{\text{th}}$  of an electrical period with 48 sample points is used to evaluate the two objectives as functions of  $\bar{\mathbf{W}} = [W_c \ W_b]$ . The *average torque*  $T_{avg}$  in (24) is defined as the mathematical average of *instantaneous torque*  $T$  for one period  $N$ , and the *torque ripple*  $T_{rip}$  in (25) is the worst-case peak-to-peak torque difference with respect to  $T_{avg}$ .

$$T_{avg}(\bar{\mathbf{W}}) = \frac{1}{N} \sum_{i=1}^N T_i \quad (24)$$

$$T_{rip}(\bar{\mathbf{W}}) = \frac{|\max(T) - \min(T)|}{T_{avg}(\bar{\mathbf{W}})} \quad (25)$$

An important consideration in using the *MotorSolve* software [43] is the appropriate selection of the *Speed/Accuracy* setting, which is responsible for the mesh refinement level and the polynomial order of the solver method. As this setting number is incremented, the solution accuracy is increased at the cost of investing more computational effort and time. In order to choose a reasonable tradeoff between speed and accuracy, a single motor model is subjected to a sensitivity analysis for the torque ripple objective as shown in Figure 25.

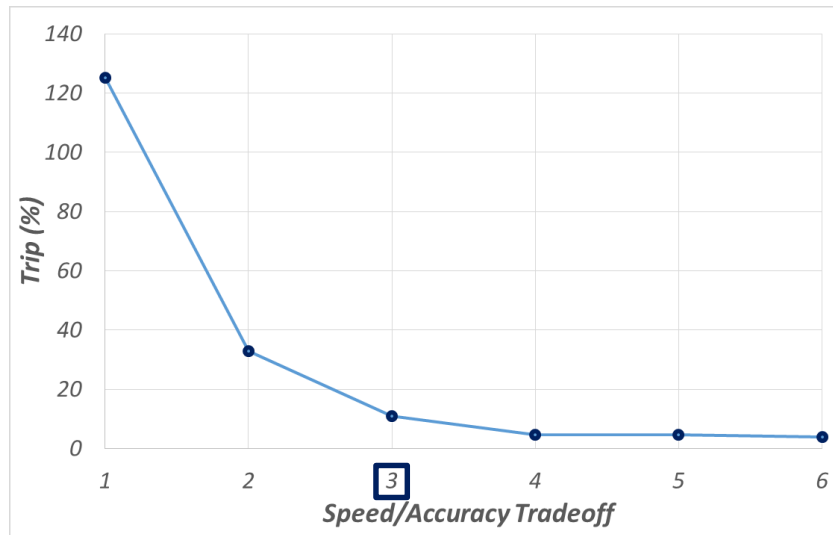


Figure 25. Sensitivity of Torque Ripple to the *Speed/Accuracy* Tradeoff Setting

By changing the *Speed/Accuracy* setting value from 1 to 3, the torque ripple value significantly drops from about 125% to 11%. Beyond a settling value of 4, the torque ripple values stay relatively constant and the computational effort required increases exponentially. It is observed

that the average torque is not as sensitive to the setting numbers due to the mathematical averaging effect of (24). Therefore, a *Speed/Accuracy* setting of 3 is chosen to simulate the instantaneous torque and calculate both objectives for each rotor design.

While motor engineers typically design for overloaded motor conditions [53], different operational points are considered to include the high efficiency regions at low current levels. This approach optimizes the SynRM rotor for different vehicle driving conditions such as efficient urban and power-consuming highway drive cycles. To incorporate this effect, the SynRM stator windings are excited at 50%, 100% and 200% of the rated current. Also the two objectives are calculated using the MTPA control strategy to compare different rotor designs. This strategy maximizes  $T_{avg}$  for a given current level by varying the current advance angle [18], [20]. Since the average torque versus the current advance angle has a single global maximum, at least 3 FEA simulations per rotor model are required to fit a quadratic function  $a\gamma^2 + b\gamma + c = 0$  and find the MTPA average torque  $T_{avg}^{MTPA}$  using  $\gamma^{MTPA}$ . A 3-part MTPA peak finding algorithm pseudocode is presented in Figure 26 and is used to search for the maximum operation point of each rotor design.

```

Initialize  $\gamma^0, \Delta\gamma$ 
Set  $p = \alpha = +1, k = 0$ 
Evaluate  $T^0 = T_{avg}(\gamma^0)$ 
Update  $\Delta T_1 = 0, \Delta T_2 = T^0$ 

While ( $\Delta T_2 / \Delta T_1 > 0 \parallel k \leq 2$ )
    Set  $\gamma^k = \gamma^{k-1} + \alpha p \Delta\gamma$ 
    Evaluate  $T^k = T_{avg}(\gamma^k)$ 
    Update  $\Delta T_1 = \Delta T_2, \Delta T_2 = T^k - T^{k-1}$ 

    IF ( $\Delta T_2 < 0$ )
         $p = -p, \Delta T_2 = -\Delta T_2$ 

    Update  $k = k + 1$ 
EndWhile

Set  $\gamma^{MTPA}$  using  $a\gamma^2 + b\gamma + c = 0$ 
Evaluate ( $T_{avg}^{MTPA}, T_{rip}^{MTPA}$ ) using  $\gamma^{MTPA}$ 
    
```

Figure 26. Pseudocode for the MTPA Peak Finding Algorithm

The first advance angle value  $\gamma^0$  and step size  $\Delta\gamma$  are initialized before setting the peak finding direction  $p$  and evaluating the first average torque value  $T^0$ . To find the single peak of a quadratic function, two torque difference variables  $\Delta T_1$  and  $\Delta T_2$  are defined in the  $+\gamma$  direction. In the  $k^{th}$ -iteration,  $\Delta T_2$  calculates the torque difference  $T^k - T^{k-1}$ , while the  $\Delta T_1$  stores the torque difference value from the previous iteration. Once more than three advance angles are explored, a stopping criterion of  $\Delta T_2/\Delta T_1 \leq 0$  is used to check whether a peak value of average torque is found or not. If the peak is not yet reached, a new advance angle  $\gamma^k$  is set before evaluating the average torque value  $T^k$  in the next iteration. Note that  $\gamma^k$  also relies on a scalar variable  $\alpha$  used to skip over previous explored points. For instance, if the new  $T^k$  value is lower than the previous  $T^{k-1}$ , both  $p$  and  $\Delta T_2$  are reversed, and the  $\alpha$  scalar is modified to avoid searching the  $\gamma^{k-1}$  angle again. Once the MTPA peak is found, the two corresponding objective values  $(T_{avg}^{MTPA}, T_{rip}^{MTPA})$  are calculated using the quadratically-fit  $\gamma^{MTPA}$ .

An example is illustrated below in Figure 27 to explain the operation of this algorithm. Starting from an initial guess  $\gamma^0$  through to  $\gamma^1$  and  $\gamma^2$ , the respective average torque values  $T^0$ ,  $T^1$  and  $T^2$  are all increasing corresponding to positive values of  $\Delta T_1$  and  $\Delta T_2$ . The stopping criterion of  $\Delta T_2/\Delta T_1 \leq 0$  is not yet satisfied, so the while loop continues for a fourth iteration. However, the present  $T^3$  value is lower than  $T^2$  which enforces an opposite polarity between the two torque difference variables  $\Delta T_1$  and  $\Delta T_2$ . Now the loop can be safely broken to compute the MTPA values.

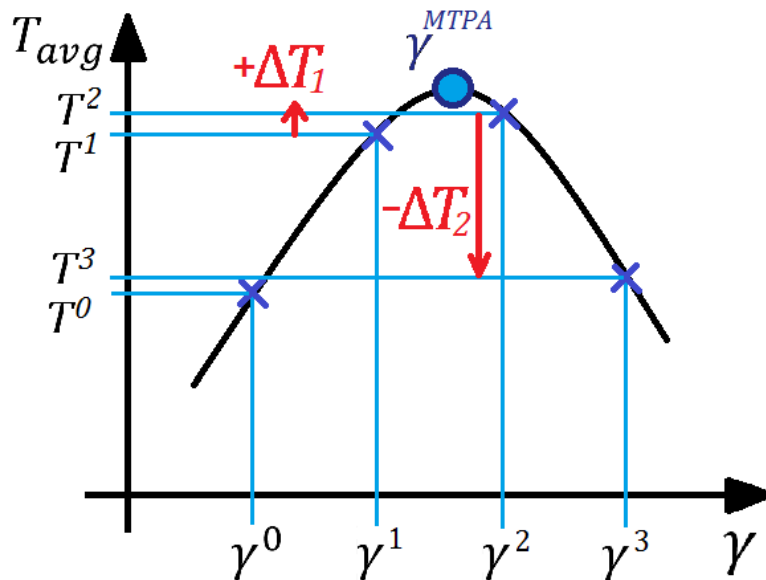


Figure 27. Example of the MTPA Peak Finding Algorithm (4 Iterations)

### 3.2.3. Supplementary Analysis

In addition to the methodologies presented for data acquisition, it is necessary to demonstrate the expected results by illustrative means. For one model design, both Figure 28 and Figure 29 display flux density plots using FEA solutions of an  $8$ -pole SynRM. The difference between them is that Figure 28 is only excited by a  $q$ -axis current where the advance angle is set to  $0^\circ$ . This encourages the flux lines to propagate through the minimum rotor reluctance paths from the stator teeth. On the other hand, Figure 29 is excited by a  $d$ -axis current where the advance angle is  $90^\circ$ .

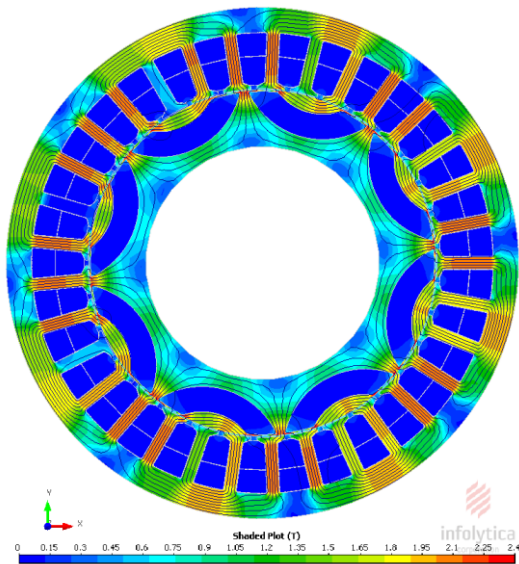


Figure 28. FEA Field Plot of an  $8$ -Pole Single-Barrier SynRM ( $1.0I_{rated}$ ,  $0^\circ$ ,  $I_d=0$ )

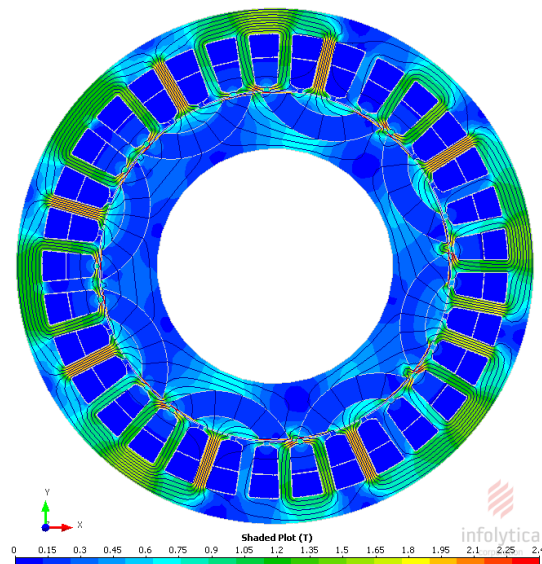


Figure 29. FEA Field Plot of an  $8$ -Pole Single-Barrier SynRM ( $1.0I_{rated}$ ,  $90^\circ$ ,  $I_q=0$ )

Since the rotor's magnetic axis is not correctly aligned with the stator MMF in Figure 29, the flux lines can only pass through the maximum reluctance paths of the flux barriers. This  $d$ -axis current excitation also introduces a lower magnetic loading on the stator teeth and back-iron compared to the first case. From the two figures, it is observed that adding more  $d$ -axis current excitation demagnetizes the rotor which is the effective method of introducing Flux-Weakening control.

Once the MTPA peak finding algorithm is used for a SynRM design, the instantaneous torque values for one or more electrical periods are obtained as shown in Figure 30. In this example, 78 time samples are used to calculate the instantaneous torques  $T_i$  for 3 different advance angles where one electrical period consists of 48 time samples. It is observed that the  $\gamma^{MTPA}$  value is  $56^\circ$ , because the average torques are lower for both  $50^\circ$  (506 Nm) and  $60^\circ$  (512 Nm) compared to the  $56^\circ$  (518 Nm) case. The average torque versus the advance angle behaviors are similar to that in Figure 27.

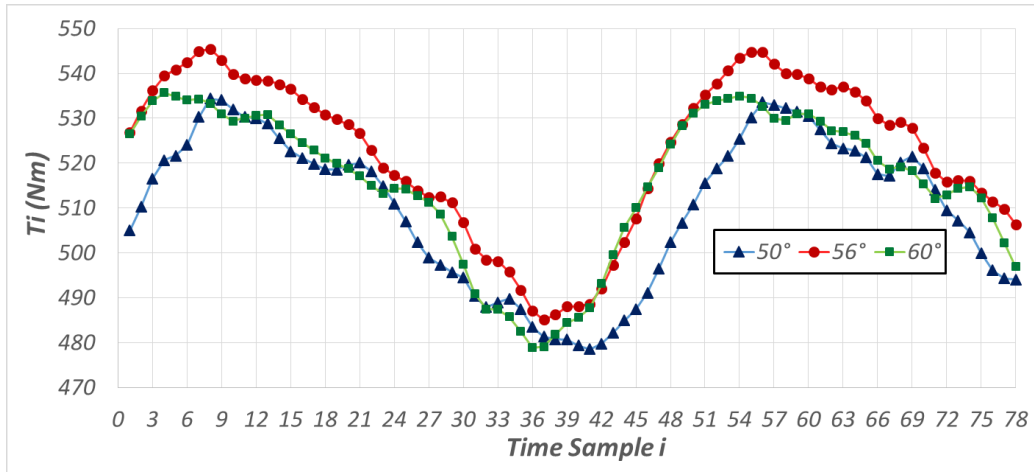


Figure 30. Instantaneous Torque Plots for 3 Advance Angles (8 poles, 1.0I<sub>rated</sub>)

Next, the simplified assumption to exclude the structural radial  $W_r$  and tangential  $W_t$  ribs from the rotor geometric parameters is validated. From an ideal electromagnetic perspective, both ribs should tend to zero in order to diminish the leakage flux passing between flux carriers and to reduce the  $d$ -axis rotor inductance. Since this is not possible in a realistic machine, both widths are minimized in order to structurally withstand high rotor speeds. For an 8-pole single-barrier SynRM design, the sensitivity of the average torque to the radial and tangential ribs is analyzed in Figure 31 and Figure 32 respectively. The displayed points of the radial and tangential ribs individually fit well to linear and quadratic functions. As expected, the average torque decreases when both rib widths increase. This simple relationship does not provide a local maximum, so both ribs are assumed to be constant for all sampled designs ( $W_r = 0.0$  mm,  $W_t = 1.0$  mm).

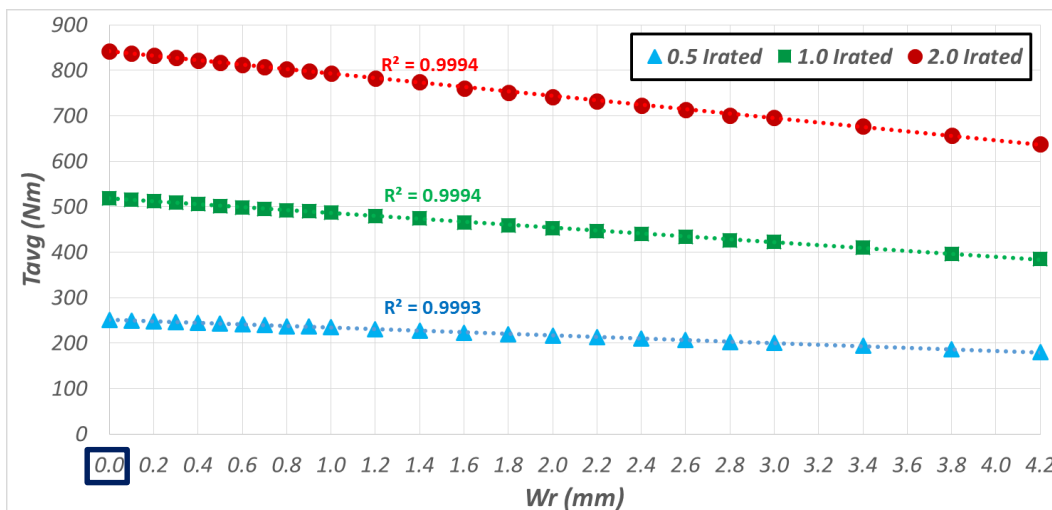


Figure 31. Sensitivity of Average Torque to the Radial Rib Width for Different Currents

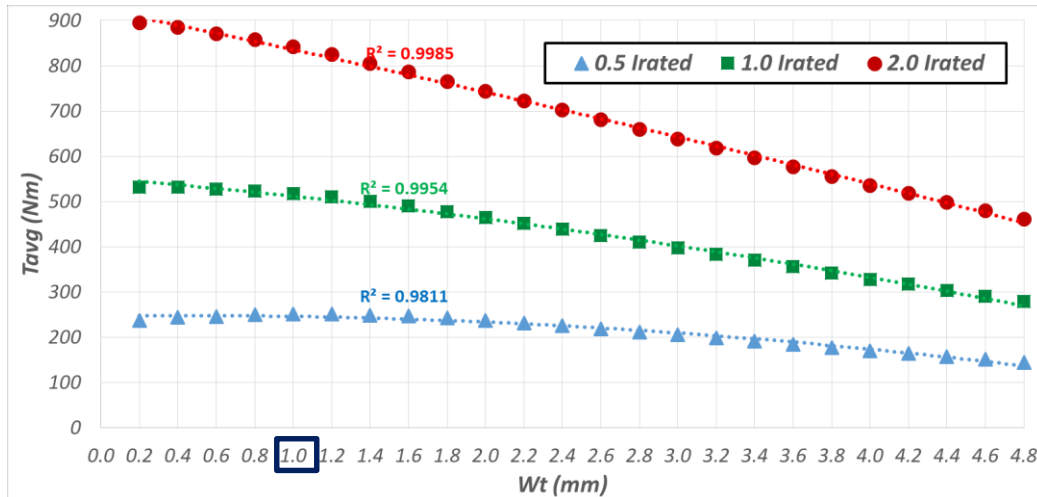


Figure 32. Sensitivity of Average Torque to the Tangential Rib Width for Different Currents

### 3.2.4. Surrogate Modelling

Before the discussion of surrogate modelling methods, a brief theory of artificial neural networks is reviewed below. An elementary multiple-input neuron is displayed in Figure 33 that connects the inputs  $p$  through the respective scalar weights  $w$  and bias  $b$  to a summing function  $\Sigma$ . The output  $n$  of the summing function is then passed onto a function  $f$  to the neuron output  $a$ . As represented in Figure 34, a single neuron  $\Sigma$  is used inside the hidden layer of an artificial neural network. The outputs of all the hidden layer neurons are summed and sent through a sigmoid function  $S$  which acts as a smooth threshold function to give a single neural network output.

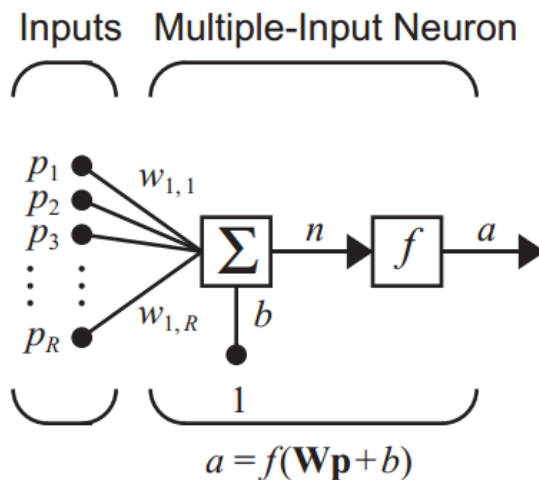


Figure 33. A Multiple-Input Neuron [56]

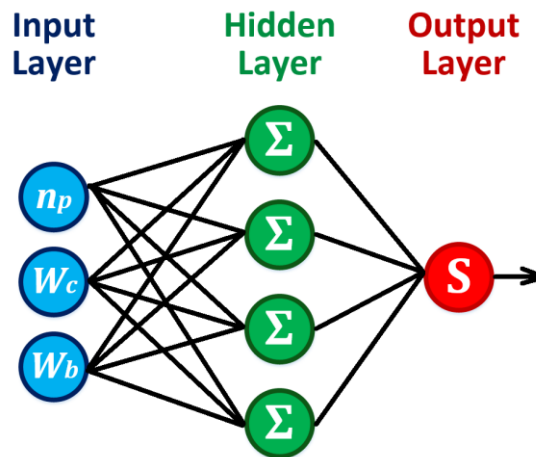


Figure 34. 3-Input 1-Output Artificial Neural Network with a Single Hidden Layer

In artificial intelligence, both the input and output targets are known a priori whereas the neural network weights and biases are unknown. In finding the right network weights and biases, a good

training function is used with two main goals: to match the network output with given targets using known inputs and to interpolate the network output for untrained inputs. The objective lies in evaluating the neural network for unknown inputs after the training process.

An artificial neural network acts as an interpolating function for regression analysis. It must not overfit the given data and ensure that the network outputs are accurately calculated for unknown input values. A common method to evaluate how well the training function of the neural network has performed is to divide the initial dataset into three sets: *training*, *validation* and *testing*. As explained in [56], the *training set* updates the network weights and biases upon computing the gradient. The *validation set* is used to monitor and improve the neural network training process through a corrective feedback. If the neural network overfits the training data due to the number of hidden layer neurons, the validation error rises and helps in adjusting the correct network weights and biases. The *testing set* checks how well the trained network can handle unknown inputs and is used to compare different trained networks without affecting the network training process. A quantitative method to measure the closeness of the neural network outputs with given targets is through the Pearson correlation coefficient  $R^2$  which measures the linear correlation between two variables. During a neural network training, it is desired to maximize this coefficient for all three sets, but with a greater emphasis on the testing set.

Upon data acquisition of the sampled points, the full dataset of the design space ( $n_p, W_c, W_b$ ) and objective space ( $T_{avg}, T_{rip}$ ) is used to train a surrogate model within the feasibility triangle  $\mathcal{F}_\Delta$ . For the limited number of sampled points, a suitable objective training function is needed to handle the tradeoff between data over-fitting and interpolation generalization. For these requirements, the *Bayesian Regularization Backpropagation Neural Network* (BRNN) with a single hidden layer for three inputs and a single output is selected for each objective as in Figure 34. However for each  $n_p$  combination and objective, a separate neural network is trained for its two ( $W_c, W_b$ ) inputs.

Through the Bayesian approach and the Levenberg-Marquardt algorithm proposed in [56], [57] and [58], this training function predetermines the optimal regularization parameters to automatically reduce the mean-squared error and sum-squared weights. It can improve the neural network generalization by using an early stopping criterion and regularization [56]. A Bayesian framework is assumed where all the network weights are random variables and are chosen to maximize the conditional probability of the weights given the data using Bayes' rule [56].

---

Hence, the BRNN training algorithm pseudocode in Figure 35 is used to individually train the two objective networks (*average torque* and *torque ripple*) for each number of hidden layer neurons  $nNeurons$ , current level  $I_s$  and rotor pole combination  $n_p$ . The training, validation and testing sets are randomly divided into 60%, 25% and 15% of the initial dataset. The convergence conditions use the  $R^2$  coefficient between the objective targets and the outputs of the trained neural network. If the  $R^2$  coefficients are less than  $\bar{R}_{thresh}^2$ , the recently-trained BRNN objective is saved before incrementing a counter variable  $iter$ . However if the  $R^2$  coefficient of the training, validation and testing sets are greater than their threshold values, the trained BRNN network is returned and the  $iter$  for-loop is broken. Once the maximum counter value  $MAX\_ITER$  is reached, the trained BRNN objective with the best  $R_{test}^2$  is chosen. This iterative process is repeated for different number of hidden layer neurons  $nNeurons$  using *MATLAB* scripting.

```

For  $nNeurons = MIN\_NEURONS$  to  $MAX\_NEURONS$ 

  For  $iter = 0$  to  $MAX\_ITER$ 
    Train BRNNObj for each  $(n_p, I_s)$ 

    IF  $(R_{train}^2, R_{val}^2, R_{test}^2) \geq \bar{R}_{thresh}^2$ 
      Return BRNNObj and Break
    ELSE
      Save BRNNObj and  $iter++$ 
    EndFor

    IF  $max(R_{test}^2) \geq R_{accept}^2$ 
      Return BRNNObj with  $nNeurons$ 

  EndFor
  
```

Figure 35. BRNN Training Algorithm Pseudocode

A regression validation is performed for the trained objectives by plotting and observing the *Response Surface* (RS) maps in the per-unit  $(W_c, W_b)$  design space plane. Both continuous variables are scaled with respect to the  $W_{lim}$  base quantity in each of their individual per-unit axes. For example, the RS maps of the average torque and torque ripple objectives for  $2.0I_{rated}$  and 8 poles are displayed in Figure 36 and Figure 37 respectively. Similar RS maps are observed for different current levels and numbers of rotor poles. The full factorial sampled points are displayed using dark crosses. Although the neural network is trained to output for any given input, the objective values are only plotted within the feasibility triangle  $\mathcal{F}_\Delta$ .

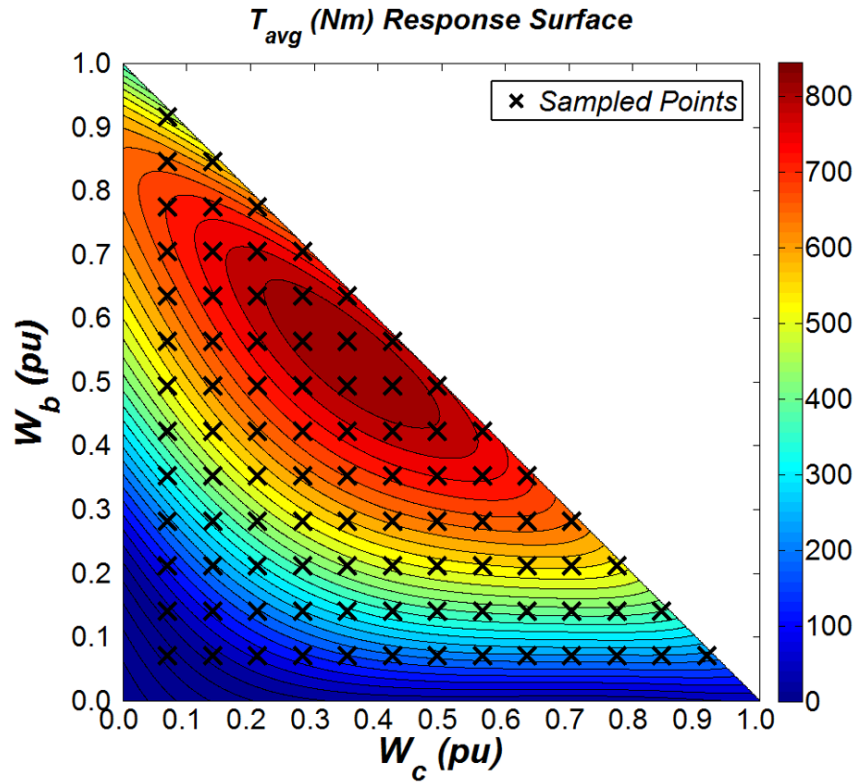


Figure 36. Single-Barrier: Average Torque RS Map for (8 poles,  $2.0I_{rated}$ )

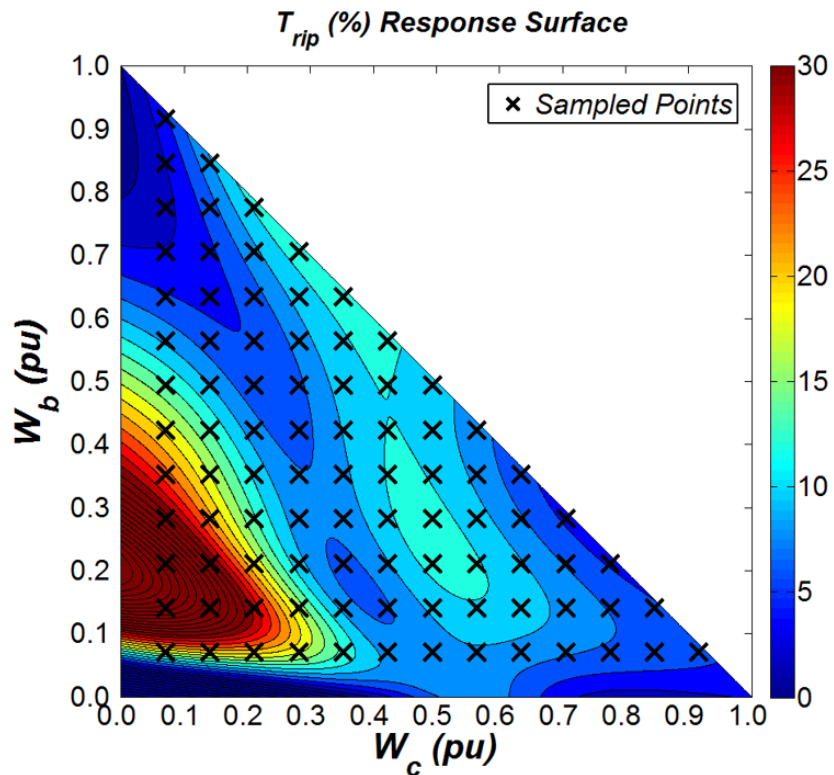


Figure 37. Single-Barrier: Torque Ripple RS Map for (8 poles,  $2.0I_{rated}$ )

For training the  $T_{avg}$  objective, only 5 neurons are needed for the BRNN training pseudocode to converge because its RS is smooth and easy to characterize. Around the single peak, the constant- $T_{avg}$  contours in the  $(W_c, W_b)$  plane follow elliptical shapes with a fixed center. However for training  $T_{rip}$ , 40 neurons provides satisfactory results to model its multimodal characteristic with peaks and valleys. This behavior is described by comparing the smaller testing  $R^2$  values of torque ripple with that of average torque from Table 5 for all three currents.

**Table 5. Training, Validation and Testing  $R^2$  Coefficients for Three Currents of the Trained BRNN Functions for the Average Torque and Torque Ripple Objectives**

$n_p$	Obj.	$0.5I_{rated}$			$1.0I_{rated}$			$2.0I_{rated}$		
		$R^2_{train}$	$R^2_{val}$	$R^2_{test}$	$R^2_{train}$	$R^2_{val}$	$R^2_{test}$	$R^2_{train}$	$R^2_{val}$	$R^2_{test}$
4 poles	$T_{avg}$	1.0000	0.9999	0.9992	1.0000	1.0000	0.9999	1.0000	1.0000	0.9998
	$T_{rip}$	0.9712	0.9877	0.9623	0.9587	0.9729	0.9634	0.9629	0.9503	0.9571
8 poles	$T_{avg}$	0.9998	0.9993	0.9998	1.0000	0.9999	0.9988	1.0000	0.9998	0.9996
	$T_{rip}$	0.9953	0.9776	0.9952	0.9908	0.9629	0.9795	0.9752	0.9742	0.9703
10 poles	$T_{avg}$	1.0000	1.0000	1.0000	1.0000	0.9999	0.9999	1.0000	0.9997	0.9994
	$T_{rip}$	0.9983	0.9584	0.9876	0.9980	0.9854	0.9904	0.9970	0.9823	0.9798

Using the BRNN training algorithm in Figure 35 for the torque ripple objective, the  $R^2_{test}$  values are reported in Figure 38. For each  $nNeurons$ , the  $T_{rip}$  objective is trained 30 independent times to measure the spread of  $R^2_{test}$  values. This boxplot suggests that the median  $R^2_{test}$  values converge to about 0.90 for  $nNeurons$  higher than 16. However if the 3<sup>rd</sup> and 4<sup>th</sup>-quartile ranges are desired to be maximized, the 40 neurons case returns as the best choice. For the  $T_{avg}$  objective, the observed boxplot does not include variability in  $R^2_{test}$  because the neural network is easily trained.

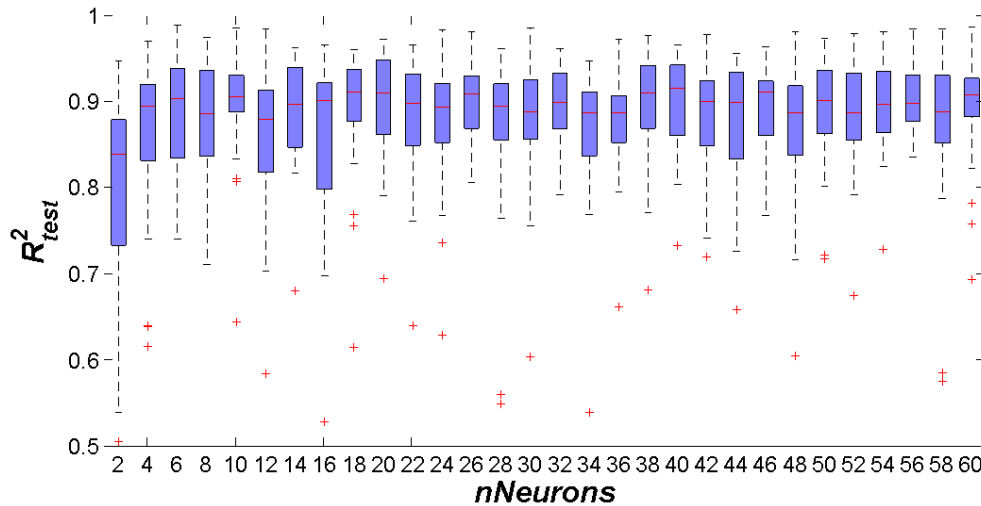


**Figure 38. Boxplot of  $R^2_{test}$  and Number of Neurons for 30 Repetitions ( $T_{rip}$ , 8 poles,  $2.0I_{rated}$ )**

### 3.2.5. Multi-Objective Optimization

In most engineering applications, marginal improvements to current designs are performed using local optimization methods. If a global optimal is suggested instead, there are additional costs associated with using a new manufacturing process which might not be an attractive short-term solution. For the SynRM rotor, however, a global optimization is necessary to understand the geometrical search space and to possibly find optimality conditions that can simplify future rotor modelling processes. To find the set of global optimal solutions of the single-barrier SynRM rotor with respect to the average torque and torque ripple objectives, an optimization procedure must be selected. It is worth mentioning that no optimization algorithm can guarantee convergence to a global optimal in finite time, unless the response surface of the search space is known a priori. For example, the average torque and torque ripple RS maps in Figure 36 and Figure 37 have a single global maximum and two global minima respectively within their feasibility triangle  $F_{\Delta}$  which ensure convergence of an appropriate optimization method.

*Deterministic optimization* methods typically rely on searching for optimal solutions using the mathematical gradient of the objective function. While these methods can quickly find an optimal solution, they are unable to escape a local optimum and may miss on searching for better solutions. On the other hand, stochastic methods take a longer time to converge to a global solution for a known RS map, because they continue to search the design space even after a local solution is found [59]. They can adapt to different computational problems and perform well for different cases [60]. Also a valuable trait of stochastic methods is their ability to handle non-differentiable objective functions which often arises in electric machine design. They perform a “random walk” through the design space and evaluate the objective value or fitness function at every explored point to understand the space’s behavior.

Under *stochastic optimization* methods, the genetic algorithm relies on mimicking the biological evolution process. By considering a search space consisting of chromosomes (DNA strings), a *Genetic Algorithm* (GA) method naturally selects the best genetic sequence of genes by continuously producing a new population of individuals [60]. In generating a new population at every iteration, a GA applies three main operators to the current individuals: *mutation*, *selection* and *crossover*. During a *crossover* operation, different individuals exchange their genes to potentially search for new combinations of solutions. A *mutation* operator randomly changes one or more genes in a chromosome in the hope of finding a new genetic sequence and escaping a local

minimum. Upon producing individuals to generate new chromosomes, the *selection* operator then chooses the best individuals for the next generation through their fitness values. Once an initial population of individuals is selected, the next ones are generated by a similar process until the rate of improvement of the fitness value has settled or the maximum number of generations has been reached. This iterative process follows the natural selection process by eliminating weak solutions and maintaining good ones across different populations of individuals. The set of Pareto optimal solutions are then reported to select a desired point satisfying the engineering constraints.

In order to consider two objectives and handle the discrete  $n_p$  variable, a Pareto optimization using the *Multi-Objective Genetic Algorithm* (MOGA) is used to find a final set of optimal solutions. Computational time becomes critical when the MOGA optimization uses a significant number of function evaluations to arrive at a set of optimal rotor designs [59]. By using BRNN surrogate models instead of direct FEA simulations, the computation overhead in function evaluations is significantly decreased [61], [62].

For this SynRM example, the formulated MOGA problem in (26) and (27) uses a population size of 100 individuals and a maximum of 600 generations: the average torque  $T_{avg}(\bar{\mathbf{W}})$  is maximized while the torque ripple  $T_{rip}(\bar{\mathbf{W}})$  is minimized within the feasible design space. The implementation of the multi-objective optimization is simplified by multiplying all the average torque values with  $-1$  and minimizing both objectives in (26). The first generation is evenly divided among the 4, 8 and 10-pole datasets, and the MOGA optimization is run 10 independent times for each current.

$$\min. \left( -T_{avg}(\bar{\mathbf{W}}), T_{rip}(\bar{\mathbf{W}}) \right) \quad (26)$$

$$\text{s. t. } \begin{cases} \bar{\mathbf{W}} \in \mathcal{F}_\Delta \\ n_p \in \{4, 8, 10\} \end{cases} \quad (27)$$

Upon running the optimization for the three current levels, the set of all optimal solutions  $\bar{\mathbf{W}} \in \mathcal{F}_{\text{OPT}}$  is obtained and used to generate the three Pareto fronts in the objective space of Figure 39. The brightness gradient of the solution markers represents the relative position of individual solutions on their respective Pareto fronts.

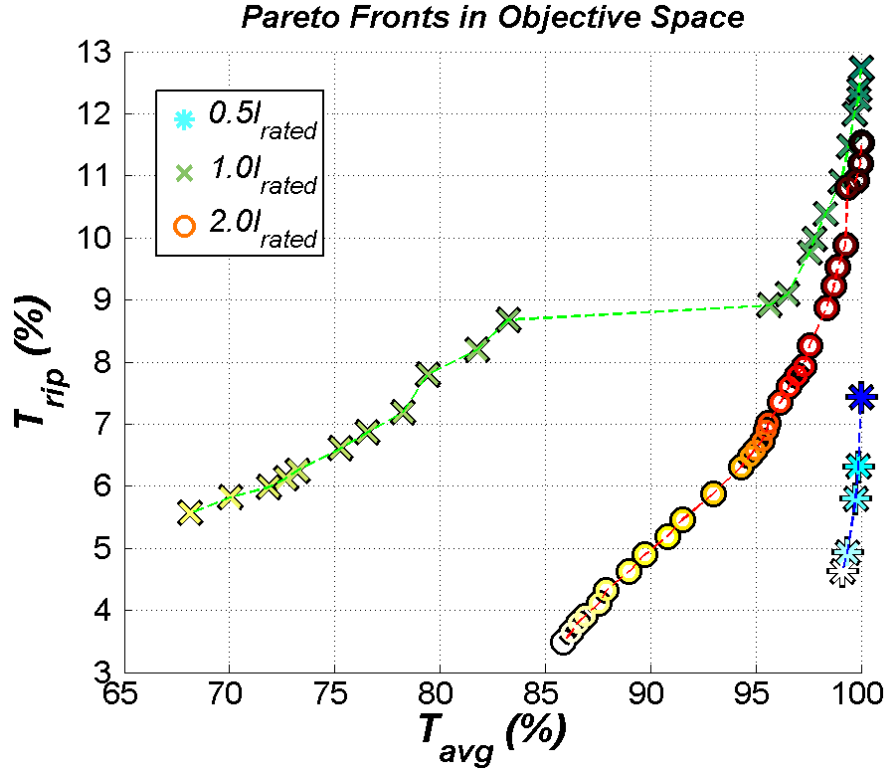


Figure 39. Pareto Fronts for Three Currents Levels in the Objective Plane

Note that the  $T_{avg}$ -axis is scaled using (28) for each current dataset such that the 50%, 100% and 200% Pareto fronts converge to their respective maxima  $T_{avg}^{MAX}$  (271 Nm, 526 Nm, 842 Nm).

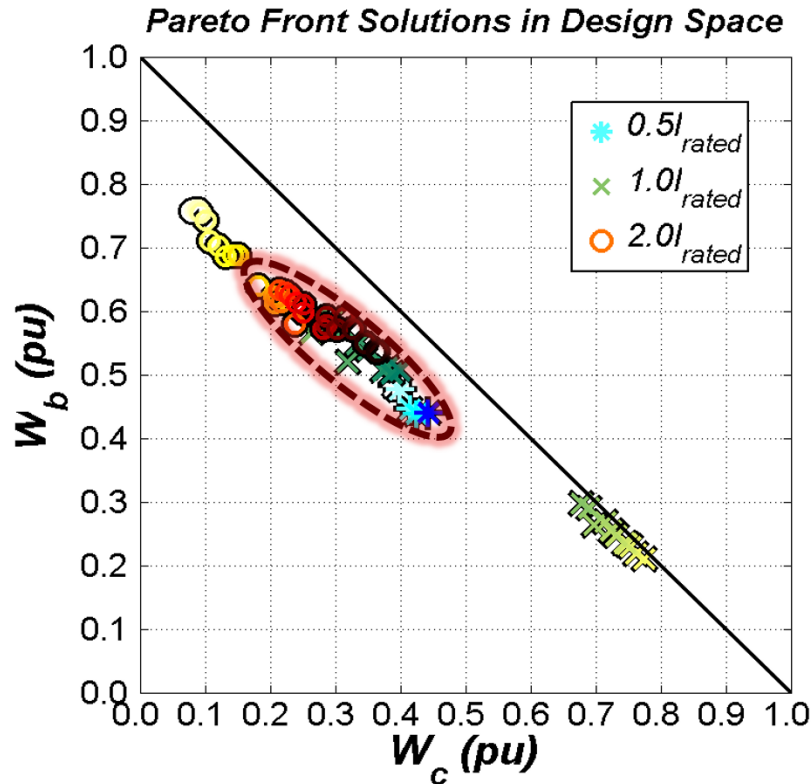
$$T_{avg}^{MAX}(I_s) = \max(T_{avg}(I_s)) \quad (28)$$

Only the  $8$ -pole designs survived in the end, because the stator is fixed and the  $8$ -pole configuration has a better *slots-per-pole* number than their  $4$  and  $10$ -pole counterparts. If the number of stator slots  $n_s$  is changed, the Pareto fronts of the MOGA may no longer consist of  $8$ -pole solutions and could even comprise of solutions across multiple  $n_p$  datasets. As suggested in [51], an asymmetric flux barrier arrangement with respect to the stator slots results in lower ripple torque values which occurs for the  $8$ -pole configuration (*slots-per-pole* =  $33/8 = 4.125$ ). Upon observing the  $T_{rip}$  results for all three current levels, the mean  $\mu_{rip}$  and standard deviation  $\sigma_{rip}$  in the  $8$ -pole dataset are significantly lower than in the  $4$  and  $10$ -pole cases shown in Table 6, which explains the lone existence of the  $8$ -pole Pareto fronts. For the following analysis, only the  $8$ -pole rotor is considered due to the superiority of its two objective values to other rotor pole combinations.

**Table 6. Statistics ( $\mu_{rip}$ ,  $\sigma_{rip}$ ) of All Single-Barrier Designs for the  $T_{rip}$  Objective**

$n_p$	$n_s/n_p$	$0.5I_{rated}$	$1.0I_{rated}$	$2.0I_{rated}$
4 poles	8.250	26.11	22.73	23.27
		11.28	9.44	16.34
8 poles	4.125	16.53	13.77	12.10
		8.39	5.25	8.23
10 poles	3.300	30.54	34.41	33.00
		10.76	9.95	8.37

Figure 40 displays the  $\mathcal{F}_{OPT}$  solutions of the three Pareto fronts of Figure 39 in the continuous design space of the 8-pole rotor. Although both objectives are optimized, more emphasis is placed on the high- $T_{avg}$  solutions of the three Pareto fronts for the considered direct-drive application. This eliminates the left-hand solutions in the objective space of Figure 39 and clusters the dark-shaded Pareto optimal solutions ( $T_{avg} > 90\%$ ) within an ellipse constraint in the design space of Figure 40. Representing the high- $T_{avg}$  solutions through this ellipse constraint relies on the unimodal characteristic of the RS map in Figure 36: the constant- $T_{avg}$  contour lines follow an elliptical behavior with respect to the  $(W_c, W_b)$  plane.


**Figure 40. Pareto Front Solutions for Three Currents Levels in the Design Plane**

Hence, the MOGA formulation may be modified to include an additional constraint  $T_{avg} > T_{avg}^{REQ}$ . An alternative approach would be to cluster the high average torque solutions  $\bar{W} \in \mathcal{F}_{HT}$  in the design space using an analytical function. For the 50%, 100% and 200% rated current solution sets in Figure 40, the final design points for the  $T_{avg} > 90\%$  constraint are grouped near each other in the design space in a similar manner to the constant- $T_{avg}$  elliptical contours in Figure 36. These solution points  $\mathcal{F}_{HT}$  in the design space can be analytically clustered using the *Minimum Volume Ellipsoid covering a finite set* formulation for a convex optimization problem in [59].

To analytically capture the high- $T_{avg}$  Pareto solutions, the convex optimization given in (29) and (30) is formulated. For a given set of optimal design points, the volume (or area) of the ellipse  $\epsilon$  is minimized such that the interior of  $\epsilon$  contains all the given design points [59]. In other words, an ellipse  $\epsilon$  is desired which encloses all the high average torque solution points  $\bar{W} \in \mathcal{F}_{HT}$  within itself. The unknown parameters of (29) and (30) are matrix  $\bar{A}$  and vector  $\bar{b}$  governing the eccentricity and center of ellipse  $\epsilon$ . Upon solving this problem using CVX, which is a convex optimization modelling tool based in *MATLAB* [63], [64], the illustrated ellipse constraint  $\epsilon$  in Figure 40 is observed to be similar to the constant- $T_{avg}$  contour lines of Figure 36. Hence, the location of the optimal solutions  $\mathcal{F}_{HT}$  in the single-barrier space can help identify a restricted region in the multiple-barrier space and reduce the number of samples needed. To validate the computational effectiveness of ellipse  $\epsilon$ , a double-barrier rotor example is presented in §3.3.

$$\max. \left( \sqrt{\det \bar{A}} \right) \quad (29)$$

$$s. t. \left\| \bar{A} \bar{W} + \bar{b} \right\|_2 \leq 1 \quad (30)$$

### 3.3. Result Verification and Discussion

Although the surrogate modelling process in §3.2.4 ensures that the trained function evaluator is robust enough for different test cases, it is crucial to validate the accuracy of the final solutions against FEA simulations as demonstrated below. This verification of the Pareto fronts is performed in §3.3.1 below. In addition, the usefulness of the ellipse constraint is demonstrated in §3.3.2 by comparing the solution quality of two sampling methods in the double-barrier design space: one relies on restricting the sampling region in the 4 dimensions of the design space, while the other approach directly samples the entire space.

### 3.3.1. Pareto Front Validation

Once the Pareto solutions are obtained, they are validated using 2D FEA simulations similar to §3.2.2. For each solution at every current level, the relative error percentage  $e_r$  between the MOGA and FEA objective values is evaluated using (31).

$$e_r = \frac{|f_{FEA} - f_{MOGA}|}{|f_{MOGA}|} \quad (31)$$

Using the calculated  $e_r$  for all the Pareto front solutions and each objective, a statistical analysis is performed for each current level with results presented in Table 7:  $\mu(e_r)$  is the mean error,  $\sigma(e_r)$  is the standard deviation error and  $\max(e_r)$  is the maximum error. The mean and standard deviation values of the  $T_{avg}$  errors are under  $(0.2, 0.1)$ . For the  $T_{rip}$  errors, these are below  $(5.4, 4.0)$ . It should be noted that compared to  $T_{avg}$ , the higher  $T_{rip}$  errors are predictable through the differences in the  $R_{test}^2$  values between the two trained BRNN objectives in Table 5. Nevertheless, the relative error percentages for the torque ripple are acceptable in finding a set of global optimal solutions. During the local optimization of a chosen global solution, the magnitudes of the relative error percentages become more prominent.

**Table 7. Relative Error Percentage Statistics for Validated FEA Solutions**

$I_s/I_{rated}$	Average Torque $T_{avg}$			Torque Ripple $T_{rip}$		
	$\mu(e_r)$	$\sigma(e_r)$	$\max(e_r)$	$\mu(e_r)$	$\sigma(e_r)$	$\max(e_r)$
<b>0.5</b>	0.16	0.07	0.24	5.36	3.92	8.74
<b>1.0</b>	0.14	0.07	0.26	3.39	2.65	8.02
<b>2.0</b>	0.15	0.10	0.33	2.35	1.48	5.37

Table 8 compares an optimal solution within the ellipse constraint of Figure 40 with two solutions chosen outside the suggested ellipse constraint for the  $2.0I_{rated}$  Pareto front. As expected, the undesirable solutions outside the ellipse constraint have lower average torque and higher torque ripple (worse objective values) with respect to the optimal reference solution.

**Table 8. Comparison between Optimal and Non-Optimal Solutions for  $2.0I_{rated}$**

$n_p$	$W_c$ [pu]	$W_b$ [pu]	$T_{avg}$ [Nm]	$T_{rip}$ [%]	Inside $\epsilon$ ?
<b>8 poles</b>	0.29	0.57	825.01 ( <i>refer.</i> )	8.52 ( <i>refer.</i> )	Yes
	0.50	0.21	541.50 (-34.4%)	13.23 (+55.3%)	No
	0.14	0.86	581.46 (-29.5%)	9.65 (+13.3%)	No

### 3.3.2. Double-Barrier Validation

Compared to the two continuous dimensions ( $W_c, W_b$ ) in the single-barrier design space, a double-barrier rotor requires four dimensions ( $W_c^1, W_b^1, W_c^2, W_b^2$ ) to model a SynRM rotor similar to §3.2.1. The flux carriers and barriers are stacked one after another starting from the rotor’s outer diameter toward the motor’s shaft. However, this increase in the total number of design variables requires a considerable number of samples to generate a reasonably accurate surrogate model for the design optimization procedure of both torque objectives.

Therefore, the underlying hypothesis is that the ellipse constraint  $\epsilon$  from §3.2.5 can be used as an initial guess of the optimal region in the double-barrier design space. A linear summation of the rotor continuous variables is assumed to simplify the mapping between the single and double-barrier spaces through  $W_{c,b} = W_{c,b}^1 + W_{c,b}^2$ . To numerically validate this hypothesis, two sampling methods are compared: method *A* only considers a restricted region of the double-barrier space using  $\epsilon$ , whereas method *B* directly samples the entire space.

To compare both methods in a fair manner, the total number of samples between the two is maintained. Methods *A* and *B* are sampled using a full factorial approach to avoid randomness or bias [45] within  $\mathcal{F}_\Delta$  across 16 and 10 levels respectively. All these design points are evaluated using 2D FEA simulations at  $2.0I_{rated}$  to account for saturation effects.

Figure 41 indicates that method *A* captures the high- $T_{avg}$  solutions in the double-barrier space. Method *A*’s mean and standard deviations of  $T_{avg}$  (792, 56) is clearly superior to *B*’s values (673, 145). Also the  $T_{rip}$  values are not compromised, since the mean and standard deviation of methods *A* (8.0, 2.0) and *B* (8.5, 3.0) are nearly the same. Hence, the torque ripple is further reduced with respect to its single-barrier counterpart (12.1, 8.2) using a restricted sampling approach.

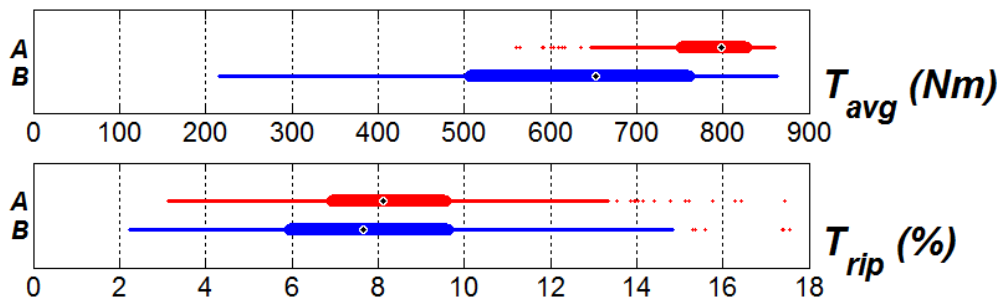


Figure 41. Objective Boxplots for Methods *A* and *B* in the Double-Barrier Space

### 3.4. Conclusion

This chapter predominantly deals with the global design optimization of Synchronous Reluctance Machine rotors. The introduction presents the required theoretical fundamentals, including sampling plans, Pareto fronts and initial sizing, which are referred in the single-barrier rotor design.

Under §3.2, single-barrier models are considered to reduce the algorithm's computational complexity and provide a relative comparison for rotors with different slots-per-pole combinations. Upon sampling the search space of discrete ( $n_p$ ) and continuous ( $W_c, W_b$ ) variables using 270 SynRM rotor models (90 models per  $n_p$  combination), two objective values per sampled design ( $T_{avg}, T_{rip}$ ) are computed using 2D Finite Element Analysis simulations as demonstrated in §3.2.2. Non-linear regression or surrogate models are trained for the two objectives through a *Bayesian Regularization Backpropagation Neural Network* shown in §3.2.4. Due to the tradeoffs between over-fitting and trend generalization of the input dataset, the high-frequency components in the torque ripple's dataset led to higher errors than in the average torque. Subsequently in §3.2.5, a *Multi-Objective Genetic Algorithm* is used to find the FEA-validated Pareto front solutions. An analytical ellipse constraint is then suggested to encapsulate optimal solutions in the design space. Compared to a direct sampling approach in §3.3.2, this restriction helps capture an optimal region within the double-barrier space for further torque ripple reduction.

Therefore, the generalizable algorithm systematically provides the set of optimal single-barrier SynRM designs within the analytical ellipse constraint. Relative accuracies of the Pareto optimal solutions are not significantly reduced for the computational cost savings. Through an example, the ellipse constraint is effectively used to restrict the sampling region of the multiple-barrier space to further decrease the torque ripple. This two-step strategy helps to reduce the computational time needed to arrive at an optimal multiple-barrier design, while visualizing the behavior of high average torque solutions. In Chapter 4, a single design from the Pareto front solutions is used for the local optimization procedure. Future work could extend the application of the ellipse constraint to find optimal SynRM rotors with higher number of barriers.

## Chapter 4 LOCAL ROTOR DESIGN OPTIMIZATION

### 4.1. Introduction

Once the set of global optimum solutions are found, a single-barrier SynRM rotor design is chosen before local optimization is performed. A single-barrier SynRM solution is selected to improve its torque ripple through a multiple-barrier rotor structure. Next, a generalization methodology to map the single-barrier to multiple-barrier designs is proposed to address computational issues arising from searching high-dimensional design spaces.

### 4.2. Multiple-Barrier Rotor Design

In the subsections below, a multiple-barrier rotor is explored and modelled by using the knowledge gained from the single-barrier results in §3.2.

#### 4.2.1. Selection of a Global Optimal Design

Provided that the SynRM case study is to design a motor for a direct-drive application, the maximum average torque  $T_{avg}^{MAX}$  solutions on the Pareto fronts are considered (where  $T_{avg} = 100\%$ ). For each  $n_p$  and  $I_s$  combination, the average torque, torque ripple and rotor insulation ratio  $k_{air,r}$  results are presented in Table 9. As suggested by [32], the unitless rotor insulation ratio in (16) should be as close to the stator insulation ratio  $k_{air,s}$  as possible at high current levels. This ensures that the saturation levels in both the stator and rotor are approximately the same. For the considered 33-slot SynRM stator,  $k_{air,s}$  corresponds to 0.47 which matches well with the  $k_{air,s}$  value of 0.44 for the high  $2.0I_{rated}$  current level of the 8-pole rotor design.

**Table 9. Single-Barrier  $T_{avg}$  [Nm],  $T_{rip}$  [%] and  $k_{air,r}$  for  $\max(T_{avg})$  Results**

$n_p$	$n_s/n_p$	$0.5I_{rated}$	$1.0I_{rated}$	$2.0I_{rated}$
4 poles	8.250	240, 22.2, 0.33	449, 23.9, 0.65	766, 21.2, 0.65
<b>8 poles</b>	<b>4.125</b>	271, 6.8, 0.20	526, 13.3, 0.39	<b>842, 12.0, 0.44</b>
10 poles	3.300	242, 17.5, 0.49	455, 24.7, 0.39	708, 28.6, 0.39

While the average torque of 842 Nm of the selected 8-pole rotor is acceptable for the SynRM's reluctance torque, the torque ripple value of 12.0% at  $2.0I_{rated}$  is generally high. Although this design corresponds to a point among the set of global optima solutions, a further global refinement is not possible for this problem setting. An alternative approach must be taken to find local solutions of this global optimum in order to improve the torque ripple. In the literature [38], [50],

[53], multiple-barrier rotor models are used to distribute the magnetic flux through multiple flux carriers for decreasing the torque ripple. A generalization methodology to map single-barrier designs to multiple-barrier ones is described below. This helps to compare multiple-barrier models using the proposed RS maps and ellipse constraint from §3.2.

#### 4.2.2. Generalization to a Multiple-Barrier Design

Similar to §3.2.1, the geometric modelling of a multiple-barrier rotor follows the same procedure as a single-barrier case. The difference, however, lies in the multiplicative increase of the number of rotor variables by the number of flux barriers  $n_b$  (e.g. 2 to 4 dimensions for a double-barrier rotor). A comparison of the design variables between the single-barrier and double-barrier rotors is illustrated in Figure 42 (a) and (b) respectively (subscripts denote the barrier number). The total width constraint in (23) is still imposed to prevent infeasible designs.

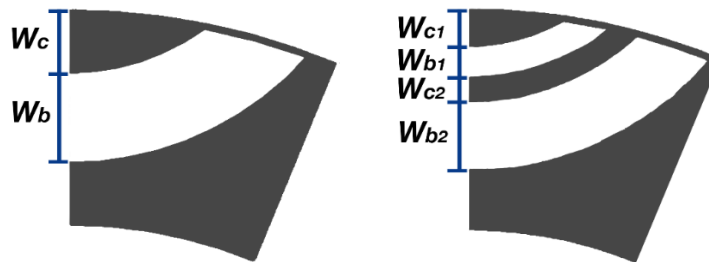


Figure 42. Rotor Half-Pole Variables: (a) Single-Barrier (left), (b) Double-Barrier (right)

Previous literature such as [52] have developed analytical relationships between the number of stator slots, the number of rotor poles and the number of rotor barriers to minimize the torque ripple in SynRMs. However, the fractional slot-per-pole number in this study leads to a desirable asymmetric flux barrier arrangement [51] which can significantly reduce the torque ripple as validated in the double-barrier example of §3.3.2. In addition, higher number of flux barriers are ignored for the local rotor optimization, but could be implemented using the proposed algorithms explained below and in §3.2.

To proceed with the local optimization of the double-barrier rotor, a sampling plan as described in §3.1.1 must be used. Due to the high number of design variables (or dimension number) of a double-barrier rotor, a Latin Hypercube sampling for 188 points is performed within and around the ellipse constraint region by considering  $W_l$  of  $0.15 pu$  in (22). This method also incorporates the knowledge that multiple magnetic flux paths can be combined into one and vice versa. By linearly summing the widths of the flux carriers and the flux barriers through (32), a slightly

improved average torque should be expected while the torque ripple should substantially decrease by distributing the stator MMF through the multiple flux carriers of the rotor.

$$W_{c/b} = \sum_{k=1}^{n_b} W_{c/b_k} \quad (32)$$

Once all the double-barrier rotor designs are sampled and solved using 2D FEA for both torque objectives, the solutions are mapped back to a single-barrier design space using (32). Through the single-barrier surrogate modelling approach in §3.2.4, the double-barrier RS maps of the two objectives are plotted in Figure 43 and Figure 44.

As observed from the two RS maps, the average torque values remain about the same as the single-barrier rotor case while the torque ripple is significantly reduced. In the double-barrier  $T_{avg}$  RS map, where the sampled points are closer to the single-barrier ellipse constraint, the constant-average torque contours have an approximately similar elliptical behavior.

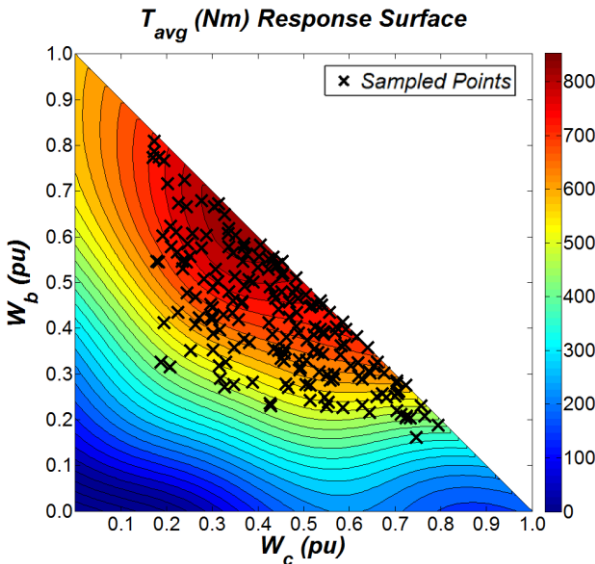


Figure 43. Double-Barrier: Average Torque RS Map for (8 poles,  $2.0I_{rated}$ )

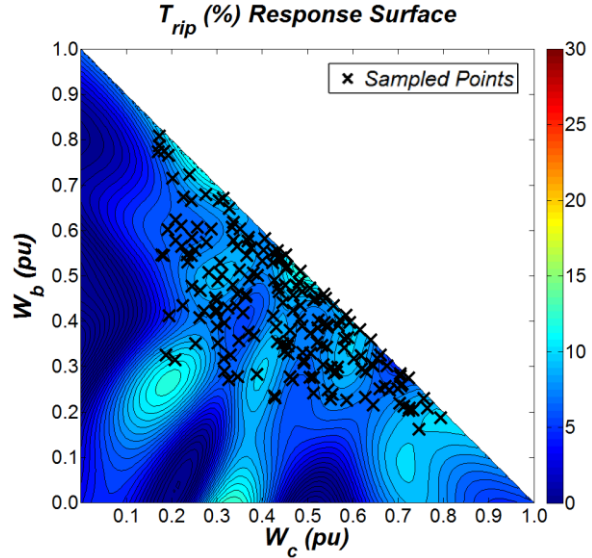


Figure 44. Double-Barrier: Torque Ripple RS Map for (8 poles,  $2.0I_{rated}$ )

For validating the multiple-barrier generalization and design comparison using the RS maps, the high average torque solution points ( $T_{avg} > 90\%$ ) are passed through the *Minimum Volume Ellipsoid* formulation in (29) and (30). This helps to capture the single-barrier and double-barrier rotor ellipses for different current levels as shown in Figure 45 (a) and (b) respectively. Comparing the two cases, the single-barrier and double-barrier center points differ by about  $0.04 pu$  which is

relatively small for assuming a linear width summation using (32). By using this generalization methodology, the computational effort invested in the local optimization of a double-barrier rotor is significantly decreased by focusing the design space sampling within the ellipse constraint.

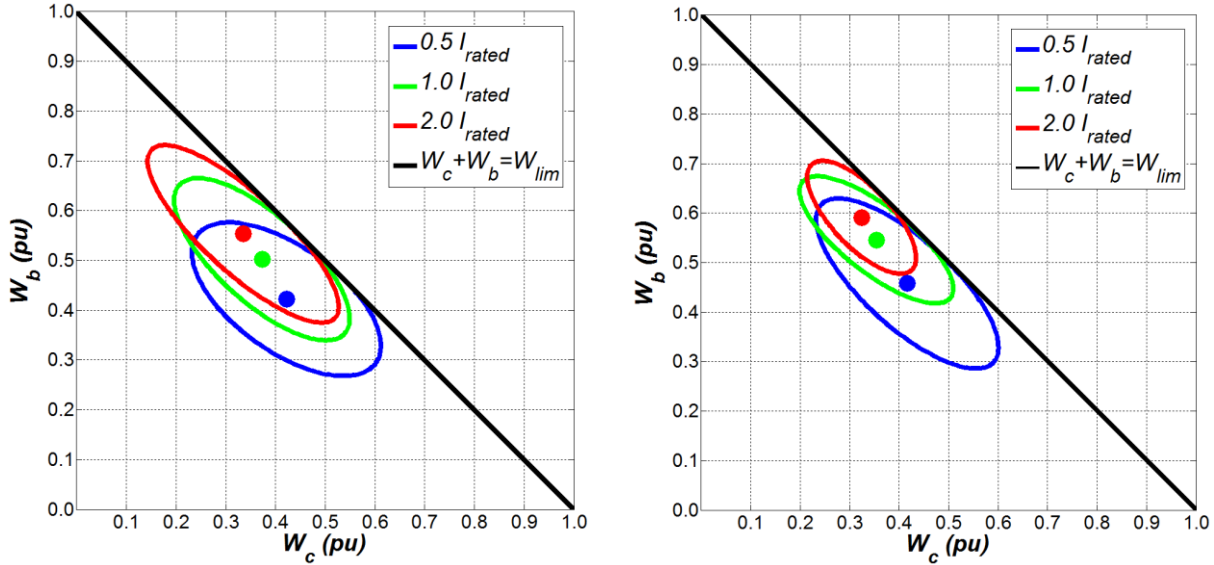


Figure 45. High  $T_{avg}$  Regions: (a) Single-Barrier (left), (b) Double-Barrier (right)

Next, the improved design for the multiple-barrier rotor corresponding to the  $T_{avg}^{MAX}$  solution is chosen. Compared to the single-barrier solution in Table 9, the torque ripple of the improved double-barrier design is significantly lower for all three currents as displayed in Table 10.

Table 10. Result Summary of Double-Barrier Design

	Objective Results		
	$0.5 I_{rated}$	$1.0 I_{rated}$	$2.0 I_{rated}$
$T_{avg}$ [Nm]	284	543	864
$T_{rip}$ [%]	6.00	7.4	6.0
Design Dimensions			
$W_{c1}$ [mm]	3.3	$W_{b1}$ [mm]	4.3
$W_{c2}$ [mm]	6.2	$W_{b2}$ [mm]	11.9
$W_c$ [pu]	0.34	$W_b$ [pu]	0.58
Overall $T_{rip}$ Statistics			
	$0.5 I_{rated}$	$1.0 I_{rated}$	$2.0 I_{rated}$
$\mu_{rip}$ [%]	13.02	10.62	8.08
$\sigma_{rip}$ [%]	5.66	3.88	2.58

Although the  $T_{avg}$  value of the double-barrier rotor increased by about 3% from the single-barrier design for  $2.0I_{rated}$ , the  $T_{rip}$  value is suitably decreased by around 50% (single-barrier: 12.0%, double-barrier: 6.0%) owing to the division of the rotor flux path by two. By comparing the torque ripple statistics of the  $\delta$ -pole single-barrier results in Table 6 with the double-barrier results in Table 10, the overall mean  $\mu_{rip}$  is much lower with a smaller variation because the sampling of the design space is focused within and around the ellipse constraint. If the double-barrier design dimensions ( $W_{c1}, W_{c2}, W_{b1}, W_{b2}$ ) are mapped using (32) to the single-barrier space and represented in the per-unit ( $W_c, W_b$ ) plane, the mapped point lies within the ellipse constraint in Figure 40. In addition, the stator and rotor saturation levels are approximately equal at high current levels by matching the double-barrier rotor insulation ratio  $k_{air,r}$  of 0.45 with 0.47 for the stator ratio.

For the double-barrier improved design, the FEA field solution in Figure 46 shows that the motor is less magnetically-loaded than in Figure 24 with fewer concentrated flux lines passing through the rotor flux carriers. This helps to improve the SynRM's efficiency level and thermal dissipation as well as decreasing the torque ripple.

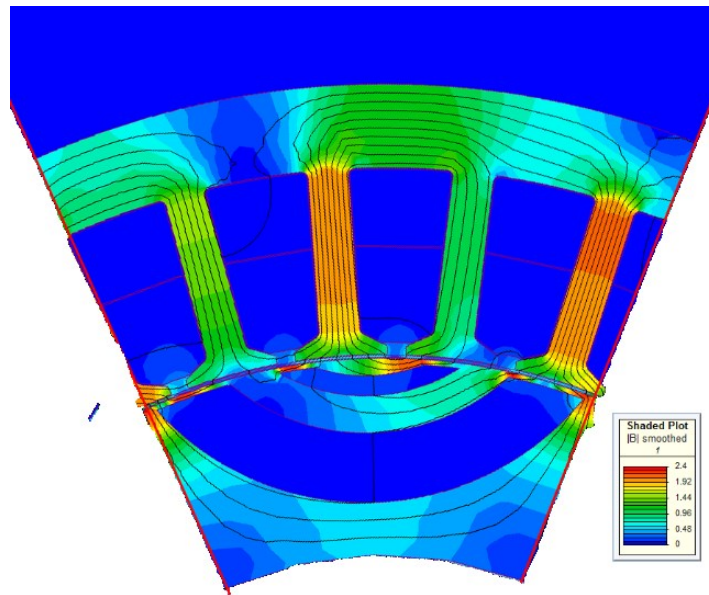


Figure 46. FEA Field Plot of the Improved Double-Barrier SynRM Rotor ( $1.0I_{rated}, 59^\circ$ )

Therefore, the proposed generalization methodology helps to find an improved SynRM rotor in the multiple-barrier design space by using an inverse-mapping from the proposed ellipse constraint in the single-barrier space for the initial sampling. This methodology is extendable to higher-barrier rotor models where a further reduction of torque ripple is expected.

### 4.2.3. Effect on Inverter Drives

Lastly, the effect of the improved double-barrier SynRM rotor design on the inverter drive is analyzed. A 3-phase inverter with a DC link of 450 V is assumed to be used at square-wave operation to find the MTPA limit at rated motor speed. This ensures a maximum available per-phase fundamental component  $V_s^{MAX}$  of  $2/\pi$  with respect to the DC link voltage using (15). Without incorporating the PM flux linkage component  $\lambda_m$  [30], the characteristic in Figure 47 is observed for different currents and rotor speeds using the current-limit circle of (13) and the voltage-limit ellipse of (14). The eccentricities of the voltage-limit ellipse decrease as the current increases. If the rotor speed is increased, the voltage-limit ellipses centered at the origin become smaller in the per-unit ( $I_d, I_q$ ) plane. This forces the inverter controller to decrease the current magnitude in order to maintain the MTPA operation. An inverse problem is then solved for the maximum rotor rated (or base) speed  $N_{base}$  using (14) for each current level. For example, an output power of about 91 kW at a maximum base speed of 1005 RPM was calculated at  $2.0I_{rated}$ . For rated current conditions, the output power at the 1192 RPM base speed is about 68 kW.

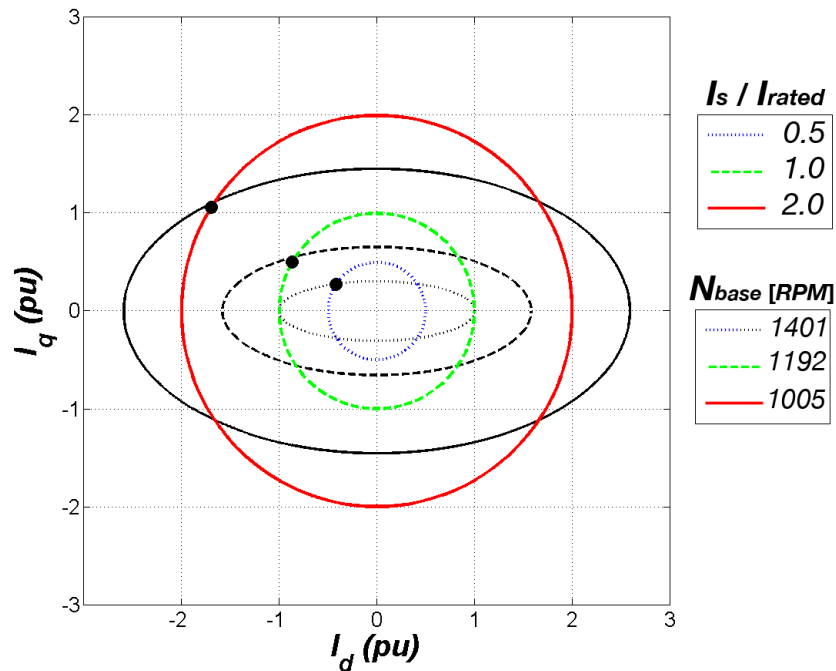


Figure 47. Current-Limit Circles (blue, green, red) and Voltage-Limit Ellipses (black) for Different Currents and Rotor Speeds of the Double-Barrier Improved Design

Although the reluctance torque of the SynRM rotor is optimized, the rated torque and the FW power (543 Nm, 68 kW) still do not match the case study requirements (967 Nm, 160 kW) in Table

3. Previously mentioned in §1.3, a pure SynRM cannot provide a high torque-to-rotor volume density and has limited Flux-Weakening capability because the voltage-limit ellipses are not centered in the left-half plane of the  $(I_d, I_q)$  plane. To alleviate these problems, permanent magnets can be incorporated within the rotor segment through a PM-assisted SynRM.

### 4.3. Permanent Magnet-Assisted Rotor Design

To meet the case study specifications, permanent magnets are inserted within the rotor structure of a pure SynRM to improve its performances. This hybrid design, known as a PM-assisted SynRM, has a higher torque-rotor-volume density and power factor, maintains an acceptable constant power during high speeds, saturates its rotor iron ribs and is well-suited to sensorless position control (through high-frequency signal injection) due to its rotor anisotropy [65].

Hence, the barrier refinements needed to realistically insert PMs are explored before comparing the performances of the *initial IPM* (refer to §2.4) with the final PM-assisted SynRM design. The theoretical IPM parameter plane described earlier in §2.3.1 is used to validate the final hybrid rotor solution. Finally, a robustness analysis of the two objectives is performed with respect to the rotor geometric parameters, the remanent flux densities of the permanent magnets and the current phase magnitudes to account for variable uncertainties.

#### 4.3.1. Barrier Refinements

By referring to (5), adding permanent magnets within the SynRM rotor structure can improve the motor's overall torque production by producing both reluctance and PM torque components. It is not feasible, however, to insert rectangular permanent magnets inside the rotor structure with circular flux barriers in Figure 22. This manufacturing problem is avoided by refining the flux barrier shapes to an angled version shown in Figure 48 for the improved double-barrier SynRM rotor. All the flux carrier and barrier widths are kept the same as the previous circular version, and the radially-magnetized rectangular permanent magnets can be inserted in both the inner and outer segments of the angled flux barriers. By removing the permanent magnets and solving for both the average torque and torque ripple using 2D FEA simulations, the performance results of the angled-barrier design in Figure 48 are found to be close to that of the optimized circular-barrier one in Table 10. In this angled-barrier design,  $W_i$  is the inner magnet width,  $W_o$  is the outer magnet width and  $\theta$  is the outer magnet orientation with respect to the inner magnet.

Before local geometric optimization of the PM-assisted SynRM rotor, the permanent magnet grade must be chosen. For this electromagnetic analysis, only electromagnetic effects at  $20^{\circ}\text{C}$  room temperature are considered and magnet demagnetization is ignored. The different demagnetization BH curves for three considered PMs are shown in Figure 49: *ceramic*, *bonded NdFeB* and *sintered NdFeB*. A brief review of each magnet's properties is described below.

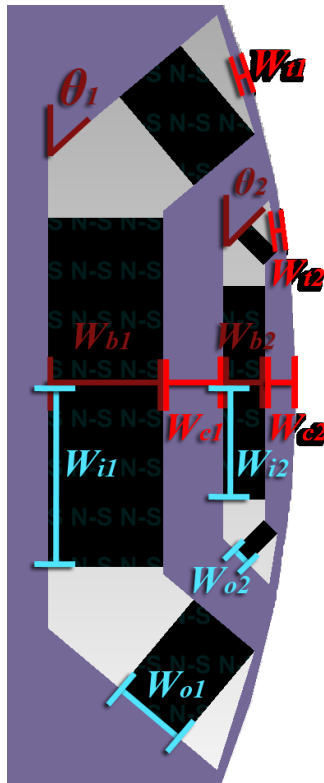


Figure 48. Rotor Geometric Variables for Angled Flux Barriers (radial PM magnetization)

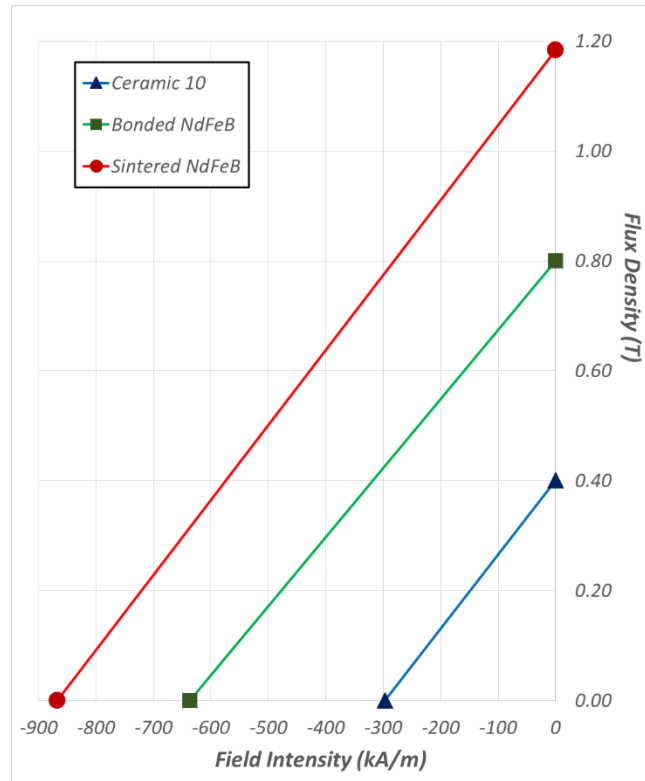


Figure 49. Demagnetization BH Curves for Different Magnets at  $20^{\circ}\text{C}$  Temperature

*Ceramic* magnets, also known as *ferrites*, are both brittle and hard and have a maximum energy product of up to  $3.5 \text{ MGOe}$  ( $27.9 \text{ kJ/m}^3$ ). Its common manufacturing process uses *sintering* which compacts the fine alloy powder in a die before fusing it into a solid material through heat [66]. As demonstrated in previous works [25], [50], [67], the popularity of using ceramic magnets in electric machine applications is due to its availability, demagnetization resistance, negative temperature coefficient and low relative cost [66]. On the other hand, *Neodymium Iron Boron* (NdFeB) is a rare-earth magnet material with the highest energy product reaching  $52 \text{ MGOe}$  ( $413.8 \text{ kJ/m}^3$ ) for its *sintered* variation. While they are costly and prone to market fluctuations, they are generally preferred in electric machine applications in order to reduce the motor's volume. A middle-ground between *ceramic* and *sintered* NdFeB magnets is the *bonded* NdFeB magnet which is formed by

injection molding of the NdFeB powder with mixed polymer into different complex shapes. Their main drawback is their lower energy product as shown in Figure 49.

The *initial IPM* design displayed in Figure 19 uses a sintered NdFeB magnet with a high coercive field intensity  $H_c$  and remanent flux density  $B_r$  of around  $1.2 T$ . In order to reduce the material cost of the PM-assisted SynRM, cheaper permanent magnet alternatives such as Ceramic 10 ( $0.4 T$ ) and bonded NdFeB ( $0.8 T$ ) are considered. Although these magnets have a smaller  $B_r$  and  $H_c$  than the sintered NdFeB, a slight PM torque is required to assist the optimized reluctance torque.

Hence, the PM-assist problem is simplified by constraining the total area of the Ceramic 10 permanent magnets per rotor pole  $A_{lim}$ . Due to the weaker performances of cheap magnet alternatives, a higher area (or volume) of rotor PMs is used compared to the magnet mass reported in Table 4 for the *initial IPM* motor. The constant value of  $A_{lim}$  fixes the amount of inserted magnets within the two barriers and helps to operate the PM-assisted SynRM in the optimal IPM design line as explained in §2.3.1. Afterward in §4.3.2, the final design's performance is validated against the IPM parameter plane.

For the 6 rectangular PMs shown in Figure 48, the geometric variables  $W_i$ ,  $W_o$  and  $\theta$  for the two angled flux barriers are optimized with respect to the average torque and torque ripple objectives. Both outer magnet orientation variables  $\theta_1$  and  $\theta_2$  are discretized between  $40^\circ$  to  $65^\circ$  in  $5^\circ$  steps. For every combination of  $\theta_1$  and  $\theta_2$ , the widths of the inner and outer magnets  $W_i$  and  $W_o$  are varied according to the area constraint in (33). Provided that the inner PMs are larger in size relative to its neighboring magnets, the former produce most of the PM torque. Therefore across both flux barriers, the inner magnet widths  $W_i$  are always maximized before varying the outer magnet widths  $W_o$  while satisfying (33). In §4.4, this assumption is verified through a robustness analysis of the remanent flux densities for the inner and outer PMs.

$$\sum_{k=1}^{n_b} (W_{i_k} + W_{o_k}) W_{c_k} \leq A_{lim} \quad (33)$$

Upon calculating the MTPA average torque and torque ripple values for all  $(\theta_1, \theta_2)$  combinations using FEA simulations, the values are plotted in the objective space to observe the Pareto front. By mapping these optimal solutions to the  $(\theta_1, \theta_2)$  design space, the corresponding contour plots in Figure 50 (a) and (b) are produced for the average torque and torque ripple respectively. Each

plot represents monotonically an increasing or decreasing behavior, but in the opposite direction of one another. For the average torque case, its contour values approximately range from 1310 to 1361 Nm with a single peak existing around  $(\theta_1, \theta_2) = (45, 45)^\circ$ . On the other hand, the torque ripple values roughly range from 3.7% to 7.3%. To satisfy a high average torque solution along the Pareto front, a single solution at  $(\theta_1, \theta_2) = (45, 50)^\circ$  is then selected.

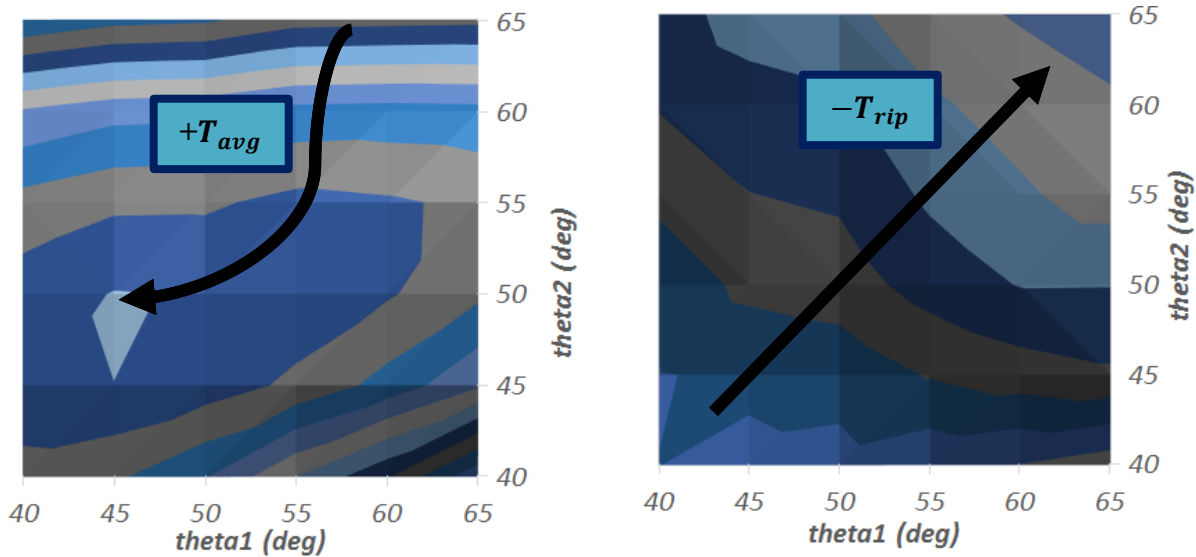


Figure 50. Contour Plots of (a) Average Torque (b) Torque Ripple

The barrier-refined design with respect to both objectives is presented in the summarized results of Table 11. By using the Ceramic 10 magnets, the rated average torque has significantly improved compared to that of the pure SynRM rotor and is closer to the *initial IPM* ratings. Despite the increase of torque ripple for  $0.5I_{rated}$ , the torque ripple values remained relatively low for both  $1.0I_{rated}$  and  $2.0I_{rated}$ .

Table 11. Result Summary of the 2B-PMa SynRM (Ceramic 10)

	Objective Results		
	0.5I <sub>rated</sub>	1.0I <sub>rated</sub>	2.0I <sub>rated</sub>
T <sub>avg</sub> [Nm]	428.3	832.5	1360.2
T <sub>rip</sub> [%]	8.92	2.33	5.13
Design Dimensions			
W <sub>i1</sub> [mm]	11.0	W <sub>o1</sub> [mm]	2.0
W <sub>i2</sub> [mm]	18.0	W <sub>o2</sub> [mm]	8.2
θ <sub>1</sub> [°]	45	θ <sub>2</sub> [°]	50

If the performance is desired to be further improved, bonded NdFeB magnets can be used instead of the Ceramic 10 magnets. This analysis is carried out in the next subsection to evaluate the power-speed characteristic of the *double-barrier PM-assisted SynRM*, renamed as *2B-PMa SynRM*, using bonded NdFeB magnets, and to compare its overall results with the *initial IPM* and *TM4 Sumo MD* motors.

#### 4.3.2. Power-Speed Characteristic

In the previous sections, the torque performances of the SynRM are calculated at the MTPA point (refer to §2.2.2) by assuming that the rotor has not exceeded its rated speed at steady-state. To analyze a motor's behavior in the constant power or *Flux-Weakening* (FW) region at high speeds, a *3-phase* inverter bridge is coupled with a motor through a common circuit simulation (refer to §2.1.1 and §2.2.3). The computed power-speed (or *P-N*) characteristics can then be compared with the ideal power curve in Figure 10, while imposing the limitations of a fixed DC bus voltage and non-ideal winding currents.

*PWM analysis* in the *MotorSolve* software is used to obtain a motor's *P-N* characteristic. Here, a motor model is connected to a *3-phase* inverter bridge, as shown in Figure 7 (a), which operates in current regulation mode at a high switching frequency [43]. A surrogate model of the motor is created using a small set of FEA solutions to save computation time in the co-simulation. Next, the inverter and motor are coupled together in a circuit simulation to calculate the electric drive performances. Although there are different PWM algorithms available such as Sine-PWM or Space Vector Modulation, the *Current Hysteresis* method is considered in this work due to its simplicity in approximating the motor's FW performance through a current-driven approach. This method regulates the non-ideal winding currents within a hysteresis band above and below a reference current waveform [9]. By assuming a 2-level inverter operation, the resulting PWM voltage waveform either increases or decreases the winding currents as 2 separate states (through a time-integral relationship) [34]. Once the current has reached either one of its hysteresis band limits, the PWM voltage waveform reverses its current state, similar to bang-bang control.

A suitable sine wave current is created in the phase windings by using at least 20 PWM chops in one cycle as suggested in [9]. For a maximum rotor speed of 3100 RPM and a high switching frequency of 16 kHz, each PWM cycle contains at least 70 chops which is sufficient to approximate

a sine wave current. Even though a high PWM switching frequency directly impacts the transistor switching losses, this effect is ignored for the FW performance estimation.

Figure 51 below displays the  $P-N$  characteristics of two current excitations of the  $2B-PMa$  SynRM with bonded NdFeB magnets ( $0.8 T$ ). For each current waveform with a hysteresis band of  $\pm 7.5 A$ , the advance angle is varied between  $55^\circ$  to  $85^\circ$  range in  $5^\circ$  increments for all rotor speeds up to a maximum of  $3100 RPM$  in steps of  $100 RPM$ .

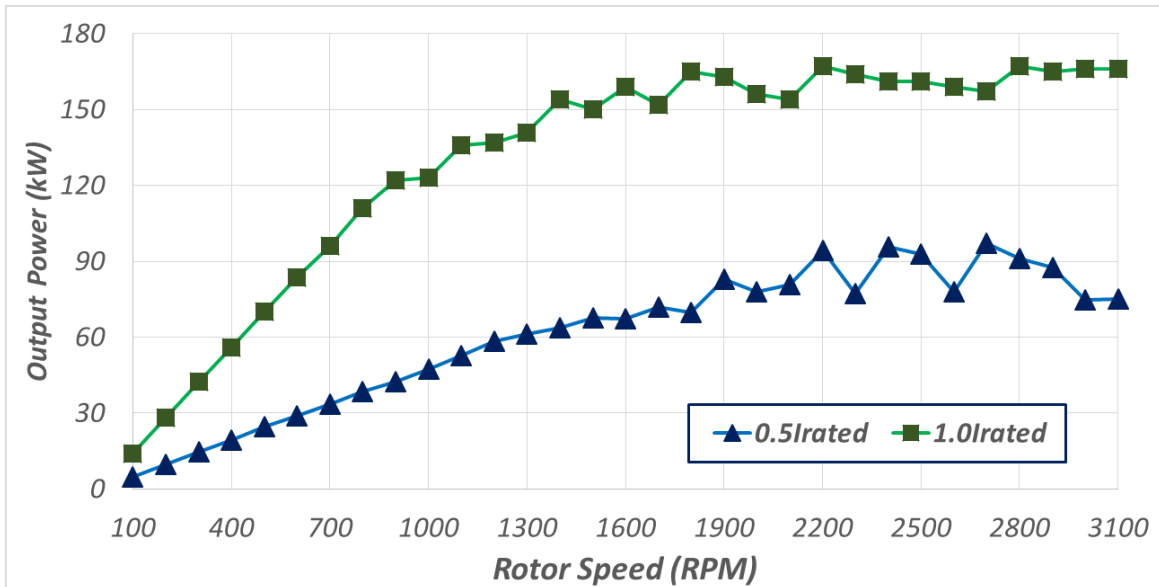


Figure 51.  $2B-PMa$  SynRM: Power-Speed Characteristics

In order to avoid misinterpretation of the  $PWM$  analysis results, the  $2.0I_{rated}$  operation is ignored: the motor's ferromagnetic saturation is high at this current. For the other non-saturated  $0.5I_{rated}$  and  $1.0I_{rated}$  conditions, the  $2B-PMa$  SynRM has not yet saturated allowing for a linear BH-curve approximation. The output power of both currents are validated using 2D FEA simulations at speeds below rated operation. Moreover in the constant power or FW region, the  $1.0I_{rated}$  curve peaks at about  $174 kW$  which meets the  $180 kW$  continuous operation requirement of the  $TM4$  Sumo MD motor. A further comparison of different motor designs is presented by referring back to the case-study requirements in §2.4 and the IPM parameter plane of §2.3.1.

#### 4.3.3. Design Comparison

Table 12 below compares the simulated performances of the  $2B-PMa$  SynRM ( $0.8 T$ ) and the initial IPM motor ( $1.2 T$ ) with the  $TM4$  Sumo MD motor [44] using 2D FEA. The latter machine employs an SMPM outer rotor with rare-earth magnets for driving heavy-duty HEVs in an urban setting

(refer to §2.4). Using the presented results of  $T_{avg}^{MAX}$ ,  $T_{avg}^{CONT}$  and  $P_{FW}^{CONT}$ , the *2B-PMa SynRM*'s ratings match well with the *TM4 Sumo MD* motor. Also the *2B-PMa-SynRM* produces considerably more torque at higher currents than the *initial IPM* motor for the same volume, because it relies more on its optimized reluctance torque component (due to a higher saliency ratio  $\xi$ ). At low current operation of  $0.5I_{rated}$ , the efficiency and power factor of the *2B-PMa SynRM* are comparable with the *Initial IPM* motor which helps to reduce the inverter's oversizing and cost. From the presented results, it may be deduced that the *2B-PMa SynRM* is superior to the *Initial IPM* motor. Considering the direct-drive application, it is necessary to prove the coupled effects of the design improvements on the average torque and FW performance.

**Table 12. Performance Comparison between Different Motors**

Performance Specification	<i>TM4 Sumo MD</i> [44]	<i>Initial IPM</i>	<i>2B-PMa SynRM</i>	$I_s/I_{rated}$ Operation
<i>Volume (L)</i>	-	22.81	-	-
$T_{avg}^{MAX}$ (Nm)	2100	1468	2231	2.67
$T_{rip}$ (%)	-	6.15	3.12	2.67
$T_{avg}^{CONT}$ (Nm)	1000	1122	1389	1.34
$P_{FW}^{CONT}$ (kW)	180	160	183	1.34
$\eta^{MAX}$ (%)	95.0	96.0	95.5	0.50
$\cos \phi$	-	0.925	0.935	0.50

Firstly, the  $T_{avg}$  values at different stator currents are simulated using 2D FEA for three motors: the *Initial IPM* motor with sintered NdFeB magnets, and the *2B-PMa SynRM* with Ceramic 10 and bonded NdFeB magnets. This helps to identify the current needed to satisfy the desired torque. Figure 52 presents the three quadratically-fitted curves for the compared motors.

The torque constraints ( $T_{avg}^{CONT}$ ,  $T_{avg}^{MAX}$ ) of the *TM4 Sumo MD* are displayed using solid black lines. For the different curves, the *Initial IPM* saturates faster than the other two motors. Its leading torque values at low currents is due to its significantly higher rotor PM content. However at higher currents, the average torques of the *2B-PMa SynRM* for both magnet cases dominate the *Initial IPM*'s, because the optimized reluctance torque of the *2B-PMa SynRM* helps to produce higher torque in overloaded motor conditions. For the bonded NdFeB magnet case, it can satisfy both torque constraints at lower current levels (93%, 239%) compared to the other motors.

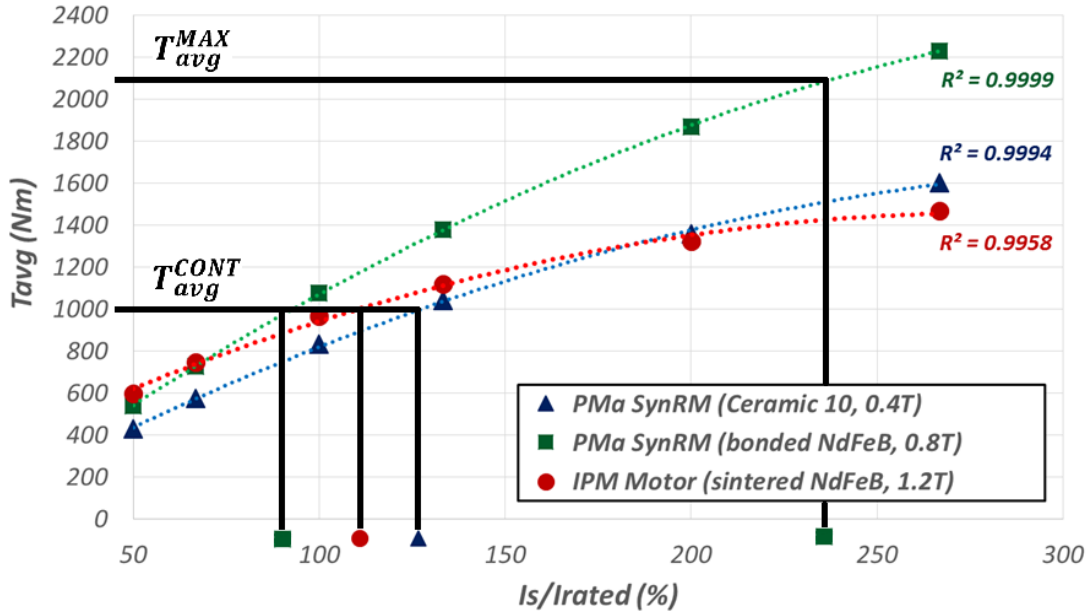


Figure 52. Average Torque Comparison between Different Motors

This result demonstrates by example the importance of relying on reluctance torque with sufficient PM-assist in a Synchronous Reluctance Machine. Simply employing high-grade sintered NdFeB magnets in an IPM rotor structure does not guarantee meeting the torque requirements. This analysis is next explained by means of the IPM parameter plane introduced under §2.3.1.

In the second part, the IPM parameter plane is used to compare the trajectories of the *Initial IPM* and the *2B-PMa SynRM* bonded NdFeB magnets for different currents. This plane consists of two axes, the rotor saliency ratio  $\xi$  and the normalized PM flux linkage  $\lambda_{mn}$ , which represent the amount of reluctance and PM torque components. By using (3), (7), (8), (13) and (14) in per-unit form and without winding losses, two drive characteristics are derived and displayed for each pair of  $(\xi, \lambda_{mn})$ : the IUR in Figure 53 and the normalized maximum drive speed in Figure 54.

The trajectories of the two motor are calculated using (1) and (2) for different MTPA currents and are shown on top of the two contour plots. Note that a saliency ratio value below 1 represents an inverse saliency ( $L_d > L_q$ ) which is not typically exploited in electric machines. As the current and saturation levels increase, both  $\xi$  and  $\lambda_{mn}$  decrease for the two motors due to saturation effects.

For the *initial IPM*, its trajectory indicates almost no saliency (low reluctance torque) as expected. It has significantly large  $\lambda_{mn}$  values (high PM torque) owing to its use of sintered NdFeB PMs. In the *2B-PMa SynRM* case, however, its optimized reluctance torque is a byproduct of its high  $\xi$

(acceptable for TLA rotor types) with enough  $\lambda_{mn}$  for torque-assist. Given that pure SynRMs suffer from low power factors as explored in §2.2.1, the addition of rotor PMs helps alleviate this problem. If the  $\lambda_{mn}$  component at  $0.5I_{rated}$  is disregarded for a pure SynRM ( $\xi = 2.54, \lambda_{mn} = 0$ ), a meagre MPF of about  $0.429$  using (10) is calculated which is considerably lower than the  $0.935$  value reported in Table 12 for the PM-assisted version. Referring back to the different drive class in Figure 17 (b), the *initial IPM* trajectory suggests that it operates as a “finite-speed SMPM”, while the *2B-PMa SynRM* acts as a “finite-speed IPM”.

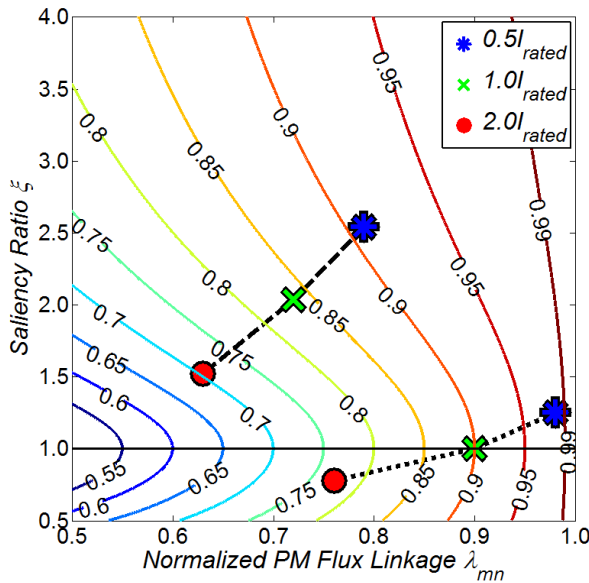


Figure 53. Inverter Utilization Ratio for *2B-PMa-SynRM* (dashed) and *Initial IPM* (dotted)

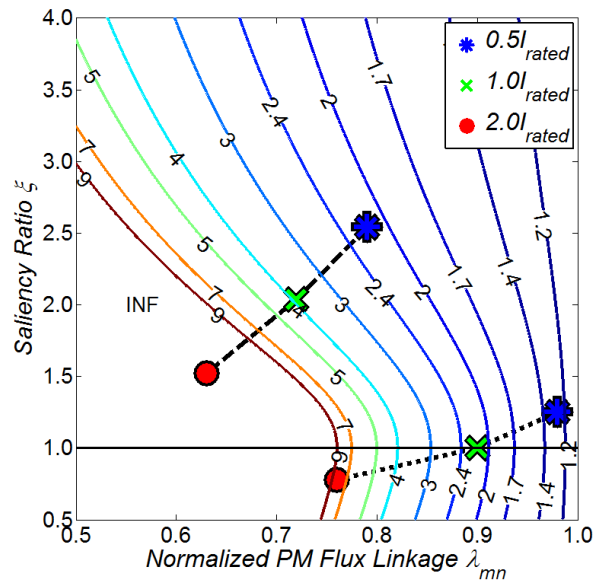


Figure 54. Normalized  $N_{max}$  for *2B-PMa-SynRM* (dashed) and *Initial IPM* (dotted)

From the IUR contour plot in Figure 53, it is observed that both motors have reasonably high and comparable IUR values that leads to benefits in reducing the oversizing and cost of the inverter. The IUR values for the  $0.5I_{rated}$  case are relatively close to the product of the efficiency and power factor values (*2B-PMa SynRM*:  $0.955 \times 0.935 = 0.893$ ) in Table 12.

Figure 54 suggests that the *2B-PMa SynRM* has a more suitable FW or high-speed characteristic for a traction application. Its trajectory tends toward the theoretical “optimal IPM design line” which also matches well with the power-speed characteristics in Figure 51 for a maximum speed of  $3100$  RPM for the *TM4 Sumo MD*.

Minor differences between the IPM parameter plane trajectories and simulated performances exist, because the analysis assumes no winding or iron losses in the drive characteristic calculations.

Nevertheless, it provides a useful motor comparison tool that matches well with the 2D FEA simulation results. Using bonded NdFeB magnets within the double-barrier rotor of the PM-assisted SynRM provides a better FW operation, requires lower currents for matching different torque constraints, and improves the efficiency and power factor.

#### 4.4. Robustness Analysis

The robustness of the  $2B\text{-}PMa$  SynRM rotor is analyzed by considering the uncertainty effects from the manufacturing process, magnetic material properties, and motor controller setpoints on the average torque and torque ripple objectives at nominal  $1.34I_{rated}$  operation.

Firstly, an extreme sensitivity analysis is performed for the nominal rotor design in Figure 48 for the  $(W_{c1}, W_{c2}, W_{t1}, W_{t2}, \theta_1, \theta_2)$  geometric parameters to account for manufacturing uncertainties. Each parameter is varied between a lower and upper limit using a *full factorial* sampling for 6 variables and 2 levels resulting in 64 different combinations (refer to §3.1.1). A tabulated summary of the geometric variations is given in Table 13, where the width dimensions and the outer magnet orientations are varied within  $\pm 0.1$  mm and  $\pm 2^\circ$  respectively.

Secondly, the magnet grades are subjected to uncertainty by varying their remanent flux density  $B_r$  values for two different cases. In the first case, the  $B_r$  values of the 6 bonded NdFeB magnets across 1 rotor pole are varied within  $\pm 0.05$  T as shown in Table 14 and Figure 55.

**Table 13. Extreme Variations of Geometric Parameters across 1 Rotor Pole**

Parameter	Min.	Nom.	Max.
$W_{c1}$ [mm]	3.15	3.25	3.35
$W_{c2}$ [mm]	6.07	6.17	6.27
$W_{t1}$ [mm]	0.9	1.0	1.1
$W_{t2}$ [mm]	0.9	1.0	1.1
$\theta_1$ [°]	43	45	47
$\theta_2$ [°]	48	50	52

**Table 14. Extreme Variations of Remanent Flux Density Parameters across 1 Rotor Pole**

Parameter	Min.	Nom.	Max.
$B_r^1$ [T]	0.75	0.80	0.85
$B_r^{2a}$ [T]	0.75	0.80	0.85
$B_r^{2b}$ [T]	0.75	0.80	0.85
$B_r^3$ [T]	0.75	0.80	0.85
$B_r^{4a}$ [T]	0.75	0.80	0.85
$B_r^{4b}$ [T]	0.75	0.80	0.85



**Figure 55. Remanent Flux Density Parameters of 6 PMs across 1 Rotor Pole**

This results in 64 different combinations by using a similar *full factorial* sampling. For the second case, all the  $B_r^1$  magnets across the 8 rotor poles are assumed to be uncertain within  $\pm 0.05 T$  while the  $B_r$  values of other magnets are kept constant at the nominal  $0.80 T$  value. Only the  $B_r^1$  magnet is considered, because it contributes the most in producing the motor's PM torque and the computational time needed to simulate different models for 1 mechanical period is high. Although there seems to be 256 different possibilities, several sequences are simply rotated versions of other combinations. For example, if the low and high limits of  $B_r^1$  are encoded using 0 and 1 digits, the  $B_r^1$  10000001 sequence across the 8 rotor poles results in a phase-shifted version of the calculated instantaneous torque as the other sequences 11000000, 01100000, 00110000, etc. These redundant sequences are ignored to ensure that only 36 unique combinations are simulated.

Thirdly, the 3-phase current magnitudes  $I_s^A$ ,  $I_s^B$  and  $I_s^C$  are assumed to be uncertain within  $\pm 5\%$  to account for variations in the motor controller setpoints. Since the sum of all 3-phase currents should be zero, only  $I_s^A$  and  $I_s^B$  are varied within  $\pm 5\%$  to result in 4 different combinations. At any time instant  $t$ , the instantaneous current  $i_s^C(t)$  of phase C is enforced using (34).

$$i_s^C(t) = -i_s^A(t) - i_s^B(t) \quad (34)$$

All the different combinations in the robustness analyses are solved using 2D FEA simulations by fixing the MTPA advance angle at  $52.5^\circ$  for the nominal  $1.34I_{rated}$  operation ( $1389 Nm$ ,  $7.22\%$ ). To calculate the relative sensitivity  $\Delta f_r$  of each objective with respect to its nominal value  $f_{nom}$ , the peak-to-peak objective difference  $\Delta f$  is calculated using (35).

$$\Delta f_r = \frac{\Delta f}{|f_{nom}|} = \frac{|\max(f) - \min(f)|}{|f_{nom}|} \quad (35)$$

The presented results in Table 15 demonstrate that the torque ripple objective is the most sensitive for the different robustness analyses. For the geometric, remanent flux density and phase current magnitude variations, the torque ripple is increasingly more prone to change with respect to the varied parameters. The average torque, however, displays more resilience against high deviation about nominal parameter values. As expected,  $B_{r_1}$  is the most contributing remanent flux density of all the 6 rotors PMs upon analyzing all the torque results for the different  $B_r$  (1 pole) variations. Therefore, this rotor design appears to be relatively robust for the extreme variations of the geometrical parameters, material properties and control setpoints introduced in this analysis.

---

Table 15. Sensitivity Results of the 2 Objectives to Extreme Parameter Variations

	Geometric (1 pole)		$B_r$ (1 pole)		$B_{r1}$ (8 poles)		$I_s$ (1 pole)	
	$T_{avg}$ [Nm]	$T_{rip}$ [%]	$T_{avg}$ [Nm]	$T_{rip}$ [%]	$T_{avg}$ [Nm]	$T_{rip}$ [%]	$T_{avg}$ [Nm]	$T_{rip}$ [%]
$\Delta f$ Value	25.31	1.80	74.14	1.87	37.97	2.01	114.52	3.19
$\Delta f_r$ [%]	1.82	24.93	5.34	25.90	2.73	27.84	8.24	44.18

#### 4.5. Conclusion

Upon globally optimizing a single-barrier Synchronous Reluctance Machine rotor in Chapter 3, one design from the Pareto front of Figure 39 is chosen to locally optimize it in the current chapter. The presented optimization mostly deals with increasing the number of rotor flux barriers to suppress the torque ripple, refining the flux barrier shapes from circular to angled versions, and inserting rectangular PMs using low-cost alternatives to the sintered NdFeB variation employed in the *initial IPM* motor shown in Figure 19. Adding PMs is motivated through the drive analysis in §4.2.3 which quantitatively demonstrates that a pure SynRM rotor cannot satisfy the required torque-to-rotor volume and Flux-Weakening capabilities in traction applications.

Relying on the analysis methods previously explained in §2.2.3 and §2.3.1, the power-speed characteristic, torque performances and drive features of a *double-barrier PM-assisted SynRM* is directly compared with the provided specifications of the *TM4 Sumo MD* [44] and *initial IPM* motors. The final rotor design matches well with the given set of drive requirements, including continuous and maximum values of both average torque and output power as well as the maximum efficiency and power factor at low current levels. However, a main drawback of the *double-barrier PM-assisted SynRM* is the lower torque-to-rotor volume due to its larger size.

Toward the end of this chapter, a robustness analysis with respect to the average torque and torque ripple is performed for variations in geometrical parameters, material properties and control setpoints. Even though the parameter deviations about their nominal values are significant, only the torque ripple is found to exhibit more sensitivity than the average torque. Based on the presented results, geometrical changes are observed to have a small effect on both objectives while the varying magnitude of the current waveform has a more prominent influence.

## Chapter 5 CONCLUSION

In this thesis, the rotor design optimization of a PM-assisted Synchronous Reluctance Machine was proposed to address the price increase of rare-earth magnets while sustaining the expected drive performances. Rather than experimentally constructing several rotor designs, a virtual laboratory using numerical simulations was created to quickly and efficiently calculate the motor performances. Starting with a global optimization approach, the set of Pareto optimal solutions were obtained and classified using an ellipse constraint in the continuous search space. Different numerical methods, lumped circuit parameters and design methodologies were used to tackle the computational and design challenges in finding the global optimal solutions: the MTPA peak finding algorithm in §3.2.2, the BRNN training algorithm in §3.2.4, the minimum volume ellipse constraint in §3.2.5, and the single-barrier to multiple-barrier generalization in §4.2.2. Only the average torque and torque ripple objectives were considered in this work. The final design results with lower cost permanent magnets matched the case study requirements and performed well in comparison with an industrial motor for a direct-drive application.

Further work could focus on refining the proposed methodologies for different slots-per-pole combinations. This helps to identify the general design relationships in order to model any SynRM rotor with initial geometric suggestions for a fixed stator structure. Including more objectives, such as efficiency and power factor, could be used to analyze the relative sensitivities of the computational methods and objective conflicts with the average torque and torque ripple. Conflicts in higher objective dimensions tends to introduce additional computational challenges in designing electric machines. Instead of relying on neural networks for the surrogate modelling, a kriging-assisted approach may be used to deal with the convergence issues in the network's training process. The multimodal behavior of the torque ripple's dataset led to greater errors in the result validation with FEA simulations. Also, the proposed ellipse constraint was only discussed with respect to the presented case study. Variability of its mathematical parameters to the number of rotor poles, number of stator slots, motor sizing and other potential variables could be explored to analytically represent a general optimality rotor constraint. An interesting exercise would be to find the underlying physical interpretation of the ellipse constraint through magnetic circuit analysis. Lastly, the mutual effect of an inverter drive could be further studied for the MTPA and FW operations at different speeds of the PM-assisted Synchronous Reluctance Machine.

**BIBLIOGRAPHY**

- [1] U.S. Department of Energy, "Annual Energy Review," 2011. [Online]. Available: [www.eia.gov/totalenergy/data/annual/index.cfm](http://www.eia.gov/totalenergy/data/annual/index.cfm).
- [2] M. Ehsani, Y. Gao and A. Emadi, Modern Electric, Hybrid Electric, and Fuel Cell Vehicles: Fundamentals, Theory, and Design, 2nd ed., CRC Press, 2009.
- [3] U.S. Department of Energy, "Emissions from Hybrid and Plug-In Electric Vehicles," 2012. [Online]. Available: [www.afdc.energy.gov/vehicles/electric\\_emissions.php](http://www.afdc.energy.gov/vehicles/electric_emissions.php).
- [4] Government of Canada, "Automotive Partnership Canada," 2014. [Online]. Available: [www.apc-pac.ca/index\\_eng.asp](http://www.apc-pac.ca/index_eng.asp).
- [5] U.S. Department of Energy, "FreedomCAR & Fuel Partnership Plan," Mar. 2006. [Online]. Available: [www.hydrogen.energy.gov/pdfs/fc\\_fuel\\_partnership\\_plan.pdf](http://www.hydrogen.energy.gov/pdfs/fc_fuel_partnership_plan.pdf).
- [6] U.S. Department of Energy, "Vehicle Technologies Office: Multi-Year Program Plan 2011-2015," Dec. 2010. [Online]. Available: [www.energy.gov/eere/vehicles/downloads/us-drive-vehicle-systems-and-analysis-technical-team-roadmap](http://www.energy.gov/eere/vehicles/downloads/us-drive-vehicle-systems-and-analysis-technical-team-roadmap).
- [7] U.S. Department of Energy, "Annual Energy Outlook 2015 with projection to 2040," Apr. 2015. [Online]. Available: [www.eia.gov/forecasts/aeo/pdf/0383\(2015\).pdf](http://www.eia.gov/forecasts/aeo/pdf/0383(2015).pdf).
- [8] P. C. Krause, O. Wasynczuk and S. D. Pekarek, Electromechanical Motion Devices, 2nd ed., Wiley-IEEE, 2012.
- [9] J. R. Hendershot, "Electric Machine Design," 2012. [Online]. Available: [http://cusp.umn.edu/machine\\_design.php](http://cusp.umn.edu/machine_design.php).
- [10] I. Boldea, L. Tutelea, L. Parsa and D. Dorrell, "Automotive Electric Propulsion Systems with Reduced or No Permanent Magnets: An Overview," *IEEE Trans. Ind. Electron.*, vol. 61, no. 10, pp. 5696-5711, Oct. 2014.

- [11] T. Fukami, M. Momiyama, K. Shima, R. Hanaoka and S. Takata, "Steady-State Analysis of a Dual-Winding Reluctance Generator With a Multiple-Barrier Rotor," *IEEE Trans. Energy Convers.*, vol. 23, no. 2, pp. 492-498, Jun. 2008.
- [12] J. K. Kostko, "Polyphase reaction synchronous motors," *J. Amer. Inst. Elect. Eng.*, vol. 42, pp. 1162-1168, Nov. 1923.
- [13] T. Matsuo and T. Lipo, "Rotor design optimization of synchronous reluctance machine," *IEEE Trans. Energy Convers.*, vol. 9, no. 2, pp. 359-365, Jun. 1994.
- [14] R. R. Moghaddam, *Synchronous Reluctance Machine (SynRM) Design*, Stockholm: KTH Royal Institute of Technology, 2007.
- [15] J. Haataja, *A Comparative Performance Study of Four-Pole Induction Motors and Synchronous Reluctance Motors in Variable Speed Drives*, Lappeenranta: Lappeenranta University of Technology, 2003.
- [16] P. Niazi, *Permanent Magnet Assisted Synchronous Reluctance Motor Design and Performance Improvement*, College Station, TX: Texas A&M University, 2005.
- [17] T. J. E. Miller, *Switched Reluctance Motors and their Control*, Oxford: Magna Physics Publishing, Oxford University Press, 1993.
- [18] T. A. Lipo, "Synchronous Reluctance Machines - A Viable Alternative for AC Drives?," *Electric Machines and Power Syst.*, vol. 19, pp. 659-671, May 1991.
- [19] F. Gabriel, *Position Self-Sensing of Permanent-Magnet Machines using High-Frequency Signal Injection*, Brussels: VUBPRESS Brussels University Press, 2013.
- [20] D. A. Staton, T. J. E. Miller and S. E. Wood, "Maximising the saliency ratio of the synchronous reluctance motor," *Proc. Inst. Elect. Eng.-Elect. Power Appl.*, vol. 140, no. 4, pp. 249-259, Jul. 1993.
- [21] A. Boglietti, M. Cavagnino, M. Pastorelli and V. A., "Experimental Comparison of Induction and Synchronous Reluctance Motors Performance," in *Conf. Rec. 40th IEEE IAS Annu. Meeting*, Kowloon, Hong Kong, 2005.

- [22] ABB, "SynRM motor and drive package (Motor Summit 2012)," 2012. [Online]. Available: [www.motorsummit.ch/data/files/MS\\_2012/presentation/ms12\\_tammi.pdf](http://www.motorsummit.ch/data/files/MS_2012/presentation/ms12_tammi.pdf).
- [23] N. Bianchi, "Synchronous Reluctance and Interior Permanent Magnet Motors," in *IEEE Workshop on Electrical Machine Design, Control and Diagnosis, WEMDCD 2013*, Paris, France, Mar. 2013.
- [24] N. Bianchi, E. Fornasiero, M. Ferrari and M. Castiello, "Experimental comparison of PM assisted synchronous reluctance motors," in *Conf. Rec. of the 2014 IEEE Energy Conversion Conference and Exposition ECCE*, Pittsburgh, PA, USA, 2014.
- [25] S. Morimoto, M. Sanada and Y. Takeda, "Performance of PM assisted synchronous reluctance motor for high efficiency and wide constant power operation," in *Conf. Record of the 2000 IEEE Ind. Appl. Conf.*, Rome, Italy, Oct. 2000.
- [26] R. Vartanian and H. Toliyat, "Design and comparison of an optimized permanent magnet-assisted synchronous reluctance motor (PMA-SynRM) with an induction motor with identical NEMA Frame stators," in *IEEE Electric Ship Technologies Symp., 2009. ESTS 2009*, Baltimore, MD, USA, Apr. 2009.
- [27] S. Morimoto, M. Sanada and Y. Takeda, "Inverter-Driven Synchronous Motors for Constant Power," *IEEE Ind. Appl. Mag.*, vol. 2, no. 6, pp. 18-24, Dec. 1996.
- [28] M. Schweizer, T. Friedli and J. Kolar, "Comparative Evaluation of Advanced 3-level Inverter/Converter Topologies against 2-level Systems," 17 Jun. 2015. [Online]. Available: [www.pes.ee.ethz.ch/uploads/tx\\_ethpublications/ecpe\\_multilevel\\_schweizer.pdf](http://www.pes.ee.ethz.ch/uploads/tx_ethpublications/ecpe_multilevel_schweizer.pdf). [Accessed Jun. 2015].
- [29] N. Mohan, T. M. Undeland and W. P. Robbins, *Power Electronics: Converters, Applications and Design*, 3rd ed., Wiley, 2003.
- [30] T. M. Jahns, "Flux-Weakening Regime Operation of an Interior Permanent-Magnet Synchronous Motor Drive," *IEEE Trans. Ind. Appl.*, vol. 23, no. 4, pp. 681-689, Aug. 1987.

- [31] R. R. Moghaddam, F. Magnussen and C. Sadarangani, "Theoretical and Experimental Reevaluation of Synchronous Reluctance Machines," *IEEE Trans. Ind. Electron.*, vol. 57, no. 1, pp. 6-13, Jan. 2010.
- [32] M. Ferrari, N. Bianchi and E. Fornasiero, "Rotor saturation impact in synchronous reluctance and PM assisted reluctance motors," in *Conf. Rec. of the 2013 IEEE Energy Conversion Conference and Exposition ECCE*, Pittsburgh, PA, USA, 2013.
- [33] R. H. Park, "Two Reaction Theory of Synchronous Machines Generalized Method of Analysis-Part I," *Trans. of Amer. Inst. of Elect. Eng.*, vol. 48, no. 3, pp. 716-727, Jul. 1929.
- [34] J. R. Hendershot and T. J. E. Miller, *Design of Brushless Permanent-Magnet Motors*, 2nd ed., Motor Design Books, 2010.
- [35] A. Vagati, M. Pastorelli, F. Scapino, G. Francheschini, "Impact of Cross Saturation in Synchronous Reluctance Motors of the Transverse-Laminated Type," *IEEE Trans. Ind. Appl.*, vol. 36, no. 4, pp. 1039-1046, Aug. 2000.
- [36] W. L. Soong and T. J. E. Miller, "Field-weakening performance of brushless synchronous AC motor drives," *IEEE Proc. Electr. Power Appl.*, vol. 141, no. 6, pp. 331-340, Nov. 1994.
- [37] I. Boldea, *Reluctance Synchronous Machines and Drives*, New York: Oxford University Press, 1996.
- [38] W. L. Soong, D. A. Staton and T. J. E. Miller, "Design of a New Axially-Laminated Interior Permanent Magnet Motor," *IEEE Trans. Ind. Appl.*, vol. 31, no. 2, pp. 358-367, Apr. 1995.
- [39] A. C. Polycarpou, *Introduction to the Finite Element Method in Electromagnetics*, Morgan & Claypool Publishers, 2006.
- [40] D. A. Lowther and P. P. Silvester, *Computer-Aided Design in Magnetics*, New York: Springer-Verlag, 1986.
- [41] P. P. Silvester and R. L. Ferrari, *Finite Elements for Electrical Engineers*, 3rd ed., Cambridge University Press, 1996.
- [42] J.-M. Jin, *The Finite Element Method in Electromagnetics*, 3rd ed., Wiley, 2014.

- [43] Infolytica Corporation, "MagNet and MotorSolve BLDC: 2D/3D Electromagnetic Field Simulation Software," Dec. 2014. [Online]. Available: [www.infolytica.com](http://www.infolytica.com).
- [44] TM4, "SUMO Datasheet," Mar. 2015. [Online]. Available: [www.tm4.com/wp-content/uploads/2015/03/TM4-SUMO-datasheet.pdf](http://www.tm4.com/wp-content/uploads/2015/03/TM4-SUMO-datasheet.pdf).
- [45] F. Jurecka, Robust Design Optimization Based on Metamodeling Techniques, München: Technische Universität München, 2007.
- [46] J.-S. Park, "Optimal latin-hypercube designs for computer experiments," *J. of Statistical Planning and Inference*, vol. 39, no. 1, pp. 95-111, Apr. 1994.
- [47] M. Johnson, L. Moore and D. Ylvisaker, "Minimax and maximin distance designs," *J. of Statistical Planning and Inference*, vol. 26, no. 2, pp. 131-148, Oct. 1990.
- [48] Wikipedia, "Pareto Efficiency," May 2006. [Online]. Available: [www.wikipedia.org/wiki/Pareto\\_efficiency](http://www.wikipedia.org/wiki/Pareto_efficiency).
- [49] J. Pyrhonen, T. Jokinen and V. Hrabovcova, Design of Rotating Electric Machines, Wiley, 2009.
- [50] A. Vagati, B. Boazzi, G. P. and G. Pellegrino, "Design of Ferrite-Assisted Synchronous Reluctance Machines Robust Toward Demagnetization," *IEEE Trans. Ind. Appl.*, vol. 50, no. 3, pp. 1768-1779, Jun. 2014.
- [51] M. Sanada, K. Hiramoto, S. Morimoto and Y. Takeda, "Torque ripple improvement for synchronous reluctance motor using asymmetric flux barrier arrangement," *IEEE Trans. Ind. Appl.*, vol. 40, no. 4, pp. 250-255, Aug. 2004.
- [52] A. Vagati, M. Pastorelli, G. Franceschini and S. C. Petrache, "Design of Low-Torque-Ripple Synchronous Reluctance Motors," *IEEE Trans. Ind. Appl.*, vol. 34, no. 4, pp. 758-765, Aug. 1998.
- [53] G. Pellegrino, F. Cupertino and C. Gerada, "Automatic Design of Synchronous Reluctance Motors focusing on Barrier Shape Optimization," *IEEE Trans. Ind. Appl.*, vol. 51, no. 2, pp. 1465-1474, Apr. 2015.

- [54] S. Burer and A. N. Letchford, "Non-Convex Mixed-Integer Non-linear Programming: A Survey," *Surveys in Operations Research and Manage. Sci.*, vol. 17, no. 2, pp. 97-106, Jul. 2012.
- [55] MathWorks MATLAB, "Parallel Computing Toolbox User's Guide," 2015. [Online]. Available: [www.mathworks.com/help/pdf\\_doc/distcomp/distcomp.pdf](http://www.mathworks.com/help/pdf_doc/distcomp/distcomp.pdf).
- [56] M. T. Hagan, H. B. Demuth and M. H. Beale, *Neural Network Design*, 2nd ed., Oklahoma: Martin Hagan, 2002.
- [57] D. J. C. MacKay, "Bayesian Interpolation," *Neural Computation*, vol. 4, no. 3, pp. 415-447, May 1992.
- [58] F. D. Foresee and M. T. Hagan, "Gauss-Newton approximation to Bayesian regularization," in *Proc. 1997 Int. Joint Conf. Neural Networks*, Houston, TX, USA, 1997.
- [59] S. P. Boyd and L. Vandenberghe, *Convex Optimization*, Cambridge: Cambridge University Press, 2004.
- [60] M. Mitchell, *An Introduction to Genetic Algorithms*, Cambridge, MA: MIT Press, 1999.
- [61] S. Giurgea, H. S. Zire and A. Miraoui, "Two-Stage Surrogate Model for Finite-Element-Based Optimization of Permanent-Magnet Synchronous Motor," *IEEE Trans. Magn.*, vol. 43, no. 9, pp. 3607-3613, Sep. 2007.
- [62] G. Crevecoeur, P. Sergeant, L. Dupre and R. Van de Walle, "A Two-Level Genetic Algorithm for Electromagnetic Optimization," *IEEE Trans. Magn.*, vol. 46, no. 7, pp. 2585-2595, Jul. 2010.
- [63] M. Grant and S. P. Boyd, "Graph implementations for nonsmooth convex programs," in *Recent Advances in Learning and Control*, V. Blondel, S. P. Boyd and H. Kimura, Eds., Springer-Verlag Limited, 2008, pp. 95-110.
- [64] M. Grant and S. Boyd, "CVX: Matlab software for disciplined convex programming, version 2.0 beta," Sep. 2013. [Online]. Available: <http://cvxr.com/cvx>.

- [65] A. Boglietti, A. M. El-Refaie, O. Drubel, A. M. Omekanda, N. Bianchi, E. B. Agamloh, M. Popescu, A. D. Gerlando and J. B. Bartolo, "Electrical Machine Topologies: Hottest Topics in the Electrical Machine Research Community," *IEEE Ind. Electron. Mag.*, vol. 8, no. 2, pp. 18-30, Jun. 2014.
- [66] Magcraft Advanced Magnetic Materials, "Permanent Magnet Selection and Design Handbook," Jul. 2015. [Online]. Available: [www.rare-earth-magnets.com](http://www.rare-earth-magnets.com).
- [67] P. Niazi, H. A. Toliyat, D.-H. Cheong and J.-C. Kim, "A low-cost and efficient permanent magnet assisted synchronous reluctance motor drive," *IEEE Trans. Ind. Appl.*, vol. 43, no. 2, pp. 542-550, Apr. 2007.